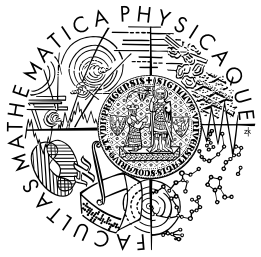

FACULTY
OF MATHEMATICS
AND PHYSICS
Charles University

BACHELOR THESIS

Marco Souza de Joode

Modeling of protoplanetary disks based on ALMA and VLTI measurements

Astronomical Institute of the Charles University

Supervisor of the bachelor thesis: doc. Mgr. Miroslav Brož, Ph.D.
Study programme: Physics
Study branch: Physics

Prague 2024

I declare that I carried out this bachelor thesis independently, and only with the cited sources, literature and other professional sources. It has not been used to obtain another or the same degree.

I understand that my work relates to the rights and obligations under the Act No. 121/2000 Sb., the Copyright Act, as amended, in particular the fact that the Charles University has the right to conclude a license agreement on the use of this work as a school work pursuant to Section 60 subsection 1 of the Copyright Act.

In ..... date ....

Author's signature

I would like to thank my advisor, doc. Miroslav Brož, for everything he has done for me during the past years. I can only wish my future academic experiences will be as enjoyable and exciting as those I had with doc. Brož. I will forever remember these times fondly.

I must thank my family, especially my parents and sister, for their love and ecouragement. Without them, I would have never gone on this path.

I want to express my gratitude to all the teachers from the Faculty of Mathematics and Physics, for teaching me all the things I could have never learned on my own. I would not have been able to finish this work three years ago. I enjoyed studying here immensely, not in small part thanks to my friends and classmates. Thank you.

I would also want to thank Dr. Miroslav Bárta for help with the data and preparation of the ALMA proposal.

Title: Modeling of protoplanetary disks based on ALMA and VLTI measurements

Author: Marco Souza de Joode

Institute: Astronomical Institute of the Charles University

Supervisor: doc. Mgr. Miroslav Brož, Ph.D., Astronomical Institute of the Charles University

Abstract:

The protoplanetary disk DoAr 44 (Haro 1-16, V2062 Oph) is a pre-transitional disk in the Ophiuchus star-forming region. A large observational dataset is available, including ALMA complex visibilities, VLTI/GRAVITY continuum squared visibilities, closure phases and triple products, VLT/UVES and VLT/X-shooter Hα spectra. Additionaly, spectral energy distribution measurements were utilized, including observations from ground-based optical observatories, the IRAS satellite and the Spitzer Space Telescope, the Sub-Millimeter Array, the 30-m IRAM radio telescope, the Australia Telescope Compact Array and others.

For the first time, this work presents a comprehensive global multi-scale kinematic equilibrium radiative-transfer model, constructed in `Pyshellspec` (Brož et al., 2021), describing the accretion region, the inner and the outer disks. According to my model, the spectral line profiles are explained by an optically thin spherical inflow/outflow within the co-rotation radius of the star, with velocities surpassing 330 km/s. The VLTI near-infrared interferometric observables can be accounted for by an innermost disk, extending from 0.1 to 0.2 au. On the other hand, the ALMA visibilities are compatible with a dust ring, extending from 36 to 56 au. The temperature and density profiles derived from my model suggest the ring could be related the condensation line of CO_2. My models also placed constraints on the inner disk, which has never been spatially resolved. These constraints allowed me to prepare and submit an ALMA proposal to study this region (1–10 au), which is the critical region for the formation of terrestrial and gas-giant planets.

Keywords: protoplanetary disks, star formation, planet formation, radio astronomy, radiative transfer, interferometry

Contents

Chapter 1

Introduction to protoplanetary disks

...for dust thou art,
and unto dust shalt thou return.

Genesis 3:19

Protoplanetary disks are large reservoirs of gas and dust, and the presumed birthplace of planets. Perhaps the first observation of a protoplanetary disk was conducted in 1852 by Hind (1864), who noted variability and nebulosity (NGC 1555) around the star T Tauri. It later served as an eponym for the class of T Tauri stars, whose unpredictable and irregular variability was associated by Joy (1945) with an ongoing accretion of circumstellar matter. He made this association by noting that these stars exhibit a brightening of emission lines during light curve maxima and their association with dark or bright nebulosity. In total, Joy (1945) identified forty objects with strong emission lines in the vicinity of the Taurus molecular cloud, inspiring Struve and Rudkjøbing (1949) to discover a similar stellar association on the Ophiuchus–Scorpius boundary. Both of these discoveries are now known to be star-forming regions. A similar but brighter class of objects has been identified by Herbig (1960), noticing emission lines and nebulosity, now called Herbig Ae/Be stars.

Heated circumstellar matter inevitably produces thermal emission in the mid-infrared bands. The first astronomical apparatus capable of observing in the $1 - 5\,\mu\text{m}$ wavelength range was constructed by Johnson and Mitchell (1962), where we also first find the designation J, K, L, M for the 1.3, 2.2, 3.6 and 5.0µm bands respectively. It was used by Mendoza (1966) to identify a large infrared excess in the Spectral-Energy Distribution (SED) for several T Tauri objects, inexplicable by interstellar extinction.

1.1 Observational evidence for Young Stellar Objects

Near infrared and millimeter wave observations by Wilking and Lada (1983) and Lada and Wilking (1984) in the Ophiuchus star forming region are a foundation of a classification based on spectral indices around $2\,\mu\text{m}$, as suggested by Lada (1987). This system, in its various modifications is used to this day. The spectral index is commonly defined as:

$$\alpha := \frac{\mathrm{d}\log(\lambda F_\lambda)}{\mathrm{d}\log\lambda}\,, \tag{1.1}$$

where F_λ denotes the monochromatic flux. It is a measure of the contribution of the circumstellar matter surrounding the Young Stellar Object (YSO). For an ideal black body, well

described by a single temperature, the monochromatic intensity (and therefore the flux) scales in the Rayleigh-Jeans regime with the fourth power of the wavelength:

$$F_\lambda \propto \frac{1}{\lambda^4} \implies \lambda F_\lambda \propto \lambda^{-3}, \tag{1.2}$$

which makes the spectral index of an ideal blackbody $\alpha = -3$. The original classification was the following:

Class I $0 < \alpha \lesssim +3$: the peak in the near-IR spectrum,
Class II $-2 \lesssim \alpha < 0$: an almost flat near-IR spectrum,
Class III $-3 < \alpha \lesssim -2$: the near-IR spectrum similar to a stellar photosphere.

Class I objects were associated by Lada (1987) with **protostars**, Class II objects with **classical T Tauri objects** (massive gas-rich protoplanetary disks) and Class III objects with very young main sequence (hydrogen burning) stars surrounded by distant dust, what would now be called a **debris disk**, or a weak-lined T Tauri star (Barsony, 1994).

Later, based on Very Large Array (VLA) observations, **Class 0 objects** were added to this classification (Andre et al., 1993), which are even more primitive than Class I, having a peak of emission in the far-IR or sub-mm domain.

Strom et al. (1990) identified several objects showing small near infrared excesses (25 µm), and large far-IR and mm excesses, indicating a formation of a large central cavity in the protoplanetary disks. They suggested these objects are undergoing a transition from Class II to Class III, assembling the material in the gap into larger bodies (planetesimals or protoplanets).

In debris disks, later evolutionary stages of protoplanetary disks, where the gas has already dispersed, gaps in the dust were found to harbour planets. The most famous examples include the direct observation of the exoplanet β Pictoris b by the now decommissioned instrument VLT/NaCo (Lagrange et al., 2010), or the direct imaging of PDS 70 b and PDS 70 c with VLT/SPHERE and VLT/MUSE, respectively (Keppler et al., 2018; Haffert et al., 2019).

Dodson-Robinson and Salyk (2011) pointed out that a planet radially clears about 5 Hill's radii, and therefore a single planet cannot create large cavities (≈ 30 au) observed in some disks, such as DM Tau or GM Aur.

Espaillat et al. (2007) identified a new class called *pre-transitional* disks, based on Spitzer spectra of UX Tau A and LkCa15: objects with optically thick millimeter emission in the outer region ($\gtrsim 40$ au), an optically thick region with micron emission in the inner region ($\lesssim 5$ au), but with an optically thin region in between, that contributes very little to the total SED. Espaillat et al. (2010) identified DoAr 44, the subject of this work, as one of these pre-transitional disks.

I believe it to be a great success of astronomy, and by extension of the scientific method, that the predictions made in the 1990s of the dimensions of the cavities in transition disks, based on disk-integrated SED measurements, were spectacularly confirmed by radio-interferometric aperture synthesis in the 2010s. First confirmations were done with ALMA precursors, such as studies using the Submillimeter Array (SMA) (Andrews et al. (2011), Brown et al. (2009)), Combined Array for Research in Millimeter-wave Astronomy (CARMA) (e.g., Isella et al. (2009), Isella et al. (2009)) and the Plateu de Bure Interféromètre (PdBI), replaced in 2014 by Northern Extended Millimeter Array (NOEMA) (e.g., Hughes et al. (2009); Pinilla et al. (2014)).

1.2 Notes on formation

Fascinatingly, when Kant (1755) and Laplace (1796) proposed the nebular hypothesis, i.e., that the solar system formed from a rotating cloud of material, they did not see it on the sky. When Jeans (1902) derived the criterion for the instability of a cold gas cloud — the so-called Jeans criterion, he did not see any collapsing clouds or Class-0 objects. When Hayashi (1961) calculated the temperature-luminosity relation of pre-main-sequence objects — the so-called Hayashi line, he did not consider that these objects accrete additional mass. When Pringle (1981) studied the conservation of angular momentum in a collapsing gas cloud, and realized that it becomes geometrically thin, fast-rotating disk, he hardly knew how complex are processes occurring in these disks.

Nevertheless, it is clear that it is necessary to know these classic analytic results, which are described in detail for example in Pringle (1981) or Armitage (2020). The goal of the next sections is to briefly review the dynamics, structure, accretion and heating of thin disks.

1.3 Thin disk dynamics

Let us consider the equation of continuity for the matter density ϱ in a velocity field $\boldsymbol{v}$:

$$\frac{\partial \varrho}{\partial t} + \nabla \cdot \varrho \boldsymbol{v} = 0\,. \tag{1.3}$$

In upcoming discussions of protoplanetary disks, we shall be using cylindrical coordinates (R, ϕ, z). We thus introduce the column density, integrated along the vertical axis:

$$\Sigma(R,\phi) := \int_{-\infty}^{\infty} \varrho(R,\phi,z)\mathrm{d}z\,. \tag{1.4}$$

The continuity equation for the column density in cylindrical coordinates in which the Lamé coefficients have the form:

$$\frac{\partial \Sigma}{\partial t} + \frac{1}{R}\frac{\partial}{\partial R}\left(\Sigma R v_R\right) = 0\,, \tag{1.5}$$

where v_R is the radial component of the velocity field $\boldsymbol{v}$. Now, let us consider the angular momentum of a rotating annulus of the inner radius R and the outer radius $R + \delta R$, with an angular velocity field Ω:

$$\delta L = 2\pi R \delta R \cdot R^2 \Omega \Sigma\,, \tag{1.6}$$

where the first term is the area of the annulus, and the second term is the angular momentum per area (with $l = R^2\Omega$ being the specific angular momentum). We can analyze the influx and outflux of the angular momentum at the borders of the annulus:

$$\dot{L}_{\mathrm{in}} = 2\pi R \cdot R^2\,\Omega(R)\,\Sigma(R)\,v_R(R)\,, \tag{1.7}$$

$$\dot{L}_{\mathrm{out}} = 2\pi(R+\delta R)\cdot(R+\delta R)^2\,\Omega(R)\,\Sigma(R+\delta R)\,v_R(R+\delta R)\,. \tag{1.8}$$

Considering a torque τ applied by external forces (other annuli), which can be expressed as:

$$\tau = \delta R \frac{\partial \tau}{\partial R}\,, \tag{1.9}$$

we can balance the fluxes of angular momentum. Taking a time derivative of Equation 1.6:

$$2\pi R \delta R \frac{\partial}{\partial t}(R^2\Omega\Sigma) = \dot{L}_{\mathrm{out}} - \dot{L}_{\mathrm{in}} + \delta R \frac{\partial \tau}{\partial R} \tag{1.10}$$

and taking a limit for $\delta R \to 0$:

$$\boxed{R\frac{\partial}{\partial t}(R^2\Omega\Sigma) + \frac{\partial}{\partial R}(R^2\Omega\Sigma R v_R) = \frac{1}{2\pi}\frac{\partial \tau}{\partial R}}\,, \tag{1.11}$$

we obtain continuity equation for angular momentum. We can also express the derivatives:

$$R\frac{\partial \Sigma}{\partial t}(R^2\Omega) + R\Sigma\frac{\partial}{\partial t}(R^2\Omega) + R^2\Omega\frac{\partial}{\partial R}(\Sigma R v_R) + \Sigma R v_R\frac{\partial}{\partial R}(R^2\Omega) = \frac{1}{2\pi}\frac{\partial \tau}{\partial R}$$

and notice that the red (1st and 3rd) terms add to zero per the continuity equation (Equation 1.5). If we assume a stationary disk, i.e., $\partial\Omega/\partial t = 0$, the second term is also zero. Therefore we get:

$$R\Sigma v_R\frac{\partial}{\partial R}(R^2\Omega) = \frac{1}{2\pi}\frac{\partial \tau}{\partial R}\,. \tag{1.12}$$

If we substitute this result back into the mass continuity equation (Equation 1.5):

$$\boxed{\frac{\partial \Sigma}{\partial t} = \frac{1}{R}\frac{\partial}{\partial R}\left(\frac{1}{2\pi\frac{\partial}{\partial R}(R^2\Omega)}\frac{\partial \tau}{\partial R}\right)}\,, \tag{1.13}$$

which is the evolutionary equation for the surface density of a thin stationary disk with a general angular velocity profile. Further, assuming Keplerian angular velocities around a central star of mass $M_\star$:

$$\Omega = \Omega_K = \sqrt{\frac{GM_\star}{R^3}}\,. \tag{1.14}$$

To proceed further, we also need to prescribe the torque τ, in a reasonable way:

$$\tau = 2\pi R \cdot \nu\Sigma\frac{\partial \Omega}{\partial R}R \cdot R\,, \tag{1.15}$$

where the first term corresponds to the circumference of the annulus, the second gives a force per unit length, arising from a differential rotation and a kinematic viscosity ν, and the last term is the lever arm. Performing both derivatives, we arrive at:

$$\boxed{\frac{\partial \Sigma}{\partial t} = \frac{3}{R}\frac{\partial}{\partial R}\left[\sqrt{R}\frac{\partial}{\partial R}(\nu\Sigma\sqrt{R})\right]}\,, \tag{1.16}$$

which is the evolution equation for a Keplerian disk. Given a solution to Equation 1.16, we can express the radial drift velocity from Equation 1.12:

$$v_R = \frac{-3}{\Sigma\sqrt{R}}\frac{\partial}{\partial R}(\sqrt{R}\nu\Sigma)\,. \tag{1.17}$$

1.4 Steady state disk

Now, in addition to our previous assumptions, let us assume the disk is steady, i.e.,

$$\frac{\partial \Sigma}{\partial t} = 0\,.$$

In such a case, the continuity equation (Equation 1.5) becomes:

$$\frac{\partial}{\partial R}(\Sigma R v_R) = 0 \implies \Sigma R v_R = \text{const.} \tag{1.18}$$

This is a statement about mass conservation in a given annulus, as the mass flow through its inner boundary is given by:

$$\dot{M} = -2\pi R \Sigma R v_R \,. \tag{1.19}$$

The continuity equation for the angular momentum (Equation 1.11) becomes:

$$\underbrace{R\frac{\partial}{\partial t}(R^2\Omega\Sigma)}_{=0} + \frac{\partial}{\partial R}(R^2\Omega\Sigma R v_R) = \frac{1}{2\pi}\frac{\partial \tau}{\partial R}\,, \tag{1.20}$$

therefore we can integrate and substitute for τ from Equation 1.15, and:

$$\Sigma R v_R \cdot R^2\Omega = \frac{\tau}{2\pi} + \frac{C}{2\pi} = R^3\nu\Sigma\frac{\partial\Omega}{\partial t} + \frac{C}{2\pi}\,,$$

$$\nu\Sigma\frac{\partial\Omega}{\partial t} = -\Sigma v_R\Omega + \frac{C}{2\pi R^3}\,. \tag{1.21}$$

The angular velocity in the Keplerian profile grows to infinity as we approach $R \to 0$. However, the surface of the central star is rotating at a reasonable speed, otherwise the it would not be a bound body. As the surface of the star and the inner disk are coupled by the means of viscosity of the gas and stellar magnetic fields, the angular velocity must start decreasing at some point in the proximity of the star. Therefore, there must be a point where $\partial\Omega/\partial t$, and this point will be around $R \approx R_\star$, where $R_\star$ is the stellar radius. Substituting this angular velocity maximum into 1.21:

$$C = 2\pi R^3 v_R \Omega = 2\pi R \Sigma v_R \cdot R^2\Omega = -\dot{M}R^2\Omega\,.$$

Further assuming that the angular velocity in this region is almost Keplerian, $\Omega \approx \Omega_K$:

$$C = -\dot{M}\sqrt{GM_\star R_\star}\,.$$

Substituting into Equation 1.21 and rearranging:

$$\boxed{\nu\Sigma = \frac{\dot{M}}{3\pi}\left(1 - \sqrt{\frac{R_\star}{R}}\right)}\,. \tag{1.22}$$

This gives us a surface density prescription for a steady-state disk with a constant accretion rate $\dot{M}$. Note, that:

$$\Sigma(R) \propto \frac{1}{\nu}\,. \tag{1.23}$$

1.5 Magnetospheric accretion

Now lets take a more detailed look at the idea below the Equation 1.21, that will give us a limit on the inner radius of the disk. If we look at the Keplerian orbital velocity at the surface of the star:

$$v_\phi = \sqrt{\frac{GM}{r}} \approx \sqrt{\frac{GM}{R}}\,, \tag{1.24}$$

Nevertheless, the stellar surface itself is rotating much slower, with a rotational period of P, or with the angular velocity $\omega_\star = 2\pi/P$, and so is the plasma directly above the stellar photosphere, as it is frozen in the stellar magnetic field. For T Tauri stars, the period is typically more than 2 days but less than two weeks (Bouvier et al., 2006; Pouilly et al., 2020; Serna et al., 2021). In the vicinity of the star, limited by some critical radius, the plasma is decelerated from the Keplerian velocity. This radius can be approximated by the co-rotation radius, i.e., the point, where:

$$\omega_\star R_{\rm co} = \sqrt{\frac{GM}{R_{\rm co}}} \implies R_{\rm co} = \sqrt[3]{\frac{GM_\star}{\omega_\star^2}}\,. \tag{1.25}$$

Below this point, the material is orbiting slower than the Keplerian velocity, and eventually accretes onto the star.

We can also define the so-called truncation radius $r_{\rm tr}$, where the ram pressure of the infalling matter ($P = \frac{1}{2}\varrho v_R^2$) equals the magnetic pressure $P_B = \frac{B^2}{2\mu}$, where B is the magnetic field and μ is the magnetic permeability. For spherically symmetric accretion, where the mass accretion rate can be written as:

$$\dot{M} = 4\pi r_{\rm tr}^2 \varrho v_R\,, \tag{1.26}$$

we can rewrite the pressure balance as:

$$\frac{1}{2}\varrho v_R^2 = \frac{1}{2}\varrho \frac{\dot{M}^2}{16\pi^2 {r_{\rm tr}}^4 \varrho^2} = \frac{B^2}{2\mu}\,. \tag{1.27}$$

If a dipole field is assumed for the magnetic field around the star in the equatorial plane:

$$B = B_\star \left(\frac{R_\star}{r_{\rm tr}}\right)^3\,. \tag{1.28}$$

Substituting for the magnetic field into Equation 1.27 and rearanging, we obtain:

$$\boxed{r_{\rm tr} = \frac{4\pi}{\dot{M}} R_\star^3 B_\star \sqrt{\frac{\varrho}{\mu}}}\,. \tag{1.29}$$

The resulting truncation radius tends to be very close to the corotation radius, for typical magnetic fields measured on T Tauri stars by Zeeman broadening (Bouvier et al., 2006).

1.6 Viscous heating

Accretion disks in astrophysics can be famously hot objects, e.g., around black holes, but accretion heating is significant even in the case of protoplanetary disks. The power dissipated due to viscous friction can be calculated as a product of of the torque and the angular velocity. A contribution of a narrow annulus is:

$$\Omega \frac{\partial \tau}{\partial R} {\rm d}R = \left[\frac{\partial}{\partial R}(\tau\Omega) - \tau\frac{\partial \Omega}{\partial R}\right] {\rm d}R\,. \tag{1.30}$$

Integrating the first term, we get a contribution to the power from the conditions at the edges, $P_A = [\tau\Omega]_{\rm in}^{\rm out}$. The second term quantifies the local loss of mechanical energy due to viscous

dissipation. We can express it in terms of energy loss per area (having to consider both sides of the disk):

$$Q = \frac{\tau \frac{\partial \Omega}{\partial R}}{4\pi R} \,. \tag{1.31}$$

Assuming a Keplerian velocity profile, a torque given by 1.15, and substituting from Equation 1.22:

$$Q = \frac{9}{8}\nu\Sigma\frac{GM_\star}{R^3} = \frac{3G\dot{M}M_\star}{8\pi R^3}\left(1 - \sqrt{\frac{R_\star}{R}}\right) \,. \tag{1.32}$$

From the Stefan-Boltzmann law, we now know how to calculate the effective temperature due to heating:

$$T_{\rm eff}^4 = \frac{3G\dot{M}M_\star}{8\pi\sigma R^3}\left(1 - \sqrt{\frac{R_\star}{R}}\right) \,. \tag{1.33}$$

Integrating the energy dissipation from equation 1.31 from $R_{\rm in}$ to $R_{\rm out}$ (substituting $t = R_\star/R$), we obtain the total luminosity due to the viscous heating:

$$L = 2\int_{R_{\rm in}}^{R_{\rm out}} Q 2\pi R {\rm d}R = \frac{3}{2}G\dot{M}M_\star\left[\frac{1}{R_{\rm in}}\left(1 - \frac{2}{3}\sqrt{\frac{R_\star}{R_{\rm in}}}\right) - \frac{1}{R_{\rm out}}\left(1 - \frac{2}{3}\sqrt{\frac{R_\star}{R_{\rm out}}}\right)\right] \,. \tag{1.34}$$

Calculating the limit as $R_{\rm in} \to R_\star$ and $R_{\rm out} \to \infty$ we obtain an limit for the luminosity:

$$L = \frac{G\dot{M}M_\star}{2R_\star} \,. \tag{1.35}$$

1.7 Vertical structure

Protoplanetary disks were found not to be completely flat, but their thickness grows with the distance from the central star. This was predicted by Kenyon and Hartmann (1987) based on analytic models of the SED, and was later proven to be true in the 1990s by Hubble Space Telescope (HST) observations e.g., Stapelfeldt et al. (1999). The gravitational potential in a protoplanetary disk deviates slightly from a central field, as the disk holds some mass:

$$\Phi = \frac{GM_\star}{r} + \Phi_{\rm disk} \,, \tag{1.36}$$

where $r \equiv \sqrt{R^2 + z^2}$. However, this contribution is small and we shall neglect in this calculation. Writing the equation of motion of a gas element, whose pressure is described by $P(z)$ at a given distance R from the axis of the disk, with:

$$\nabla\Phi = \frac{1}{\varrho}\nabla P \,, \tag{1.37}$$

and focusing on the vertical component:

$$\frac{GM_\star}{r^2}\frac{z}{r} = \frac{1}{\varrho}\frac{{\rm d}P}{{\rm d}z} \,. \tag{1.38}$$

Assuming the disk is isothermal at the given radial distance with $P = \varrho c_s^2$, where the speed of sound is given by the temperature profile:

$$c_s^2 = \frac{k_{\rm B}T}{\mu m_{\rm u}} \,, \tag{1.39}$$

where k_B is Boltzmann's constant, is the mean molecular weight in the medium and m_u is the atomic mass unit. Then, we can separate the equation of motion into:

$$-\frac{\mu m_u}{k_B T}\frac{GM_\star}{r^3}\int z\mathrm{d}z =: \frac{1}{H}\int z\mathrm{d}z = \int \frac{1}{\varrho}\,\mathrm{d}\varrho\,,$$

where H is defined as the scale height. The integration constant corresponds to a the mid-plane density. Also, now the difference between R and r is negligible:

$$\varrho(R,z) = \varrho(R,z=0)\exp\left(-\frac{z^2}{2H^2}\right)\,. \tag{1.40}$$

From our definition of column density (Equation 1.4), integrating this result we obtain:

$$\Sigma = \int_{-\infty}^{\infty}\varrho\,\mathrm{d}z = \varrho(R,z=0)H\,, \tag{1.41}$$

so that wee see the relation to the scale height:

$$H(R) = \frac{\Sigma(R)}{\varrho(R,z=0)}\,. \tag{1.42}$$

1.8 Astronomical interferometry

Models must be constrained by observations, and the respective tool that allowed for (arguably) the most progress in the field of protoplanetary disks is astronomical interferometry, both in the optical and radio domain.

Michelson and Pease (1921) were the first to measure α Ori using an interferometer mounted on the 100-inch Cassegrain on Mount Wilson, and inferred its angular size using the Rayleigh criterion and the concept of the *visibility* $\mathcal{V}$ of interference fringes, which Michelson proposed earlier (Michelson, 1890):

$$\mathcal{V} = \frac{I_\mathrm{max} - I_\mathrm{min}}{I_\mathrm{max} + I_\mathrm{min}}\,. \tag{1.43}$$

During the early 20-th century, the concepts of coherence and incoherence of light were treated as separate categories: either a phenomenon produced an interference pattern, or not, with no intermediate states. Zernike (1938) brought clarity to the entire field by introducing the concept of the degree of coherence. He imagined two points, P_1, P_2, in the same wave field. The vibration at the points $P_{1,2}$ can be described as:

$$a_{1,2}e^{i\phi_{1,2}}e^{i\omega t}\,,$$

with $a_{1,2} \in \mathbb{R}$ assumed scalar not to complicate the discussion with polarization effects, ω describing the monochromatic wave, and $\phi_{1,2}$ are phases. The complex amplitude is the time-independent part of the vibration:

$$A_{1,2} = a_{1,2}e^{i\phi_{1,2}}\,.$$

Traditional astronomical imaging has only access to the intensity of light at one point, which is given by the mean value of the square of the amplitude:

$$\mu_1 = \langle A_1 A_1^*\rangle\,, \tag{1.44}$$

$$\mu_2 = \langle A_2 A_2^*\rangle\,. \tag{1.45}$$

If we were to make a screen with two pinholes at P_1, P_2, and observe their interference patters on a detector behind the screen (*the focal plane*), we would again have only access to the intensity, but it would be dependent on the "parasitic" phase delay β introduced by a systematic path difference, which needs to be corrected for:

$$\mu = \mu(\beta) = \langle (A_1^* e^{-i\beta} + A_2^*)(A_1 e^{+i\beta} + A_2) \rangle = J_1 + J_2 + 2\Re\{\langle A_1^* A_2 \rangle e^{-i\beta}\} \,. \tag{1.46}$$

Lets denote $\mu_{12} = \langle A_1^* A_2 \rangle \in \mathbb{C}$. Zernike (1938) showed that its value on the detector, on the coordinates 2-dimensional coordinates $(u, v) \in \mathbb{R}^2$ on the screen with the two pinholes (*the aperture plane*) is:

$$\boxed{\mu_{12}(u,v) = \int_{\mathbb{R}^2} I(l,m) e^{-2\pi i(lu+mv)} \mathrm{d}l \, \mathrm{d}m = \mathcal{F}\{I(l,m)\}} \,, \tag{1.47}$$

where $I(l, m)$ is the intensity of the source on the *sky plane*, and $\mathcal{F}\{\cdot\}$ denotes its Fourier transform. This result is today called the van Cittert–Zernike theorem (van Cittert (1934) derived some similar results for some special cases, without the explicit connection to the Fourier transform).

The first astronomical interferometer using two separate telescopes, as opposed to the mirrors mounted on a single telescope, was constructed by Labeyrie (1975) in Nice. The interferometer consisted of two 250 mm telescopes separated by a 12 m baseline and an optical laboratory in between them.

Optical interferometry today still utilizes the contrast of interference fringes, although the technical challenges of maintaining coherence over large apertures and long baselines, needed for large angular resolutions, are immense – this is exemplified by the international effort of the European Southern Observatory (ESO) behind the Very Large Telescope Interferometer (VLTI).

The first radio interferometric observations were performed by Bolton and Stanley (1948) on a cliff above the sea near Sydney, observing the Cyg A radio source and its reflection of the sea, using two Yagi antennas tuned to 100 MHz. Monitoring the interference pattern between the direct and reflected rays, they achieved an astrometric precision of $7'$.

The principle of aperture synthesis in radio interferometry is illustrated in Figure 1.1, and some practical aspects of this discipline, necessary to interpret the visibilities needed for this thesis, are outlined in the next chapter.

1.8.1 Visibility of a homogeneous ellipse

Let us denote the coordinates on the tangent plane as l, m, and let us parameterize them as:

$$l = a\varrho \cos\phi_1 \,, \tag{1.48}$$

$$m = b\varrho \sin\phi_1 \,, \tag{1.49}$$

where a, b are dimensionless numbers and ϱ is in an angle in radians, describing the semi major and the semi minor axis of the ellipse on the sky. Similarly, let the aperture plane coordinates be given by:

$$u = br \cos\phi_2 \,, \tag{1.50}$$

$$v = ar \sin\phi_2 \,. \tag{1.51}$$

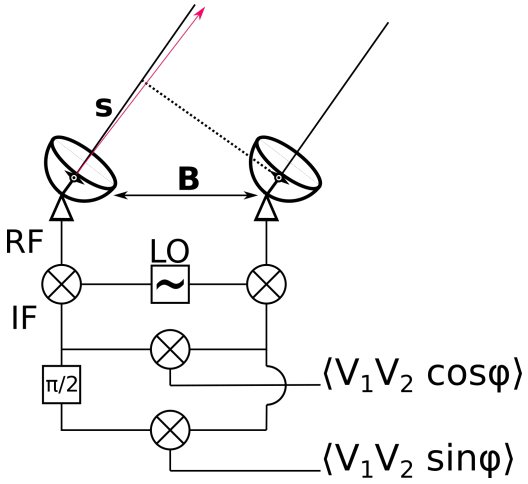

Figure 1.1: A radio interferometer measuring complex visibilities. Delay lines (possibly digital, not shown) compensate for the zero-order effect caused by the geometric phase delay β (not shown). The Radio Frequency (RF) signal from both antennas is mixed (multiplied) with a signal from a synchronized Local Oscillator (LO), producing a down-converted Intermediary Frequency (IF) signal. This can be amplified and correlated with the signal from the second antenna. Adding a $\pi/2$ phase-shift allows for the extraction of the entire complex visibility, as we can extract both the real and imaginary part separately (the $\cos\varphi$ term and the $\sin\varphi$ term).

where the scaling parameters are introduced to simplify a substitution later. Let us describe the intensity of the source as a homogeneous elliptical disk:

$$I(l,m) = \begin{cases} \frac{1}{\pi ab\theta^2} & \varrho = \sqrt{\left(\frac{l}{a}\right)^2 + \left(\frac{m}{b}\right)^2} < \theta\,, \\ 0 & \varrho = \sqrt{\left(\frac{l}{a}\right)^2 + \left(\frac{m}{b}\right)^2} > \theta\,, \end{cases} \tag{1.52}$$

where θ is an angle in radians. Now, using the van Cittert–Zernike theorem, the complex visibility is given by the Fourier transform of the intensity. Notice that our source function for a centered ellipse is real and even, therefore the Fourier transform will also be real:

$$f(-x) = f(x) \implies \mathcal{F}\{f\}(\xi) = \int_{\mathbb{R}^N} f(x) e^{-2\pi i(x,\xi)} \mathrm{d}x = \tag{1.53}$$

$$= \int_{\mathbb{R}^N} f(x)\cos(2\pi i(x,\xi))dx = \mathcal{F}\{f\}(-\xi) = \int_{\mathbb{R}^N} f(x)\cos(2\pi i(x,-\xi))\mathrm{d}x \in \mathbb{R}\,. \tag{1.54}$$

In our specific case, the complex visibility μ is given by:

$$\mu(u,v) = \int_{\mathbb{R}^2} I(l,m) e^{-2\pi i(lu+mv)} \mathrm{d}l\,\mathrm{d}m = \tag{1.55}$$

$$= \int_{\mathbb{R}^2} I(a\varrho\cos\phi_1, b\varrho\sin\phi_1) e^{-2\pi iab\varrho r\cos(\phi_1-\phi_2)} ab\varrho\,\mathrm{d}\varrho\,\mathrm{d}\phi_1\,, \tag{1.56}$$

where the identity $\cos\phi_1\cos\phi_2 + \sin\phi_1\sin\phi_2 = \cos(\phi_1-\phi_2)$ was used in the exponential. Now:

$$\mu = \frac{ab}{\pi ab\theta^2}\int_0^{2\pi}\int_0^{\theta} \varrho e^{-2\pi iab\varrho r\cos\phi}\mathrm{d}\varrho\,\mathrm{d}\phi\,. \tag{1.57}$$

By performing an integration by parts on in the inner integral, using a substitution $q = 2\pi abr\cos\phi$:

$$\int_0^{\theta} \varrho e^{-iq\varrho}\mathrm{d}\varrho = \frac{(1+iq\theta)e^{-iq\theta} - 1}{q^2}\,, \tag{1.58}$$

$$\mu = \frac{1}{\pi\theta^2}\int_0^{2\pi} \frac{(1+2\pi iabr\theta\cos\phi)e^{-2\pi iabr\theta\cos\phi} - 1}{4\pi a^2b^2r^2\cos^2\phi}\mathrm{d}\phi\,. \tag{1.59}$$

Differentiating under the integral sign with respect to θ, we obtain:

$$\frac{\mathrm{d}\mu}{\mathrm{d}\theta} = \frac{1}{\pi\theta^2}\int_0^{2\pi} \frac{(2\pi iabr\cos\phi)e^{-2\pi iabr\theta\cos\phi} - 2\pi iabr\cos\phi(1+2\pi iabr\theta\cos\phi)}{4\pi a^2b^2\cos^2\phi}\mathrm{d}\phi\,, \tag{1.60}$$

$$\frac{\mathrm{d}\mu}{\mathrm{d}\theta} = \frac{1}{\pi\theta}\int_0^{2\pi} e^{-2\pi iabr\theta\cos\phi}\mathrm{d}\phi\,. \tag{1.61}$$

Now, we shall use the following integral identity for the Bessel functions of the first kind of integer order:

$$J_n(z) = \frac{i^{-n}}{\pi}\int_0^{\pi} e^{-z\cos\theta}\cos(n\theta)\mathrm{d}\theta\,, \tag{1.62}$$

specifically for the zeroth-order:

$$J_0(z) = \frac{1}{\pi}\int_0^{\pi} e^{iz\cos\theta}\mathrm{d}\theta\,. \tag{1.63}$$

Then,

$$\frac{\mathrm{d}\mu}{\mathrm{d}\theta} = \frac{2}{\theta}\left[\frac{1}{\pi}\int_0^{\pi} e^{2\pi iabr\theta\cos\phi}\mathrm{d}\phi\right]^* = \frac{2}{\theta}\left[J_0(2\pi abr\theta)\right]^* = \frac{2}{\theta}J_0(2\pi abr\theta)\,, \tag{1.64}$$

because Bessel functions of the first kind of an integer order of a real value are real. Now, using the identity:

$$\frac{\mathrm{d}}{\mathrm{d}x}[x^mJ_m(x)] = x^mJ_{m-1}(x) \tag{1.65}$$

for $m=1$, using $z = 2\pi abr\theta$, $\frac{\mathrm{d}}{\mathrm{d}z} = \frac{1}{2\pi abr}\frac{\mathrm{d}}{\mathrm{d}\theta}$:

$$\frac{\mathrm{d}}{\mathrm{d}z}\left(2\pi^2a^2b^2r^2\theta^2\mu\right) = zJ_0(z) = \frac{\mathrm{d}}{\mathrm{d}z}(zJ_1(z))\,. \tag{1.66}$$

Therefore, using $k = 2\pi abr$:

$$\mu = \frac{2J_1(2\pi abr\theta)}{2\pi abr\theta} = \frac{2J_1(k\theta)}{k\theta}\,. \tag{1.67}$$

Converting to the original aperture plane coordinates, $r = \sqrt{(u/b)^2 + (v/a)^2}$, we obtain:

$$\mu(u,v) = \frac{2J_1(2\pi\theta\sqrt{a^2u^2+b^2v^2})}{2\pi\theta\sqrt{a^2u^2+b^2v^2}} = \frac{2J_1(2\pi\sqrt{\alpha^2u^2+\beta^2v^2})}{2\pi\sqrt{\alpha^2u^2+\beta^2v^2}}\,, \tag{1.68}$$

where now α, β are the semi-major and semi-minor axes of the ellipse in angular units (radians). For the special case of a circular disk, $a = b = 1$,

$$\mu(u,v) = \frac{2J_1(2\pi\theta\sqrt{u^2+v^2})}{2\pi\theta\sqrt{u^2+v^2}}\,. \tag{1.69}$$

1.8.2 Narrow elliptical ring

Using the same coordinates one can describe a narrow ring, described by an angular radius θ:

$$I(l(\varrho,\phi_1), m(\varrho,\phi_1)) = \frac{1}{2\pi\theta}\delta(\varrho-\theta)\,. \tag{1.70}$$

Then, its complex visibility is:

$$\mu(u,v) = \mathcal{F}\{I(l,m)\}(u,v) = \int_{\mathbb{R}^2} I(l,m) e^{-2\pi i(lu+mv)} \mathrm{d}l\, \mathrm{d}m = \tag{1.71}$$

$$= \frac{1}{2\pi\theta} \int_0^{2\pi} \theta e^{-2\pi i ab r \cos\phi} \mathrm{d}\phi = \frac{2\pi\theta}{2\pi\theta} J_0(2\pi ab\theta r) = J_0(2\pi\sqrt{u^2\alpha^2 + v^2\beta^2})\,, \tag{1.72}$$

using the same notation from the example. I will use this result to model the inner region.

1.8.3 General position angle

If we want to calculate the visibility of a source on the sky with a general orientation, i.e., a position angle, we can describe the rotated image $I'(l,m)$ as:

$$I'(l,m) = I(l',m')\,, \tag{1.73}$$

where $I(\cdot,\cdot)$ is the function describing the surface brightness of the non-rotated image and l', m' are given by:

$$\begin{pmatrix} l' \\ m' \end{pmatrix} = \begin{pmatrix} \cos\theta & \sin\theta \\ -\sin\theta & \cos\theta \end{pmatrix} \begin{pmatrix} l \\ m \end{pmatrix} \iff \begin{pmatrix} l \\ m \end{pmatrix} = \begin{pmatrix} \cos\theta & -\sin\theta \\ \sin\theta & \cos\theta \end{pmatrix} \begin{pmatrix} l' \\ m' \end{pmatrix} \tag{1.74}$$

If the original visibility is given by the van Cittert–Zernike theorem:

$$\mu(u,v) = \int_{\mathbb{R}^2} I(l,m) e^{-2\pi i(lu+mv)} \mathrm{d}l\, \mathrm{d}m\,, \tag{1.75}$$

then the visibility of the rotated source is given by:

$$\mu'(u,v) = \int_{\mathbb{R}^2} I'(l,m) e^{-2\pi i(lu+mv)} \mathrm{d}l\, \mathrm{d}m$$

$$= \int_{\mathbb{R}^2} I(l',m') e^{-2\pi i([l'\cos\theta - m'\sin\theta]u + [l'\sin\theta + m'\cos\theta]v)} \mathrm{d}l'\, \mathrm{d}m'$$

$$= \int_{\mathbb{R}^2} I(l',m') e^{-2\pi i(l'[u\cos\theta + v\sin\theta] + m'[-u\sin\theta + v\cos\theta])} \mathrm{d}l'\, \mathrm{d}m'$$

$$= \mu(u\cos\theta + v\sin\theta, -u\sin\theta + v\cos\theta) = \mu\left(\begin{pmatrix} \cos\theta & +\sin\theta \\ -\sin\theta & \cos\theta \end{pmatrix} \begin{pmatrix} u \\ v \end{pmatrix}\right) =: \mu(u',v')\,,$$

which is a simple rotation of the original visibility function. I will use this to estimate the position angles of the disks.

Chapter 2

Observations

2.1 Previous studies of DoAr 44

The object studied in this thesis, DoAr 44 = Haro 1-16, was discovered by Haro (1949) in the Ophiucus–Scorpius region, shortly after the discovery of the region by Struve and Rudkjøbing (1949). It was later included in the catalogue by Dolidze and Arakelyan (1959). Other designations for the same object are V2062 Oph in the traditional variable star GCVS notation (Kukarkin et al., 1971), IRAS 16285-2421, 2MASS J16313346-2427372, ROX-44.

Montmerle et al. (1983) performed an X-ray survey of the ϱ Ophiuchi region using the Einstein Observatory (Giacconi et al., 1979). They found 50 new X-ray sources, many of which corresponded to known T Tauri stars. They also found that these X-ray sources were highly variable on the scale of days, due to the accretion variability.

Nuernberger et al. (1998) performed a radio survey of the sources discovered by Montmerle et al. (1983) using the 30-m Institut de Radioastronomie Millimétrique (IRAM) single-dish radio telescope, at 1.3 mm. They concluded that the disk mass of DoAr 44 is $16.6 M_{\mathrm{Jupiter}}$.

McClure et al. (2010) performed Spitzer/IRS spectroscopy from 5–36 µm for up to 136 protoplanetary disks in Ophiuchus. They discovered a 30–40 au cavity in DoAr 44, based on the SED modeling, and categorized it as a classical T Tauri star and a Class II object, i.e., a pre-transitional disk. From the demographics of the disk population, they conclude that gap clearing by massive protoplanets is the best explanation for pre-transitional disks.

Ricci et al. (2010a) performed a 3.3 mm continuum survey of the ϱ-Ophiuchi region, including DoAr 44, using the Australia Telescope Compact Array (ATCA), measuring the spectral indices between 1.3 mm and 3.3 mm fluxes. They concluded that the spectral indices of Ophiuchus sources is not statistically different from the sources in the Taurus / Auriga star forming region, which they surveyed using the PdBI in a previous study (Ricci et al., 2010b), but differ significantly from the interstellar medium.

Andrews et al. (2010) then performed an interferometric survey using the SMA at 40 au resolution in the Ophiuchus star forming region. They tried fitting their results using the common Lynden-Bell and Pringle (1974) prescription:

$$\Sigma = \Sigma_0 \left(\frac{R}{R_c}\right)^{\gamma} \exp\left[-\left(\frac{R}{R_c}\right)^{2-\gamma}\right], \tag{2.1}$$

where Σ_0, R_c, γ are some parameters. This function has good analytical properties with respect to the evolution equations mentioned in Chapter 1. However, for several disks they found a poor fit, which could be explained by the fact these disks (DoAr 44, SR 21, SR 24 and WSB 60) had

a large central cavity. This was the first *spatially* resolved observation of the cavities predicted by SED modeling. They continued their investigation into transitional disks with an additional SMA study (Andrews et al., 2011), finding that the dust in the cavity has been depleted by 4–6 orders of magnitude with respect to the Lynden-Bell and Pringle (1974) profile.

Espaillat et al. (2010) modeled Infra Red Telescope Facility (IRTF) 2.1–5.0 micron spectra with $R = 1500$ resolution, and also Spitzer spectra, using analytical temperature prescriptions. They derived a higher accretion rate of $\dot{M} = 9.3 \cdot 10^{-9}\, M_\odot\, \mathrm{yr}^{-1}$. One of their conclusions is that within the 2 au radius, there is $M = 1 \cdot 10^{-8} M_{\mathrm{Jupiter}}$ of dust, corresponding to about $8 \cdot 10^{-7} M_{\mathrm{Jupiter}}$ of gas, assuming solar metallicity.

Bouvier et al. (2020b) obtained K-band (2 – 2.4 µm) continuum and Brγ line visibilites of DoAr 44 from VLTI/GRAVITY. They concluded that the Brγ emission is localised inwards of the continuum emission, suggesting that the optically thin gas flows, where the line emission is created are located within the truncation radius. They used the Lazareff et al. (2017) visibility models, using a point source, an elliptical Gaussian in place of the disk and a "halo". This halo represents all the incoherent emission from outside regions. They found the contribution of the ellipse to be 27 %, the star 67 % and the halo 6 %.[1]

Bouvier et al. (2020a) also performed multicolor photometry from Las Cumbres Observatory Global Network (LCOGT) and spectroscopy using the Canada-France-Hawaii Telescope (CFHT). They found a rotation period of $P = 2.96$ days, a stellar inclination of $i = (30 \pm 5)°$, which is in agreement with the inclination of the ellipse modeling (supposedly) the inner rim seen by VLTI. From their Hα, Hβ, Paβ, Brγ spectra, they conclude that the spectral line profiles are best explained as a combination of funnel flows along magnetic field lines and disk winds, similar to the ones described by radiative transfer models by Kurosawa et al. (2011), where the "funnel" flows cross the line of sight. For some spectral lines, this behaviour is periodic (He I), and for others, they report a more complicated, chaotic variability (Brγ). Bouvier et al. (2020a) derived an accretion rate of $\dot{M} = 6.5 \cdot 10^{-9}\, M_\odot\, \mathrm{yr}^{-1}$.

The Ophiuchus DIsc Survey Employing ALMA (ODISEA) project by Cieza et al. (2019) is a series of publications detailing ALMA Band 6 ($\lambda = 1.3$ mm) observations of Ophiuchus disks selected using Spitzer IR excesses. It presented continuum observations and observations in the C-O $v = 0, J = 2 - 1$ line at 28 au resolution for up to 133 disks, spatially resolving 60 of them, including DoAr 44. They estimated the dust masses of these disks using a simple proportionality to the observed flux density F_ν:

$$M_{\mathrm{dust}} = \frac{d^2 F_\nu}{\kappa_\nu B_\nu(T_{\mathrm{dust}})}\,, \tag{2.2}$$

where d is the distance derived by Gaia, B_ν is the Planck function, T_{dust} is assumed to be uniformly 20 K and κ_ν is taken as a power-law from Beckwith et al. (1990),

$$\kappa_\nu = 0.1\,\mathrm{cm}^2\mathrm{g}^{-1} \left(\frac{\nu}{1\,\mathrm{THz}}\right)^\beta\,, \tag{2.3}$$

which for a common value of $\beta = 1$ and the ALMA Band 6 ($\nu = 225$ GHz) gives a fixed value of $0.023\,\mathrm{cm}^2\mathrm{g}^{-1}$.[2]

[1] In this thesis, a very similar analysis is performed on the same dataset, available from the ESO archive (Delmotte et al., 2006), as a stepping stone for our radiative transfer models – only Bouvier et al. (2020b) used wavelength dependent elliptical gaussians, and I used wavelength independent elliptical disks. The resulting fractional I obtained are within 1% of the ratios by Bouvier et al. (2020b), which is natural, as we used the same data and a very similar model.

[2] You will see the approach taken in this work is a bit more sophisticated, taking into consideration the dust

They conclude that the Ophiuchus (ϱ Ophiuchi) star forming region has more massive disks compared to the Taurus, Auriga, Chameleon, σ-Orionis and Lupus star forming regions, and together with the Taurus region, they are also the youngest (1–2 Myr).

The second paper in the series, ODISEA II (Zurlo et al., 2020), explored the effect of multiplicity on disk properties, because of the about 130 disks, about 20 of them were found to harbour a double star.

The third paper in the series, ODISEA III (Cieza et al., 2021) returned to the Ophiuchus sample at 3–5 au resolution in ALMA Band 6. This provided us with the highest resolution view of DoAr 44 up to date. Combined with the DSHARP survey (Andrews et al., 2018), where DoAr 44 was not included, the following evolutionary sequence emerged:

1. The youngest disks form with a monotonic density profile with no visible dips, rings or gaps.
2. Proto-planets start to grow, resulting deep narrow gaps and clear rings.
3. Gas giants start to accrete gas, carving wide gaps, dust accumulates at the inner edge of the rings.
4. The inner disk is cleared, forming a large inner cavity. The dust from the outer regions accumulates at the inner edge of the outer ring.
5. The inner disk is completely dissipated, and the dust from the outer disk has formed a narrow ring.

DoAr 44 would fit into the 4th stage of this process.

The Disks around T Tauri Stars with SPHERE (DARTTS-S) (Avenhaus et al., 2018) was a study of 8 prominent T Tauri disks, using the VLT/SPHERE/IRDIS instrument, operating between 0.9–2.3 microns, in the differential polarimetric imaging mode, with a coronagraph obscuring 0.1″ around the central star. These images can be seen in Figure 2.6, showing the scattered light from the surface of the disk. Surprisingly, they found no correlation of the scattered light, either to the stellar mass or to mm-fluxes.

Casassus et al. (2018) focused on the misalignment of the inner and outer disks of DoAr 44. This is somewhat visible in the radio continuum, but it is very apparent in the polarimetric images. They estimated a tilt of 30° of the inner disk with respect to the outer disk using radiative transfer modeling.

Arce-Tord et al. (2023) studied these same SPHERE images together with the ALMA Band 6 images from ODISEA and new Band 7 images, specifically of the DoAr 44 system. They derived a relative inclination of 21°.[3]

Leiendecker et al. (2022) performed a study of DoAr 44, together with the better known system HD 163296. They estimated a dust mass of 0.3 M_{Jupiter}, corresponding to 21.5 M_{Jupiter} mass of gas. They tried explaining the ring morphology alternative scenarios, such as a break up of two large bodies. They also estimated the mass of a hypothetical planet needed to clear the inner disk at 0.5 to 1.6 M_{Jupiter}.

density distribution, the temperature profile, the dust mineralogical composition, scattered light and a variety of other factors.

[3]I cannot check these more complex geometries due to the technical limitations of our tools. However, I have calculated the inclinations of the inner accretion region and of the outer disk separately, and the relative inclination of about 10° to 20° appears to be correct, if the inner disk shares the the geometry of the accretion region. Definitive answers would be provided if the proposed ALMA observation detailed in the Appendix A were to be done.

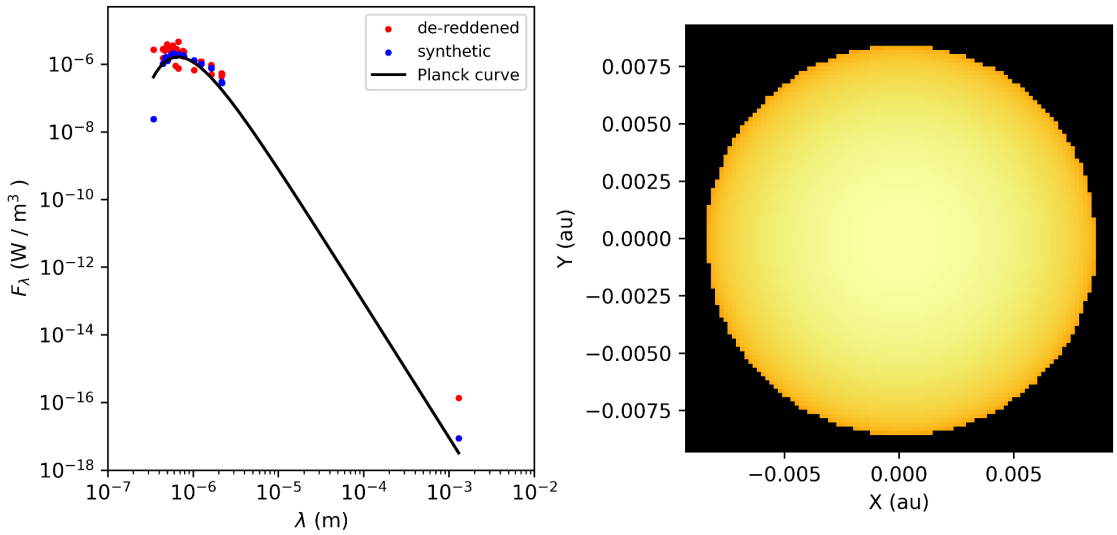

Figure 2.1: **Left**: Broadband SED, cropped to the band where the central star dominates. The red points show the data after de-reddening, i.e., after correcting for extinction. **Right**: A synthetic image of the young star.

2.1.1 My previous work on DoAr 44

This thesis is a logical continuation of my Student's Faculty Grant (SFG) project (Souza de Joode, 2022), which started in the Autumn of 2022. This previous work dealed with C-O $v = 0 J = 3-2$ line measurements to estimate the star mass, moment maps, analytical models of the SED and some very preliminary interferometric fits of the ALMA data using `pyshellspec`. Moreover, there are some descriptions of the ALMA `MeasurementSets` and a series of technical issues that had to be overcome to proceed with the main part of the work, which is presented in this thesis.

Distance, absorption and de-reddening

The distance to DoAr 44 was determined in Gaia DR2 (Gaia Collaboration, 2018) as $d = 149.9 \pm 0.99$ pc, and in Gaia EDR3 (Gaia Collaboration, 2020) as 146.32 ± 0.49 pc. This places it in somewhat more distant regions of the ρ Ophiuchi molecular cloud.

The column densities in the **densest** part of the ρ Ophiuchu molecular cloud cause an immense extinction of $A_V = 50 - 100$ mag (Wilking et al., 2008), and exceed $A_V = 20$ mag in most areas (Ridge et al., 2006). However, DoAr 44 is located in a less dense "window", in between three of the largest clouds, with the densest cloud L1688 about 1° to the west, L1709 about 0.5° to the North and L1689 about 0.3° to the East. The extinction in this position is less than or approximately $A_V = 3$ mag from both Two Micron All Sky Survey (2MASS) and Infra Red Astronomical Satellite (IRAS) measurements (Ridge et al., 2006) – these values are however along the **entire** line of sight. The wavelength dependence, i.e. the reddening, was adopted from Sloan Digital Sky Survey (SDSS) measurements analyzed by Schlafly and Finkbeiner (2011), together with the distance-dependent extinction, which is about $A_V = 2$ mag.

The γ velocity was determined by Miret-Roig et al. (2022) as $\gamma = -5.7\,\mathrm{km\,s^{-1}}$, which is consistent with the best fit γ velocities obtained by my models of the spectral lines.

2.2 VLT: Optical and IR spectra

The Very Large Telescope (VLT), operated by ESO is the largest optical and infrared astronomical facility, consisting of four 8.2-m Unit Telescopes (UTs) and four moveable 1.8-m Auxiliary Telescopes (ATs). Each of the four UTs is equipped with a variety of instruments, placed in the two Nasmyth foci (Nasmyth A and Nasmyth B), or in the Cassegrain, Coudé or interferometric foci. Most of the observation time is used in an observing mode, where the UTs operate independently, utilizing the instruments in the Nasmyth/Cassegrain foci.

These instruments include adaptive optics imagers (HAWK-I, VISIR, FORS2), both echelle (UVES, FLAMES/GIRAFFE, X-shooter, CRIRES) and integral-field spectrographs (MUSE, FLAMES/ARGUS), high-contrast coronographs (SPHERE), polarimeters and others. A photograph of the facility can be seen in Figure 2.3.

For this study, we utilised the available VLT spectra of DoAr 44, that captured the Hα line. These can be seen in Figure 2.2. The Signal to Noise Ratio (SNR) for all of the observations is > 100, which means clear differences between the individual measurements are due to the intrinsic variable properties of the source.

Bouvier et al. (2020a) performed an investigation using their photometry from the LCOGT, and spectra from the CFHT. They report a variability of the spectral line which is very complicated, but its dominant frequency is consistent with the rotational period of the star.

In this work, I model the accretion region using stationary velocity and density profiles, meaning that it cannot, in principle, account for the transient variability of the spectral line profile, which seems to be connected to chaotic funnel flows. Therefore, we modeled separately the "extreme" X-shooter profile, and a "compromise" profile made by averaging the four measurements, and using the standard deviation of the mean as an artificial uncertainty of the compromise measurement.

The latter approach also has the benefit of relaxing the tight error-bars on the individual measurements, that were complicating the χ^2 optimization.

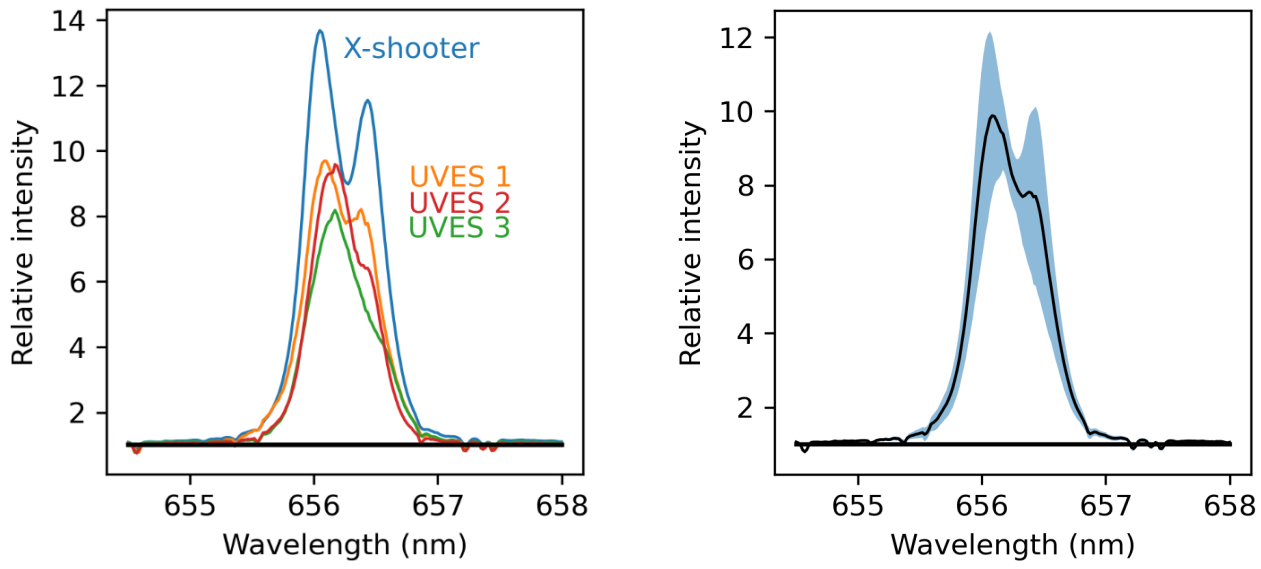

Figure 2.2: Available VLT/X-shooter and VLT/UVES spectra of DoAr 44 used in this work. The profiles are variable on the scale of a few days. I modeled both the extreme double-peaked X-shooter profile, and also an "average" profile that served as a steady-state simplification for my models.

2.3 VLTI: Optical interferometry

The VLTI coherently combines beams of light from the four UTs or the four ATs, providing a milli-arcsecond spatial resolution and an intermediate ($R = 5000$) spectral resolution. There are currently three operational VLTI instruments:

1. Multi-AperTure mid-Infrared SpectroScopic Experiment (MATISSE) (Lopez et al., 2022),
2. GRAVITY (GRAVITY Collaboration et al., 2017),
3. Precision Integrated-Optics Near-infrared Imaging ExpeRiment (PIONIER) (Le Bouquin et al., 2011).

The MATISSE operates in the infrared L, M, N bands, corresponding to 3.2–3.9, 4.5–5.0, and 8.0–13.0 microns respectively, with the spectral resolution $R \in (30; 5000)$. It is a four-way beam combiner, able to utilize both the UTs and the ATs. It reaches 3.5 mas resolution at the shortest wavelengths and 12.5 mas at the longest wavelengths.

GRAVITY is the K band instrument (2.0–2.4 micron), resolving 4–50 mas scales using the UTs and 2–140 mas scales using the ATs. Its spectral resolution is either 22, 500 or 4500.

PIONIER is a low spectral resolution instrument, which uses 1 or 6 spectral channels in the H band (1.5 – 2.4 micron). It was originally a visitor instrument, but now it is kept as a part of the facility.

2.4 ALMA: Radio interferometry

The Atacama Large Millimeter/submillimeter Array (ALMA) is the world's largest millimeter and sub-millimeter observatory, consisting of 66 antennas:

- 50 main 12-m antennas, provided jointly by ESO and National Radio Astronomy Observatory (NRAO),
- The Atacama Compact Array (ACA), (Iguchi et al., 2009) , used to provide low frequency Fourier components consisting of
  - 12 7-m antennas,
  - 4 12-m Total Power Array (TP) antennas.

ALMA operates in 10 configurations, C-1 to C-10. The C-1 configuration is the most compact, with the longest baseline of 160 meters, and C-10 is the most extended configuration, spanning over 16 kilometers. The 54 12-m antennas can be placed on 192 concrete antenna foundations providing access to power, the LO signal and network connection (Chalmers et al., 2012).

Receivers

ALMA offers 10 spectral bands, spanning a range of wavelengths from 0.32 to 8.6 mm, corresponding to a range of frequencies from 950 to 30 GHz. ALMA is operational since 2013 and is under constant development: the first observations in ALMA Band 1 are being performed as of writing this work (March 2024). Band 10 observations on long baselines will start being performed from October 2024 (see Appendix A). The limits of each spectral band are determined mostly by the atmospheric transmission windows.

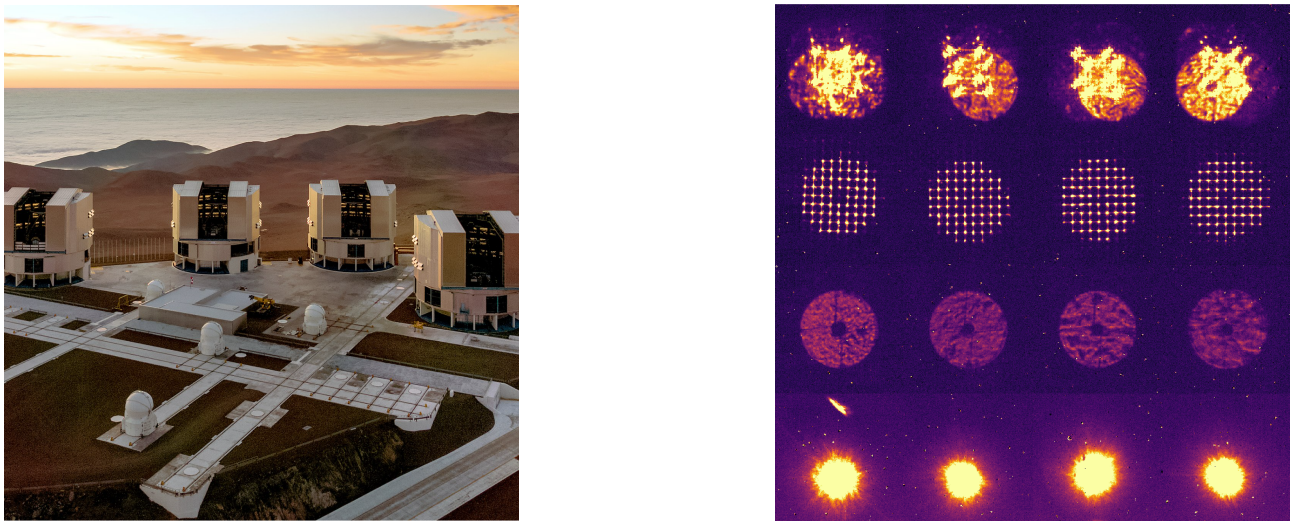

Figure 2.3: **Left**: The Very Large Telescope of the European Southern Observatory at Cerro Paranal. The spectra were obtained by UVES located in the Nasmyth B focus of UT2 (Kueyen), the second large building from the left, and X-shooter in the UT3 Cassegrain focus (third large building from the left). The SPHERE instrument, the adaptive optics coronagraph and polarimeter, is located in the Nasmyth A focus of UT3. The interferometer GRAVITY is located in the flat beam combiner building in the middle. **Right**: A raw uncalibrated frame from the VLTI/GRAVITY instrument, from which the interferometric observables are extracted by the pipelines accessible through `esoreflex` (Freudling et al., 2013).

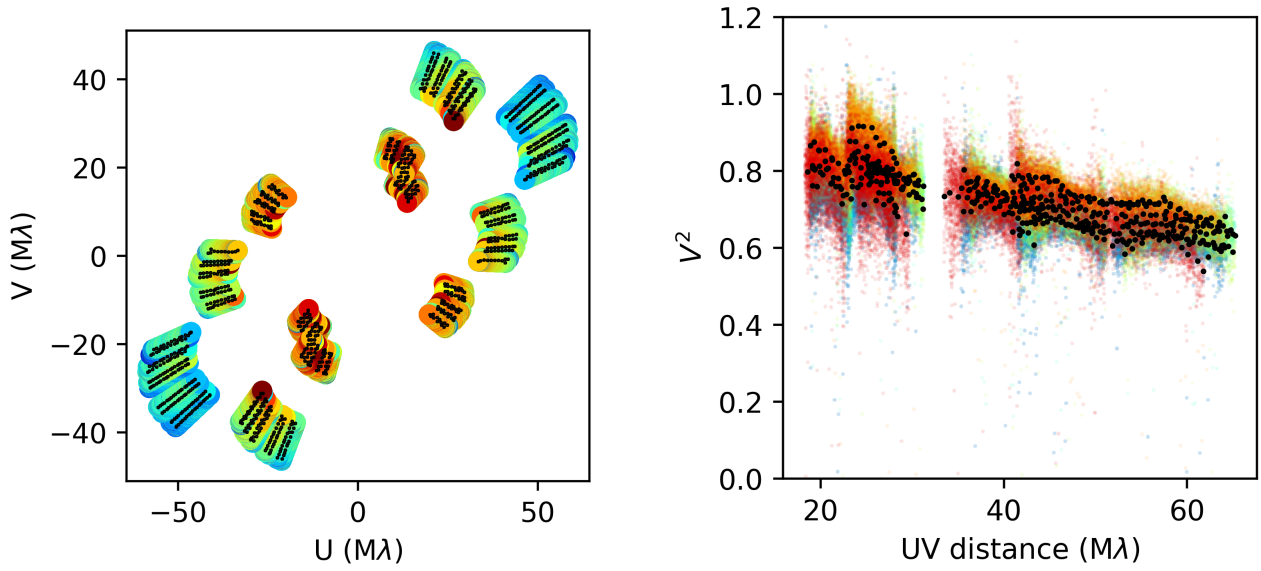

Figure 2.4: Available VLTI/GRAVITY interferometric visibilities of DoAr 44. **Left**: V^2 plotted as points in the uv (Fourier) plane. The color encodes the square of the visibility (red are large values, blue are small values). The black dots form a smaller dataset, obtained by rounding the decimal expansion of the u and v coordinates, averaging the coordinates of the points that fell into each bin and averaging the visibilities with the weights given by the uncertainties. This smaller dataset was used to converge my models. **Right**: The same values now plotted against a single radial coordinate $\sqrt{u^2+v^2}$. Note that the averaging and binning must not be performed in this radial coordinate, as all information about the position angle would be lost. From the theoretical point of view, the graph on the right figure is not a mathematical function, as for a single value of $\sqrt{u^2+v^2}$ many visibility values can be measured, as V^2 is inherently a two-dimensional function.

Each spectral band has a dedicated receiver cartridge, so it is not possible to observe simultaneously in multiple spectral bands. Each receiver operates at cryogenic temperatures and detects two orthogonal linear polarisations. The design of the receiver cartridges varies significantly depending on the frequency band, as every wavelength range presents its own challenges.

Down-conversion

The RF signal is down-converted into an IF. This is achieved by mixing with the LO signal, which is distributed via optical fibres from four centers on the ALMA site: two for the 12-m array, one for the 7-m ACA and one for the TP Array. The demands on the LO signal are stringent, as the 16-km array has to be synchronised at the 10 femtosecond level (Shillue et al., 2011).

Each receiver outputs two orthogonal components of the signal (voltage), X, Y, which are proportional to the measured components of the electric field in the receiver E_x, E_y.

Correlation

The ALMA correlator phase-shifts, multiplies and integrates these output voltages to give raw (uncalibrated) complex visibilities. The time integration is typically 6 seconds. For the full-polarization setup, it is capable of utilizing all the possible independent pairs, i.e., $\langle X_1 X_2^* \rangle, \langle X_1 Y_2^* \rangle, \langle Y_1 X_2^* \rangle, \langle Y_1 Y_2^* \rangle$. These are related via the complex gains, G_X, G_Y to the components of the Stokes parameters, that describe the complex amplitude of the electric field of the incoming wave:

$$I = \langle E_x^2 \rangle + \langle E_y^2 \rangle \,, \tag{2.4}$$

$$Q = \langle E_x^2 \rangle - \langle E_y^2 \rangle \,, \tag{2.5}$$

$$U = \langle E_{x'}^2 \rangle - \langle E_{y'}^2 \rangle \,, \tag{2.6}$$

$$V = \langle E_L^2 \rangle + \langle E_R^2 \rangle \,, \tag{2.7}$$

where E_x, E_y are measured in a local Cartesian basis, $E_{x'}, E_{y'}$ are in a Cartesian basis rotated by $\pi/4$ and E_R, E_L are in a circular basis. The relation to the raw correlations is the following:

$$\begin{pmatrix} I \\ Q \\ U \\ V \end{pmatrix} = \frac{1}{2} \begin{pmatrix} 1 & 0 & 0 & 1 \\ \cos 2\psi & -\sin 2\psi & -\sin 2\psi & -\cos 2\psi \\ \sin 2\psi & \cos 2\psi & \cos 2\psi & -\sin 2\psi \\ 0 & -i & i & 0 \end{pmatrix} \begin{pmatrix} \langle X_1 X_2^* \rangle / (G_X G_X^*)_{12} \\ \langle X_1 Y_2^* \rangle / (G_X G_Y^*)_{12} \\ \langle Y_1 X_2^* \rangle / (G_Y G_X^*)_{12} \\ \langle Y_1 Y_2^* \rangle / (G_Y G_Y^*)_{12} \end{pmatrix} , \tag{2.8}$$

where ψ is the parallactic angle measured between the zenith, the object, and the celestial pole — this angle is easily calculated from the time of the observation and the coordinates of the object. The terms in the vector on the right-hand side can be though of as calibrated visibilities, which should be very close to the theoretical visibilities calculated as the Fourier transform of the source intensity.

Our measurement, as is the case with the majority of ALMA measurements, utilizes only the $\langle X_1 X_2^* \rangle$ and $\langle Y_1 Y_2^* \rangle$ components. Notice from the Equation 2.8, that having just the $\langle X_1 X_2^* \rangle$ and $\langle Y_1 Y_2^* \rangle$ components, only the Stokes I component is recoverable. The $\langle X_1 X_2^* \rangle$ and $\langle Y_1 Y_2^* \rangle$ visibilites for DoAr 44 are shown on Figure 2.5.

Calibration

The central problem of calibration is the quantification of the time-dependent, frequency-dependent, direction-dependent complex gains. These gains largely antenna dependent, and can be separated into $G_1\,, G_2$, and partly baseline-dependent:

$$(GG^*)_{12} = G_1(t)G(t)_2^* G(t)_{12}\,,$$

where the "mixed" residual G_{12} can[4] be represented as having unit magnitude, and typically has a small phase ($\sim 1\%$ of the phases of G_1 and G_2). These gains are obtained by measuring a known source, like a quasar or a solar system object.

Triple products and closure phases If we neglect this baseline-dependent contribution, we can derive an interesting result. Lets denote the theoretical undisturbed visibility:

$$\mu_{X12} = \langle E_{X1} E_{X2}^* \rangle\,,$$

which should correspond to the first value of the vector in Equation 2.8. Now, let us assume some disturbance (attenuation or amplification and phase shift, represented by $G_{X1} \in \mathbb{C}$, affects the measured value of E_{X1}, and similarly for $G_{X2} \in \mathbb{C}$ for the second antenna. The observed visibility on this baseline would then be:

$$\mu'_{X12} = \langle G_{X1} E_{X1} G_{X2}^* E_{X2}^* \rangle\,, = G_{X1} G_{X2}^* \mu_{X12}\,.$$

If we include a third antenna, affected by a gain G_{X3}, we can calculate the other two perturbed visibilities:

$$\mu'_{X23} = \langle G_{X2} E_{X2} G_{X3}^* E_{X3}^* \rangle\,, = G_{X2} G_{X3}^* \mu_{X23}\,.$$

$$\mu'_{X31} = \langle G_{X3} E_{X3} G_{X1}^* E_{X1}^* \rangle\,, = G_{X3} G_{X1}^* \mu_{X31}\,,$$

If we then calculate the product of these three complex visibilities, we get the following result:

$$T'_3 = \mu'_{X12}\mu'_{X23}\mu'_{X13} = G_{X1}G_{X2}^*\mu_{X12}G_{X2}G_{X3}^*\mu_{X23}G_{X3}G_{X1}^*\mu_{X31} = \tag{2.9}$$

$$= |G_{X1}|^2|G_{X2}|^2|G_{X3}|^2\mu_{X12}\mu_{X23}\mu_{X31} = |G_{X1}|^2|G_{X2}|^2|G_{X3}|^2 T_3\,, \tag{2.10}$$

which demonstrates that the antenna-based phase disturbances do **not** affect the phase of the so-called **triple product**, and the "invariant" quantity $\arg(T_3)$ is called the **closure phase**.

This technique can also be used in optical/IR interferometry, as both $|T_3|$ and $\arg(T_3)$ are measurable quantities. Specifically, at a given moment, the VLTI generates $\binom{4}{2} = 6$ squared visibility measurements and $\binom{4}{3} = 4$ closure phases, either from the four UTs or from the four ATs. On the other hand, typical ALMA calibration procedures do not result in closure phases, but calibrate the visibility phases directly for each baseline.

The antenna-based gains are themselves composed of a variety of effects:

1. The attenuation (absorption, scattering) and phase shifts caused by the troposphere,
2. the response of the single-dish antenna (the primary beam),
3. the bandpass (i.e., the frequency) response of the antenna.

The effects above are multiplicative, but there are a number of additional additive effects.

[4] I think

System Temperature Calibration

The monochromatic intensity I_ν is an intensive quantity, described by a function of position, direction and frequency: $I_\nu = I(x, y, z, \alpha, \delta, \nu)$ — and this holds also for the other monochromatic Stokes parameters (Q_ν, U_ν, V_ν). In a vacuum, they are all conserved along the line of sight. Particularly, for optically thick thermal emission, coming from a body having a single equilibrium temperature T, in the Rayleigh-Jeans regime and the Stokes I_ν component[5]:

$$I_\nu = \frac{2k_B T\nu^2}{c^2}\,. \tag{2.11}$$

This fact is used in radio-astronomy to define the *brightness temperature*:

$$T_b := I_\nu \frac{c^2}{2k_B\nu^2}\,, \tag{2.12}$$

regardless whether the body has a single temperature or is optically thick, whether the radiation is thermal, or the source is spatially resolved. Nevertheless, if these requirements are satisfied, the brightness temperature coincides with the temperature of the source. However, many other sources contribute to the total measured intensity — or equivalently and more commonly, the total temperature $T_{\rm tot}$:

$$T_{\rm tot} = T_b + T_{\rm CMB} + T_{\rm ISM} + T_{\rm trop} + T_{\rm spill} + T_{\rm loss} + T_{\rm rx}\,, \tag{2.13}$$

specifically:

1. T_b: the brightness temperature of the source — e.g., 6000 K for the optically thick solar photosphere, or the temperature of an optically thin medium (with the optical thickness τ), multiplied by the factor $(1 - e^{-\tau})$.

2. $T_{\rm CMB} = 2.726\,{\rm K}$, from the cosmic microwave background radiation.

3. $T_{\rm ISM}$: the temperature of both the foreground and background interstellar medium, multiplied by $(1 - e^{-\tau})$.

4. $T_{\rm trop}$: the temperature of the troposphere, times the factor $(1 - e^{-\tau_z H})$, where τ_z is the zenith optical thickness and H the air-mass. In the sub-mm domain, this is dominated by the water vapour content, thus the need for high-elevation desert environment. For high-frequency observations, the factor $(1 - e^{-\tau_z H})$ can be up to 0.7, thus contributing around 200 K ($300\,{\rm K} \cdot 0.7 = 210\,{\rm K}$).

5. $T_{\rm spill}$: spillover from the antenna side-lobes, reflections off the surroundings, etc.

6. $T_{\rm loss}$: noise temperature due the losses in the feed.

7. $T_{\rm rx}$: receiver noise temperature. This is partially mitigated by the helium cryogenic coolers, nevertheless, it can reach up to 2000 K in ALMA Band 10 due to the necessary amplifiers.

[5]Another assumption is that the observation spatially resolves the source, i.e., that in the source is larger than the synthesized beam of the interferometer, or the PSF in the case of direct imaging, so that the "dark sky" from the background does not contribute.

Imaging

In contrast to optical interferometers or radio interferometers with a small number of baselines, it has become possible and common to compute images out of visibilities observed by ALMA.

Two main approaches to the question of mapping the source intensity distribution emerged in radio astronomy: phased arrays and aperture synthesis interferometers.

The **phased array**, or beam-former approach was the first one to develop historically, as it is possible to implement with analogue technology and did not require a super-computer like the ALMA Correlator. A narrow beam is created by combining the signals from individual antennas, and is pointed electronically by introducing delays between the signals. By scanning this beam across the source, a map is obtained. An example of a traditional phased array radio telescope is Giant Ukrainian Radio Telescope (GURT), but also some of the best radio observatories such as the Low Frequency Array (LOFAR), or the precursors to the Square Kilometre Array (SKA).

The aperture synthesis interferometers directly measure the components of the Fourier image of the source by correlating the signals of each pair of antennas. This allows the entire image to be captured at once without scanning a narrow beam across the source. It also allows for the possibility of measuring the signals first and correlating them later: a technique employed by Very Long Baseline Interferometry (VLBI) arrays such as European VLBI Network (EVN), Very Long Baseline Array (VLBA), or famously the Event Horizon Telescope (EHT).

The result of a decade of pathfinders and precursors in the mm-domain, such as NOEMA, CARMA, Nobeyama Millimeter Array (NMA), and the SMA is the radio interferometer ALMA.

Without even considering real-world effects, such as atmospheric extinction, atmospheric phase changes, interstellar extinction, atmospheric emission, antenna temperature, and many other effects, we do not have access to the complete image even in theory, as we cannot sample the entire Fourier space by a finite number of antennas (without building a single large dish). The image that we obtain by simple Fourier inversion is "undeconvolved":

$$\boxed{I_\mathrm{d} = I(l,m) * D(l,m) = \mathcal{F}^{-1}\{S(u,v)\mu(u,v)\} = \int_{\mathbb{R}^2} S(l,m)\mu(l,m)e^{+2\pi i(lu+mv)}\mathrm{d}u\,\mathrm{d}v}\,, \quad (2.14)$$

where $D(l,m)$ denotes the so-called **dirty beam**, i.e., the asymmetric point-spread function corresponding to the sampling function $S(u,v)$, which is given by all of the present baselines (antenna pairs). This convolution of the dirty beam with the intensity on the sky is called the **dirty image**. Typically, $S(u,v)$ will be comprised of $N(N-1)/2$ $\delta-$functions, where N is the number of antennas. The dirty beam is known, as it is simply:

$$D(l,m) = \mathcal{F}^{-1}\{S(u,v)\}\,. \quad (2.15)$$

Typically for ALMA observations, $D(l,m)$ is approximated by an elliptical gaussian kernel, described by semi-major and semi-minor axes which are often given as the angular resolution. This kernel is surrounded with spiral-like tendrils and asymmetric rings, which make the dirty image $I(l,m) * D(l,m)$ impossible to safely interpret. The gaussian kernel on its own is called the **clean beam** or the **synthesized beam**.

Performing a deconvolution on the vast amounts of data was possible, yet very impractical, until the discovery of the CLEAN algorithm by Högbom (1974). The Högbom CLEAN algorithm looks for the brightest pixel in a selected region of the dirty image $I_\mathrm{d} = I(l,m) * D(l,m)$, and subtracts a fraction (typically less than 0.1 for safety) of the dirty beam from the location centered at the brightest pixel. The process continues on the residual image, until the

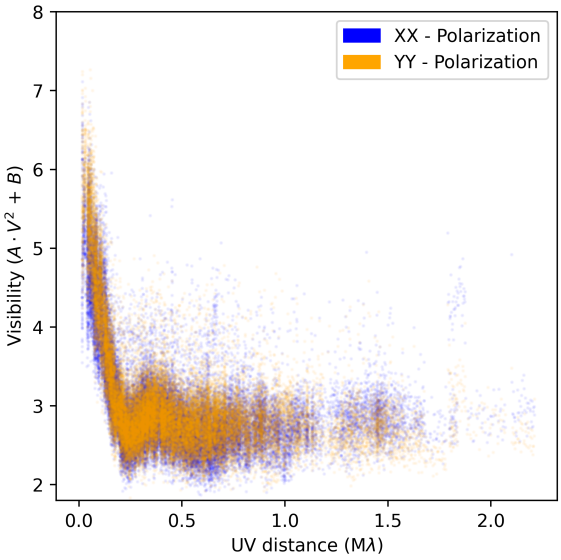

Figure 2.5: Squared visibilites for both polarizations (XX, YY) of the ALMA observation of DoAr 44. Equation 2.8 tells us that to obtain the Stokes I component, the correct procedure is simply adding the two signals. As there is no reason to expect a polarized signal, and no significant difference is discernible between the two polarizations, I only use the Stokes I component. This is common practice for such observations.

residual image does not show any structure and has reached the noise level. The image is then represented by a collection of delta functions, which can be convolved again with the elliptical gaussian kernel without the side-lobes (i.e., the clean beam), or presented in itself. Other implementations (most commonly by Schwab (1984)) perform these subtractions both in the image space and in the Fourier space, in so-called minor and major cycles, increasing the efficiency. CLEANed images of DoAr 44 can be found on Figure 2.6, and a list of all the available ALMA observations (as of May 2024) is presented in the Table 2.1.

These imaging algorithms, together with the calibration procedures, are implemented in the software package Common Astronomy Software Applications (CASA) (Bean et al., 2022). The synthetic images for this work were rendered in The Cube Analysis and Rendering Tool for Astronomy (CARTA) (Comrie et al., 2021).

Table 2.1: Currently available ALMA observations of DoAr 44. The values minRS and maxRS correspond to the minimum and maximum recoverable scales. The integration time is seconds is denoted by t.

Project code	Band	Release date	minRS	maxRS	t (s)
2019.1.01111.S	3	2022-08-13	0.251” = 36 au	3.80” = 550 au	490
2021.1.00378.S	4	2023-08-16	0.210” = 31 au	3.94” = 575 au	73
2018.1.00028.S	6	2020-11-30	0.026” = 4 au	0.64” = 93 au	2830
2012.1.00158.S	7	2015-08-19	0.229” = 33 au	1.98” = 290 au	2056
2019.1.00532.S	7	2022-06-08	0.168” = 25 au	2.70” = 390 au	2570
2019.1.00532.S	7	2023-09-06	0.023” = 3.5 au	0.56” = 81 au	4391
2021.1.00378.S	8	2023-09-01	0.154” = 22 au	2.36” = 345 au	113

2.5 Spectral Energy Distribution

The measurements of the SED were taken from the following surveys, publications and catalogues, using Vizier (Ochsenbein et al., 2000) and other access points:

- SkyMapper catalogue (Bessell et al., 2011),
- The XMM-Newton Optical Monitor Serendipitous Source Survey Catalogue (Page et al., 2012),
- The Guide Star Catalog II (Lasker et al., 2008),
- AAVSO Photometric All Sky Survey (APASS) (Henden et al., 2016),
- The Sloan Digital Sky Survey (SDSS) (York et al., 2000),
- The 2MASS (Skrutskie et al., 2006),
- The Pan-STARRS survey (Kaiser et al., 2002),
- The Gaia satellite (Gaia Collaboration, 2018, 2020),
- The ASAS-SN catalogue (Jayasinghe et al., 2018),
- The United Kingdom Infrared Telescope (UKIRT) (Hewett et al. (2006), Lawrence et al. (2007)),
- The Wide-field Infrared Survey Explorer (WISE) (Wright et al., 2010),
- Spitzer/IRAC (Fazio et al., 2004), Spitzer/MIPS instruments (Rieke et al., 2004),
- The IRAS satellite (Neugebauer et al., 1984),
- The AKARI satellite (Takita et al., 2010),
- The Herschel/PACS (Billot et al., 2006), and Herschel/SPIRE instruments (Griffin et al., 2010),
- The James Clerk Maxwell Telescope (JCMT) (Mohanty et al., 2013),
- ATCA (Ricci et al., 2010a).

Also the integrated ALMA photometry was used, together with the interferometric observations described below. The X-ray data from Montmerle et al. (1983) were not interpreted, as the emission formed in non-LTE conditions, which is outside of the approximations of our models.

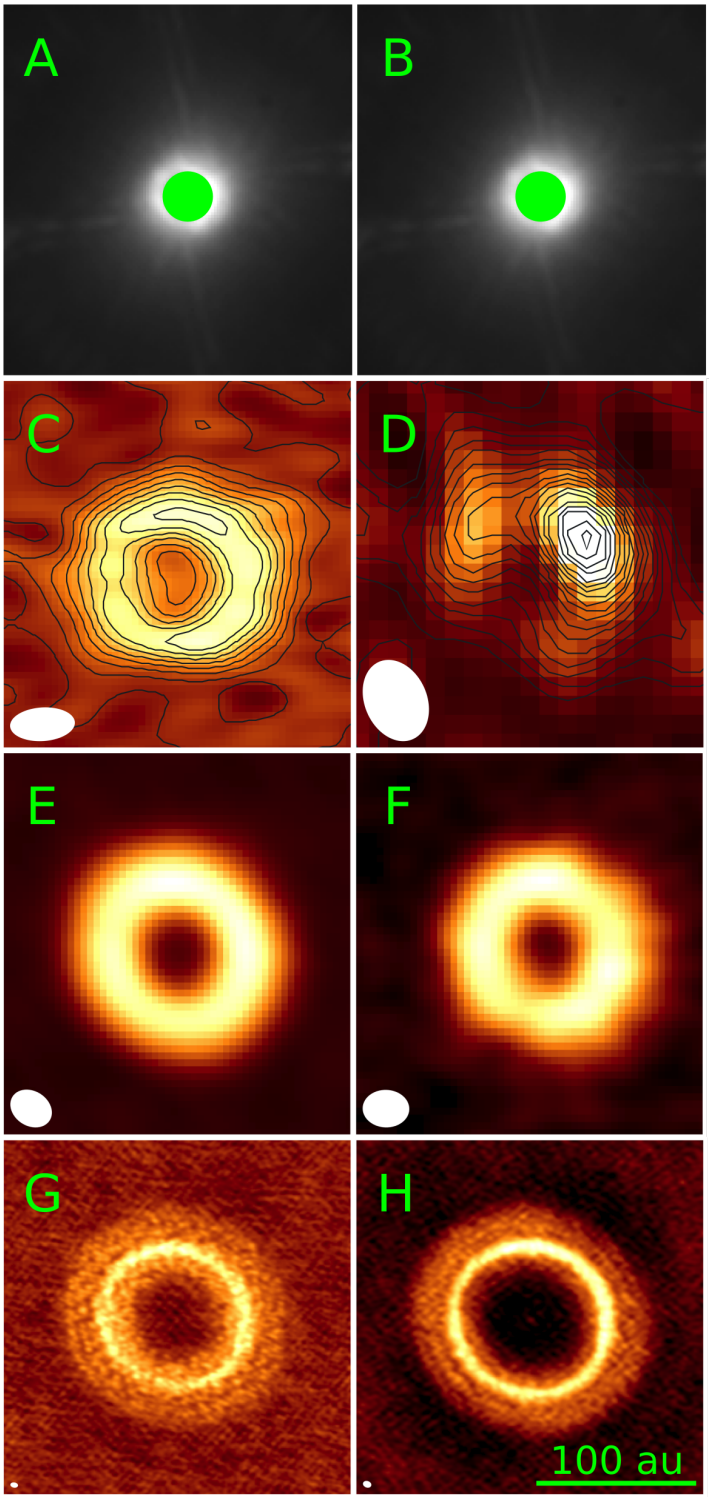

Figure 2.6: A comparison of available spatially resolved observations of DoAr 44. **A**: VLT/SPHERE/IRDIS Channel 1. **B**: VLT/SPHERE/IRDIS Channel 2. **C**: ALMA Band 3. **D**: SMA at 346 GHz. **E**: ALMA Band 8. **F**: ALMA Band 7. **G**: ALMA Band 7 (extended). **H**: ALMA Band 6 (extended). The SPHERE images are in the H band, and correspond to perpendicular linear polarizations. The green circle on the SPHERE images is the 0.1" radial extent of the coronagraph. Contours are plotted over the low-resolution interferometric images. The synthesized beam is shown as a white ellipse (very small for plots G and H).

Chapter 3

Modeling

In this work, I present several radiative-transfer models of DoAr 44, used to understand the vast amount of available observations.

1. An inner accretion region model, on the scale of tens of solar radii, using:
   - VLT/UVES visible spectra,
   - VLT/XSHOOTER visible and near infrared spectra,
   - VLTI/GRAVITY H-band interferometric visibilities.
2. An outer disk model, on the scale of tens of astronomical units (i.e., about 200 times larger scale than the first model), using:
   - ALMA Band 6 and Band 7 radio interferometric visibilities,
   - ALMA Band 3 and Band 8 measurements used as photometry, due to their low spatial resolution,
   - VLT/SPHERE adaptive optics imaging.

Together, these models must be consistent with the broad band SED measurements, and should help us answer the following scientific questions:

1. For the inner region:

   Q1 Is matter being accreted onto the central star, or are we observing stellar winds?

   Q2 What is the geometry of the accretion region?

2. For the outer disk:

   Q3 Is the observed ring a surface density maximum or an observational effect? Is it really necessary to describe the large cavity between the inner disk and the outer ring as a drop in surface density?

   Q4 Does the observed ring coincide with a condensation line of a volatile, or must it be caused by an exoplanet?

3.1 Simple analytic models

Before we begin constructing radiative-transfer models that account for gas and dust density, chemical composition, Mie and Rayleigh scattering, various profiles of temperature, electron number density, complicated geometries, evaporation temperatures of different minerals and similar complexities of real protoplanetary disks, it will be useful to construct a few simple analytic models. With them, I aim to describe the observed interferometric visibilities. These models include:

1. A homogeneous ellipse described by two axes and a position angle, α, β, ω for both the VLTI/GRAVITY and ALMA (squared) visibilities, together with a halo in the background.

2. A homogeneous ellipse described by α, β, ω, together with a point source and a background halo for the VLTI/GRAVITY visibilities.

3. A thin elliptical ring with a background halo for the ALMA visibilities.

Similar models were used by Lazareff et al. (2017) to model VLTI/PIONIER visibilities of about 50 Herbig AeBe disks. The introduction of a halo allows us to lower the visibility at short baselines that are not sampled by the VLTI. However, this contribution is not merely a mathematical aid, but it is directly observed by coronagraphic measurements, such as VLT/SPHERE – see Figure 2.6. The three models can be described as follows:

$$\mu_1(u,v) = \frac{f_\mathrm{e}\mu_\mathrm{e}(u,v;\alpha,\beta)}{f_\mathrm{h}+f_\mathrm{e}} =: e\mu_\mathrm{e}(u,v;\alpha,\beta,\omega), \tag{3.1}$$

$$\mu_2(u,v) = \frac{f_\mathrm{s}+f_\mathrm{e}\mu_\mathrm{e}(u,v;\alpha,\beta,\omega)}{f_\mathrm{h}+f_\mathrm{e}+f_\mathrm{s}}, \tag{3.2}$$

$$\mu_3(u,v) = \sqrt{A+B\mu_\delta^2(u,v;\alpha,\beta,\omega)}\,, \tag{3.3}$$

where the visibility of an ellipse μ_e and of a δ-ring were derived as:

$$\mu_\mathrm{e}(u,v;\alpha,\beta,\omega) = \frac{2J_1(2\pi\sqrt{\alpha^2u'^2+\beta^2v'^2})}{2\pi\sqrt{\alpha^2u'^2+\beta^2v'^2}}\,, \tag{3.4}$$

$$\mu_\delta(u,v;\alpha,\beta,\omega) = J_0(2\pi\sqrt{u'^2\alpha^2+v'^2\beta^2})\,, \tag{3.5}$$

with the rotated aperture-plane coordinates given by:

$$\begin{pmatrix}u'\\v'\end{pmatrix} = \begin{pmatrix}\cos\omega & +\sin\omega\\ -\sin\omega & \cos\omega\end{pmatrix}\begin{pmatrix}u\\v\end{pmatrix}. \tag{3.6}$$

The parameters $f_\mathrm{e}, f_\mathrm{h}, f_\mathrm{s}$ denote the fractional contributions of the ellipse, halo and the star. The coordinates u, v and the angular sizes α and β are dimensionless, i.e., given in cycles per baseline and radians. As the separations of the telescopes (or antennas) is much larger than the wavelength which we are observing, we commonly use dimensionless units such as kλ or Mλ to denote a 10^3 or 10^6 cycles per baseline.

These parameters are estimated in Tables 3.1, 3.2 and 3.3.

These analytic models were used as a benchmark for the more complex radiative-transfer models, providing the angular extent of the observed structures as a guide. Also, they provided

Table 3.1: Best-fit parameters for the ellipse and halo model, suitable for the inner accretion region. The contribution of the always resolved halo (i.e.,a structure responsible for the visibility decrease at the shortest measured baselines) can be gauged from Equation 3.1, i.e., $\frac{f_e}{f_e+f_h} = e$. Rearranging, we obtain $\frac{f_h}{f_e} = \left(\frac{1}{e} - 1\right) \doteq 8.1\%$.

Parameter	value	σ
α (mas)	0.576	0.01
β (mas)	0.814	0.03
ω (°)	147.4	1.6
e	0.925	0.003

Table 3.2: Best-fit parameters for the star and disk and halo for the VLTI measurements of the inner accretion region. Notice that by separating the emission into a resolved component (ellipse) and unresolved component (star), the best-fit angular size of the ellipse increased. However, the relative contribution of the always resolved halo remains virtually unchanged: here I obtained $f_h = 7\%$ and in the ellipse and halo model I obtained 7%. The linear scale of the accretion region is 0.24 au.

Parameter	value	σ
α (mas)	1.243	0.2
β (mas)	1.663	0.3
ω (°)	147	2
f_s	0.68	0.1
f_c	0.24	0.1
f_h	0.072	0.005

a way to deal with the fully resolved component in the VLTI observations, and with the fact that the ALMA observations are in physical and not relative units. I rescaled the interferometric quantities in the following way:

$$V^2_{\text{new,in}} = \frac{1}{e^2} V^2_{\text{in}} , \tag{3.7}$$

$$T_{3,\text{new,in}} = \frac{1}{e^3} T_{3,\text{in}} , \tag{3.8}$$

$$V^2_{\text{new,out}} = -A + \frac{1}{B} V^2_{\text{out}} , \tag{3.9}$$

where $e = 0.925$ from the simplest ellipse model, and A, B are taken from the δ-ring model. The best-fit parameters and their uncertainties (68% confidence intervals of the marginalized posterior distributions) were obtained via a Markov Chain Monte Carlo (MCMC) simulation with an uninformative prior. In each case, two solutions were obtained for two position angles separated by 180°, and only the solution with $\omega < 180°$ was considered. Initial simulations were performed with 32 walkers and 10^4 steps. The marginalized posteriors were used as a starting value of the next iteration: these new simulations ran with 64 walkers for a total of 10^5 steps, with a 30% burn-in phase. All simulations were implemented using the `emcee` package (Foreman-Mackey et al., 2013).

The corner plots displaying the posterior probability distributions of the parameters are shown in Figure 3.1 for the model using an ellipse and halo, and in Figure 3.3 for the model using an ellipse, a star and halo. The corner plot for the δ-ring model posteriors used to model

Table 3.3: Best-fit parameters of the δ-ring and halo model suitable for ALMA visibilities. The A and B parameters were used to rescale the visibilities in physical units (Jy) into a unit-less quantity, which is the convention used in optical interferometry, as well as `Pyshellspec`, a radiative-transfer modeling tool.

Parameter	value	σ
α (mas)	329	1
β (mas)	304	1
ω (°)	156	2
$A(10^5\mathrm{Jy}^2)$	3.721	0.003
$B(10^5\mathrm{Jy}^2)$	3.827	0.012

the ALMA visibilites is shown in Figure 3.4.The best-fit ellipse and the synthetic visibilities for the ellipse and halo model are shown in Figure 3.2.

From all these models, I infer an inclination of the inner accretion region at $i = 40° \pm 3°$ and of the outer disk at $i = 22° \pm 1°$. The positions angles seem to be closely aligned, at $\omega = 147° \pm 2°$ for the inner accretion region and $\omega = 156° \pm 2°$ for the outer disk.

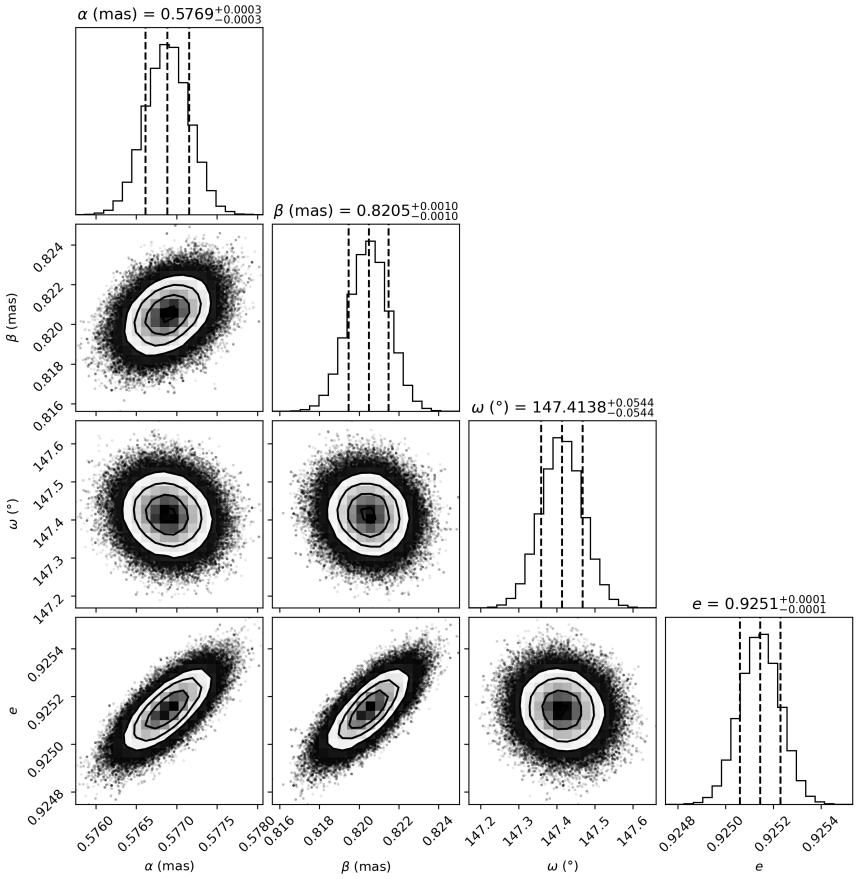

Figure 3.1: The joint posterior probability distributions and marginalized probability distributions for the parameters of the ellipse and halo model of DoAr 44. Notice that the angular scale (α, β) is very small, corresponding to about 18 – 25 solar radii (0.08 – 0.12 au). This is due to the fact that the circumstellar matter is modeled together with the central star, which contributes significantly at these wavelengths (2 µm). The parameter ω gives the position angle of the semi-minor axis of the ellipse. The parameter e quantifies the contribution of the halo.

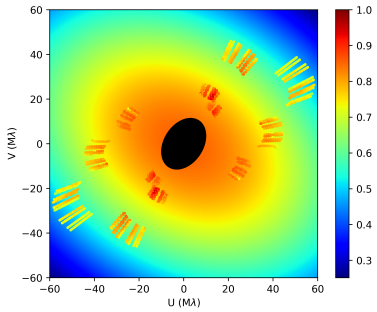

Figure 3.2: The best-fit for the VLTI visibilities in the uv plane, using a simple elliptical disk model. The orientation of the best-fit ellipse on the sky (north is up, east is left) is shown with the black ellipse in the center, with an arbitrary size. The VLTI/GRAVITY data are points on radial rays (the length of the segments is given by the wavelength range) extending over short arcs, whose azimuthal extent is given by the time of observation. They are colored based on the visibility value, with the model visibilites in the background.

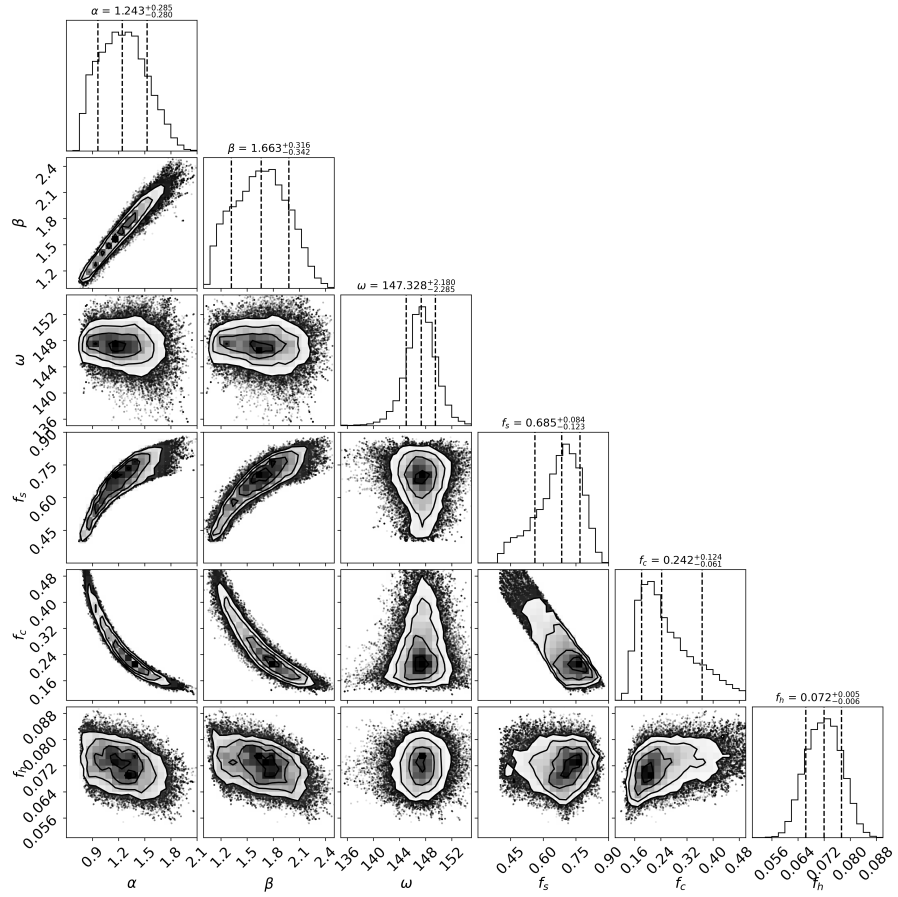

Figure 3.3: The joint posterior probability distributions and marginalized probability distributions for the parameters of the star and ellipse and halo model, based on VLTI/GRAVITY measurements of DoAr 44. Some of the parameters are strongly correlated, but this does not impact the utility of these calculations. The size of the ellipse (at 146 pc) is 0.2×0.24 au. The contribution of the always resolved halo is about 7%. The error-bars seem to be underestimated due to the fact that the model is too simple.

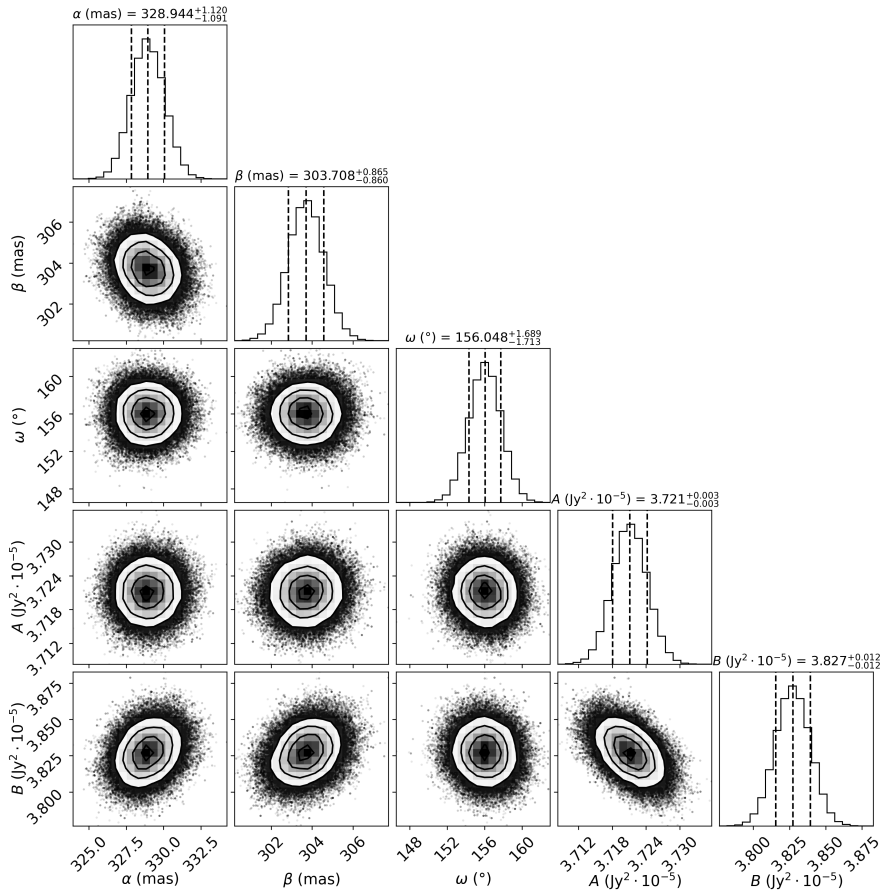

Figure 3.4: The joint posterior probability distributions and marginalized probability distributions for the parameters of the δ-ring model describing the ALMA Band 7 data. The parameters A and B play the role of the unresolved and always resolved emission. As I am using calibrated data, the visibilites were scaled to physical units (Jy), but I had to rescale them back, as `Pyshellspec`, our radiative-transfer tool expects visibilities normalized between 0 and 1.

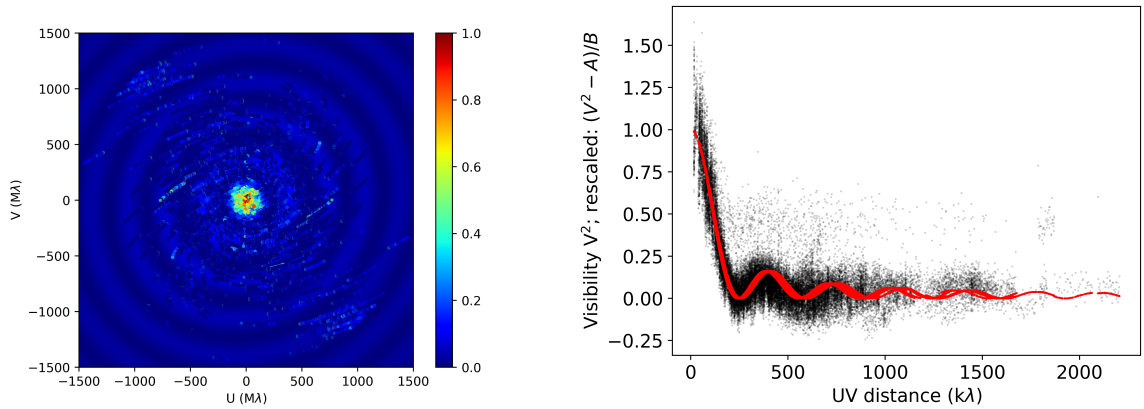

Figure 3.5: The best-fit δ-ring compared to the ALMA Band 7 data. **Left**: plotted in the Fourier plane. The background color represents the model visibility, and the colored points correspond to ALMA data. **Right**: plotted against the radial distance $\sqrt{u^2 + v^2}$ in the Fourier plane. The best-fit dimensions ($\alpha = 329$ mas, $\beta = 304$ mas) correspond to a projected ellipse of 44 times 49 au. However, it is known the real structure must be (nearly) circular, and so an inclination of $i = 22°$ is inferred.

3.2 `Pyshellspec` radiative-transfer models of the accretion region

The primary tool used to create all models for this work, `Pyshellspec`, was developed by Brož et al. (2021) and Mourard et al. (2018) to model the β LyræA system. `Pyshellspec` generates observables, such as interferometric visibilities and closure phases, spectral lines, light curves or broad band SEDs, based on synthetic images generated by `Shellspec`, a 3D radiative-transfer code by (Budaj and Richards, 2004). `Shellspec` is a tool used for modelling binary stars moving within circumstellar matter (i.e., gas and dust), and includes a series of parametrically defined objects, such as stars, rings, discs, jets and spherical shells, which shall be later described.

`Shellspec` integrates the radiative-transfer equation along the line of sight:

$$\mathrm{d}I_\nu = (\epsilon_\nu - \chi_\nu I_\nu)\mathrm{d}x\,, \tag{3.10}$$

where ϵ_ν, χ_ν are the total emissivity and the total opacity of the medium, I_ν is the specific monochromatic intensity, and $\mathrm{d}x$ is measured along the ray. The total opacity is given as the sum of the total opacity σ_ν and the absorption opacity κ_ν:

$$\chi_\nu = \sigma_\nu + \kappa_\nu\,. \tag{3.11}$$

`Shellspec` allows the user to include into κ_ν the following sources of absorption opacity:

1. Spectral line opacity,
2. HI (neutral hydrogen) bound-free opacity,
3. HI free-free opacity,
4. H^- (negative hydrogen ion) bound-free opacity,
5. H^- free-free opacity,

and the following sources of scattering opacity:

1. Thompson (i.e., low-energy Compton) scattering on free electrons,
2. Rayleigh scattering on neutral hydrogen,
3. Mie scattering and absorption on dust.

The dust opacities are summed over all the included dust species that are located in a cold enough region, allowing for dust condensation. The total emissivity is calculated as the sum of the thermal emissivity and the emission due to scattering:

$$\epsilon_\nu = \epsilon_\nu^{\mathrm{sc}} + \epsilon_\nu^{\mathrm{th}} = \epsilon_\nu^{\mathrm{sc}} + B_\nu(T)\kappa_\nu\,, \tag{3.12}$$

where B_ν is the Planck function.

One limitation is that `Pyshellspec` is a single-scattering radiative-transfer tool. That means that the stellar light scattered off the disk is accounted for in the synthetic image, but it does not handle multiple scatterings. That would be a task orders of magnitude more difficult.

For the evaluation of the goodness of fit, a χ^2 metric is defined:

$$\chi^2 = \chi^2_{\mathrm{SPE}} + \chi^2_{\mathrm{V2}} + \chi^2_{\mathrm{arg(T3)}} + \chi^2_{\mathrm{T3}} + \chi^2_{\mathrm{SED}}\,, \tag{3.13}$$

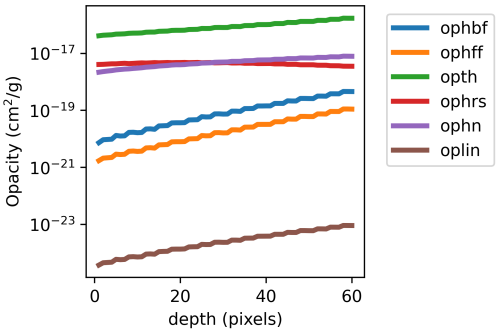

Figure 3.6: An example of the relative contributions of different sources of opacity along a line of sight. These are from top to bottom: the hydrogen bound-free opacity, the hydrogen free-free transitions, Thompson scattering, Rayleigh scattering, scattering on H^-, and the contribution of spectral lines.

where:

$$\chi^2_{\mathrm{SPE}} = \sum_{i=1}^{N_{\mathrm{SPE}}} \left(\frac{I^i_{\lambda,\mathrm{obs}} - I^i_{\lambda,\mathrm{syn}}}{\sigma_i} \right)^2 , \tag{3.14}$$

$$\chi^2_{\mathrm{V2}} = \sum_{i=1}^{N_{\mathrm{V2,in}}} \left(\frac{|V^i_{\mathrm{obs,in}}|^2 - |V^i_{\mathrm{syn,in}}|^2}{\sigma_i} \right)^2 + \sum_{i=1}^{N_{\mathrm{V2,out}}} \left(\frac{|V^i_{\mathrm{obs,out}}|^2 - |V^i_{\mathrm{syn,out}}|^2}{\sigma_i} \right)^2 , \tag{3.15}$$

$$\chi^2_{\mathrm{arg(T3)}} = \sum_{i=1}^{N_{\mathrm{arg(T3)}}} \left(\frac{\arg(T_3)^i_{\mathrm{obs}} - \arg(T_3)^i_{\mathrm{syn}}}{\sigma_i} \right)^2 , \tag{3.16}$$

$$\chi^2_{\mathrm{T3}} = \sum_{i=1}^{N_{\mathrm{T3}}} \left(\frac{|T_3|^i_{\mathrm{obs}} - |T_3|^i_{\mathrm{syn}}}{\sigma_i} \right)^2 , \tag{3.17}$$

$$\chi^2_{\mathrm{SED}} = \sum_{i=1}^{N_{\mathrm{SED}}} \left(\frac{F^i_{\lambda,\mathrm{obs}} - F^i_{\lambda,\mathrm{syn}}}{\sigma_i} \right)^2 . \tag{3.18}$$

However, the total χ^2 was not be optimized globally, as this is exceedingly difficult. The only contribution optimized globally was χ^2_{SED}, with the other contributions optimized separately for the accretion region, the inner disk and the outer disk.

3.2.1 The central star

The simplest element in our radiative-transfer model is the central star. A priori, the stellar parameters are not known. A synthetic stellar spectrum must be provided as a boundary condition. Such a stellar spectrum was obtained by interpolation of extensive grids of stellar atmospheres such as OSTAR and BSTAR (Lanz and Hubený, 2003, 2007), PHOENIX (Husser et al., 2013), AMBRE (De Laverny et al., 2012) and POLLUX (Palacios et al., 2010), using `pyterpol`, a tool developed in the work of Nemravová et al. (2016). The interpolation is performed in a 3-dimensional parameter space of the effective temperature T_{eff}, the (logarithm of) surface gravity $\log g$ and the metallicity Z. The initial stellar parameters have to be set up according to previously published works.

Stellar radius

The initial value of $R_\star = 1.85\,R_\odot$ was adopted from Ricci et al. (2010a), who adopted the spectral type from Andrews and Williams (2007) and the temperature scale (Schmidt-Kaler, 1982), to estimate the effective temperature. The luminosity was derived from 2MASS measurements

of the flux (Cutri et al., 2003) and estimates of extinction, yielding a rough estimate of the stellar radius. The study by Bouvier et al. (2020a) derived a value of $R_\star = (2.0 \pm 0.15) R_\odot$. It must be noted that the stellar properties were derived from the UV, visible and near-IR measurements, which are the most susceptible to interstellar absorption, which is substantial and also direction-dependent in these dense star forming regions.

Stellar mass

The initial estimate of the stellar mass $M_\star = 1.4\,M_\odot$ was adopted from the ODISEA (Cieza et al., 2021), which utilized ALMA Band 6 (1.3 mm) observations. My own analysis of the same C-O $v = 0\,, J = 3 - 2$ line measurements resulted in a stellar mass of $M_\star = (1.4 \pm 0.2)\,M_\odot$.

3.2.2 A disk model

A natural explanation for a double-peaked spectral line is a rotating disk. Similar double-peaked profiles are observed for example in Be stars, like Pleione (Gies et al., 1990) or ζ Tauri (Quirrenbach et al., 1994), and are generally explained by an edge-on optically thin rotating structure.

The primary object used to model disks is the called `NEBULA` in `Pyshellspec`, which is based on the thin disk from the introduction. The surface density dependence is parametrized by:

$$\Sigma(R) = \Sigma(R_{\rm innb}) \left(\frac{R}{R_{\rm innb}} \right)^{e_{\rm densnb}} = H(R) \varrho_0(R)\,, \tag{3.19}$$

where $\Sigma(R_{\rm innb})$, $R_{\rm innb}$, $e_{\rm densnb}$ are parameters, and:

$$H(R) = R \frac{c_s(R)}{v(R)}\,, \tag{3.20}$$

where $v(R)$ is the Keplerian velocity, and c_s is the speed of sound given by:

$$c_s = \sqrt{\frac{\gamma k_{\rm B} T(R)}{\mu}}\,, \tag{3.21}$$

where $\gamma = c_p / c_V$ is the ratio of specific heats, μ is the mean molecular weight. The temperature dependence is parametrized by:

$$T(R) = T_{\rm nb} \left(\frac{R}{R_{\rm innb}} \right)^{e_{\rm tempnb}}\,, \tag{3.22}$$

with $T_{\rm nb}$ and $e_{\rm tempnb}$ being parameters to be fitted.

However, as the inclination of the disk is low ($\approx 20°$ for the outer disk and $\approx 40°$ for the inner accretion region), the radial velocities produced by Keplerian rotation at the co-rotation radius $r_{\rm co}$, or even at the stellar photosphere are **never** enough to explain the spectral line width (see Figures 3.22, 3.23). Let us recall that the co-rotation radius is the location, where the Keplerian orbital period matches the period of rotation of the central star:

$$R_{\rm co} = \sqrt[3]{\frac{G M_\star P}{4\pi^2}}\,.$$

I obtained the rotation period of the star by constructing a Lomb-Scargle periodogram from sparse ASAS-SN measurements, obtaining $P = (2.96 \pm 0.01)$ days, which is in good agreement with photometric studies of this star (Bouvier et al., 2020a).

3.2.3 A bipolar jet model

During the early phases of star formation, powerful jets are sometimes observed, emerging from the poles of the protostar, for example in HH-30 Tauri.

The geometry of the `JET` object in `Pyshellspec` is defined using an inner and outer radius, and a cone opening angle, with respect to the polar axis of the star. The velocity profile in the `JET` is given as:

$$v(r) = v_{\rm jt}\left(1 - \frac{r_{\rm csh}}{r}\right)^{e_{\rm densjt}}, \tag{3.23}$$

while the density profile is given as:

$$N_e(r) \propto \rho(r) = \varrho_{\rm jt}\left(\frac{r_{\rm injt}}{r}\right)^2 \frac{v(r_{\rm injt})}{v(r)} \tag{3.24}$$

and

$$T(r) = T_{\rm jt} = \text{const}\,.$$

With these jets, I tried to match the double-peaked Hα profile measured by VLT/X-shooter, and simultaneously the VLTI/GRAVITY visibilities. The interferometric data primarily place a constraint on the total extent of the modeled structures. The powerful jets observed in the Herbig-Haro objects HH-30, HH-34, HH-47, HH-111 or others extend to parsec scales (i.e., 200 000 au!) and have opening angles of only several degrees (Reipurth et al., 1997). In addition, these jets are often strong radio sources, and would have very likely been detected by radio surveys. However, Herbig-Haro objects are objects more massive than classical T Tauri stars, and younger than Class II, so it is natural that we do not see these features in DoAr 44.

Protostellar jets are essentially outflows of matter that did not get accreted from the protoplanetary disk onto the young star, but was launched perpendicularly to the disk. The exact mechanism is under discussion. Jets commonly have thin envelopes with larger opening angles, that have been observed by ALMA in the spectral line of silicon oxide (SiO), transporting material from the inner to the outer disk. This could be the explanation for finding chondrules and Ca-Al inclusions in cometary material in the outer disk (Lee et al., 2022), a fact that is poorly explained by many models of the evolution of our own solar system.

In any case, a hot **collimated** optically thin jet inevitably produces two narrow emission lines (see Figure 3.27), as the bulk of gas is either moving quickly towards or away from the observer, which is in conflict with the VLT/X-shooter measurements, showing two broad overlapping profiles, and with the VLT/UVES profiles, that are single peaked.

It is of course impossible to fit two qualitatively different profiles with one stationary. I work with velocity fields, but I do not account for their evolution in time. However, a structure extending thousands of astronomical units with the $\sim 100\,\mathrm{km\,s^{-1}}$ velocities measured by the spectral profiles simply cannot evolve on the scale of a few days, which is the variability reported by Bouvier et al. (2020a). The spectral line emission must originate from radii, whose Keplerian orbital periods are comparable to the timescale of the variation of the spectral profile, i.e., a few tens of solar radii at most.

The temperature of these jets must be even higher than that of the stellar photosphere, to account for the fact that the prominent Hα line is about 8 – 10 times above than the surrounding continuum. This forced me to use temperatures of 7000 – 10000 K in the optically thin circumstellar matter.

A tempting deduction presents itself, in view of the fact that the blue-shifted peak of the VLT/X-shooter spectrum is stronger than the red-shifted peak: if the matter were to be

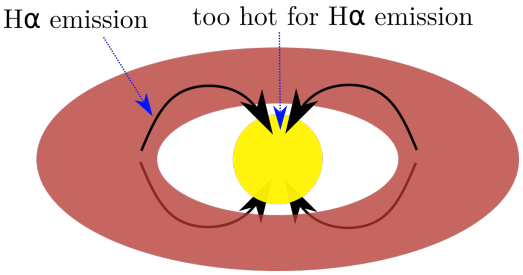

Figure 3.7: A possible geometry matching the observed Hα profile. Optically thin gas from the top of the disk approaches the observed (above). This produces a blue-shifted line. On the bottom of the disk, a similar flow occurs, but is partially obscured by the matter above. The matter falling back on the surface of the star could contribute less to the Hα emission due to the different temperature or optical depth.

partially translucent (i.e., $\tau \approx 1$) the front lobe of the jet would partially shadow the back lobe. Therefore, the front lobe would be the one responsible for the blue-shifted emission, and the back-lobe would be responsible for the red-shifted emission. Thus, it appears that the process originates from some **outflow of matter**, not an inflow, i.e., accretion.

However, we must proceed with caution. The jet object in `Shellspec` has a very simple radial velocity field. It cannot model the more realistic situation, that is shown in Figure 3.7. The flow is fed from the disk, rising in the z-direction at larger radii and falling onto the stellar surface at smaller radii. One can imagine the temperature being such that the flow produces the Hα emission while rising up from the mid-plane, as is for example too hot during the fall onto the star. Such a situation could produce a very similar spectral line profile as the out-flowing jets, while at the same time carrying matter towards the central star. As the tool I am using only allows for constant temperature profiles and a simple geometry, I did not perform any detailed calculations, but similar geometries are sometimes assumed in works on **magnetospheric accretion** (Bessolaz et al., 2008; Takasao et al., 2018; Li et al., 2022).

The largest issue with a model consisting of only optically thin matter is the conflict with the VLTI interferometric observations. These were taken in the 2 µm continuum. For the gas to create a substantial contribution that would be noticeably more extended than the radius of the central star, it has to be relatively dense, orders of magnitude more dense than the best solutions obtained by only fitting the spectral line profile. Such gas must be optically thick in the visible wavelengths, making the Hα line much less prominent, as the emission is coming from only the surface atmosphere of the gas and not the bulk volume.

Nevertheless, focusing for now only on the spectra, there are two ways of matching the observed profiles, introducing more "slow" emission: increasing the opening angle of the jets, or introducing an extended disk.

Jet-only solutions that minimize the χ^2_{SPE} of the VLT/X-shooter spectrum are shown in Figures 3.26, 3.25. They have converged on an opening angle of about $\alpha_{\mathrm{jt}} \approx (38 \pm 2)^\circ$, and they match the high-velocity (very red-shifted or very blue-shifted) emission well, and can even account for the relative intensity difference between the red-shifted and blue-shifted maximum. They do not however match the emission at low radial velocities.

Jet-only solutions that minimize the χ^2_{SPE} of the VLT/UVES spectra (and the averaged spectrum, as described in the previous chapter), that do not exhibit the double-peaked profile, converge to opening angles of $\alpha_{\mathrm{jt}} \gtrsim 89^\circ$. As these two "jets" now form an almost full spherical shell, I have decided to utilize the `Shellspec` object `shell` that is fully spherically symmetric, removing the need for the α_{jt} parameter that naturally disappeared.

3.2.4 A spherical shell model

The velocity, density and temperature profiles in the `SHELL` object are identical to the `JET` object, except for the geometry:

$$v(r) = v_0 \left(1 - \frac{r_{\mathrm{csh}}}{r}\right)^{e_{\mathrm{denssh}}} , \tag{3.25}$$

$$N_e(r) \propto \rho(r) = \varrho_{\mathrm{sh}} \left(\frac{r_{\mathrm{insh}}}{r}\right)^2 \frac{v(r_{\mathrm{insh}})}{v(r)} , \tag{3.26}$$

$$T(r) = T_{\mathrm{sh}} = \mathrm{const} . \tag{3.27}$$

Working with optically thin matter, which is necessary to explain the observed Hα lines, introduces a natural degeneracy. Focusing only on emissivity in the equation of radiative-transfer:

$$\frac{\mathrm{d}I_\nu}{\mathrm{d}x} = \epsilon_\nu ,$$

or in terms of the specific emissivity, and for small optical depths:

$$I_\nu \propto \varrho \varepsilon_\nu \Delta x .$$

For continuum emission, but even for spectral line emission in a limited range of parameters, the emissivity depends monotonically on temperature. So, while observing optically thin matter at a single wavelength there is a degeneracy between the total volume of matter, its density and its temperature – as seen on Figure 3.9.

A search for the best-fit profile was performed on a sub-space of the possible parameter space, that was identified (via trial and error) as being spanned by the most relevant parameters:

1. R_{outsh}, the outer radius,
2. R_{vsh}, the velocity at the inner boundary,
3. e_{velsh}, the exponent of the power-law describing the velocity field of the shell,
4. T_{sh}, the constant temperature,
5. ϱ_{sh}, the density at the inner boundary.

The R_{insh} had to be fixed slightly above the stellar surface (for not to cause a collision with the `STAR` object).

Scans of the parameter space have been performed, and χ^2_{SPE} maps were generated by comparing the model spectral lines to the ones measured by VLT/UVES. These can be seen in Figures 3.9 and 3.10.

However, the best-fit parameters of the `SHELL` could not be easily transferred to the final model, as the introduction of the disk necessary to explain the interferometric observations influences the spectral line profile. The contribution to the SED and a synthetic image of the `SHELL` model can be seen in Figure 3.8.

3.2.5 A disk and jet model

To account for the continuum emission seen by VLTI/GRAVITY and to compensate for the missing Hα emission at low radial velocities, it is possible to introduce a disk perpendicular to the jets feeding the star. This allows for good fits of both the interferometric observables and the spectral line profiles.

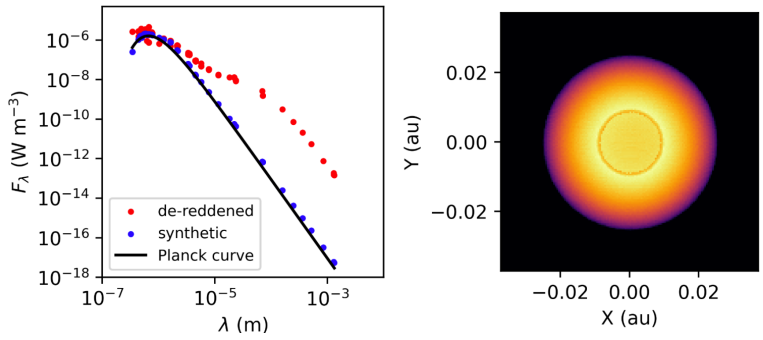

Figure 3.8: **Left**: SED contribution of the star and shell `Pyshellspec` model. The red points are SED measurements corrected for interstellar reddening, and the blue points are the result of the radiative-transfer simulation. The ideal black-body spectrum, corresponding to the temperature $T_\star = 4750\,\mathrm{K}$, is overlaid. **Right**: A synthetic image of the star and shell model calculated for the Hα line (arbitrary color scale).

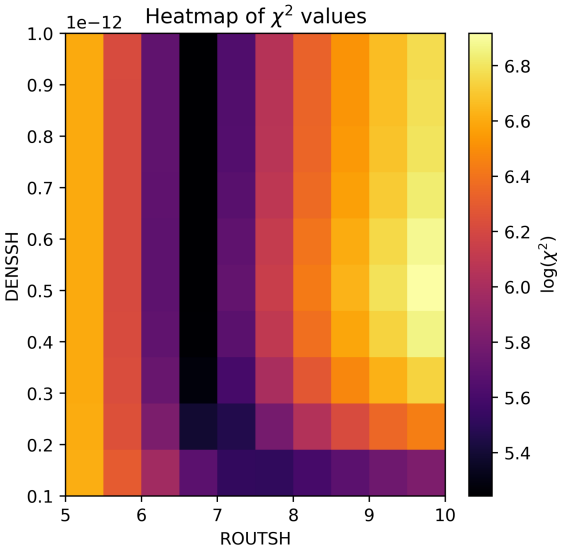

Figure 3.9: The density ϱ_{sh} vs volume χ^2_{SPE} map, based on the VLT/UVES spectra, and a spherically symmetric shell as the source of Hα emission. A degeneracy is visible as a diagonal in the lower portion of the map. The degeneracy of the density ϱ_{sh} and temperature T_{sh}extends in the third perpendicular direction to the valley, where the lowest values of χ^2 values are obtained at $R_{\mathrm{outsh}} = 6.75\,R_\odot$. The map was generated for the velocity $v_{\mathrm{sh}} = 95\,\mathrm{km\,s^{-1}}$ a velocity exponent $e_{\mathrm{velsh}} = 2.42$ and temperature $T_{\mathrm{sh}} = 10000\,\mathrm{K}$.

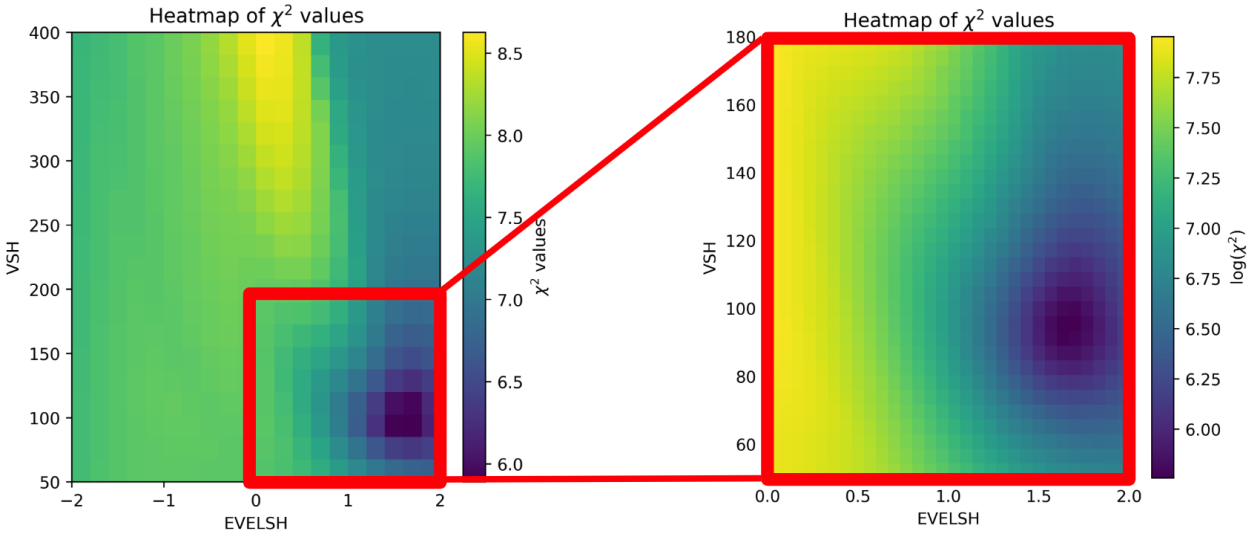

Figure 3.10: An example of a velocity v_{sh} vs the velocity exponent e_{velsh} χ^2_{SPE} map, based on the VLT/UVES spectra, and a spherically symmetric shell as the source of Hα emission.

This however introduces a new complication: the introduction of the continuum emission in the near-IR wavelengths naturally introduces continuum emission to the red part of the visible spectrum, i.e., the continuum around Hα. This of course affects the relative intensity of the Hα line, which is the measured quantity by VLT/X-shooter and UVES.

Converging towards a minimum in the combined metric:

$$\chi^2 = \chi^2_{\rm SPE} + \chi^2_{\rm V2} + \chi^2_{\rm arg(T3)} + \chi^2_{\rm T3}$$

using the averaged spectrum resulted again in very large opening angles of the jets. $\alpha_{\rm jt} > 70°$, leading us towards a model with a spherically symmetric shell. For the best-fit model, whose parameters are shown in Table 3.4, the contributions are:

$$\begin{aligned}
\chi^2_{\rm SPE} &= 749\,, & \chi^2_{r,\rm SPE} &= 3.7\,,\\
\chi^2_{\rm V2} &= 924\,, & \chi^2_{r,\rm V2} &= 1.8\,,\\
\chi^2_{\rm arg(T3)} &= 7.6\cdot 10^4\,, & \chi^2_{r,\rm arg(T3)} &= 1.9\,,\\
\chi^2_{\rm T3} &= 2.9\cdot 10^5\,, & \chi^2_{r,\rm T3} &= 7.1\,.
\end{aligned}$$

From the value of $\chi^2_{r,\rm SPE} = 3.7$, it is clear that the spectroscopic observations capture some complexity that is not present in our model. The value $\chi^2_{r,\rm V2} = 1.8$ differs so significantly from $\chi^2_{r,\rm T3} = 7.1$, even though they correspond to very similar observables, is explained by the fact I have averaged the visibility data in smaller bins (as explained in Chapter 2), but the triple product measurements have not been averaged.

Table 3.4: Best-fit parameters of the jet and disk model of the inner accretion region of DoAr 44.

Parameter	Object	best-fit value	σ	Unit
$\alpha_{\rm jt}$	JET	70	3	$^\circ$
$r_{\rm injt}$	JET	3	0.1	$R_\odot$
$r_{\rm outjt}$	JET	50.8	0.5	$R_\odot$
$v_{\rm sh}$	JET	230	5	K
$\varrho_{\rm sh}$	JET	$3.0\cdot 10^{-10}$	$2\cdot 10^{-11}$	g cm^{-3}
$T_{\rm jt}$	JET	8500	200	K
$e_{\rm tempjt}$	JET	-0.2	0.1	1
$e_{\rm veljt}$	JET	1.6	0.1	1
$r_{\rm innb1}$	NEBULA	10	5	$R_\odot$
$r_{\rm outnb1}$	NEBULA	40	5	$R_\odot$
$\varrho_{\rm nb1}$	NEBULA	$1\cdot 10^{-8}$	$3\cdot 10^{-9}$	g cm^{-3}
$T_{\rm nb1}$	NEBULA	3800	500	K
$e_{\rm dennb1}$	NEBULA	-0.5	0.1	1
$e_{\rm tmpnb1}$	NEBULA	-0.7	0.1	1

3.2.6 A disk and shell model

Out of the objects currently available in `Shellspec`, the geometry that best replicates the observables is the following: a central star, surrounded by a spherical shell of hot gas, surrounded by a disk. The geometry of the disk was taken from the MCMC fits of the analytic

models, an inclination of $i = 40°$ is assumed, together with the position angle of 147°. The rescaled visibilites were used to converge the models, as it is computationally expensive and practically difficult to include the outer halo (which would diminish the visibilities at low values of $\sqrt{u^2 + v^2}$), and maintaining a high enough resolution of the inner hot region, which is the driver constraint for the grid density. The comparison of the spectroscopic and interferometric VLT+VLTI measurements with our synthetic data is shown in Figure 3.11. The plots of $|T_3|$ and $\arg(T_3)$ are shown as a function of the circumference UV_T of the triangle from which the triple product is calculated (as in reality, the independent variable is four-dimensional):

$$(u_1, v_1)^T = \frac{\mathbf{B_1}}{\lambda}\,, \tag{3.28}$$

$$(u_2, v_2)^T = \frac{\mathbf{B_2}}{\lambda}\,, \tag{3.29}$$

and the third edge of the triangle is:

$$(u_3, v_3)^T = (u_1, v_1)^T + (u_2, v_2)^T\,, \tag{3.30}$$

and the circumference:

$$UV_T = \sqrt{u_1^2 + v_1^2 + u_2^2 + v_2^2 + u_3^2 + v_3^2}\,. \tag{3.31}$$

For the best-fit model, the χ^2 contributions are:

$$\begin{aligned}
\chi^2_{\mathrm{SPE}} &= 605\,, & \chi^2_{r,\mathrm{SPE}} &= 3.0\,,\\
\chi^2_{\mathrm{V2}} &= 759\,, & \chi^2_{r,\mathrm{V2}} &= 1.4\,,\\
\chi^2_{\mathrm{arg(T3)}} &= 7.7 \cdot 10^4\,, & \chi^2_{r,\mathrm{arg(T3)}} &= 1.8\,,\\
\chi^2_{\mathrm{T3}} &= 5.2 \cdot 10^5\,, & \chi^2_{r,\mathrm{T3}} &= 12.0\,.
\end{aligned}$$

This model produces better fits in comparison to the jet and disk model (except for triple products, where there might be some scaling issue) – cf. Figures 3.25 and 3.26.

The problem with the triple product is most likely related to the fact, that the rescaling was done using the parameter e obtained by the MCMC analytic modeling, which quantifies the contribution of a halo to the visibility measurements. The parameter e was fitted using the squared visibilies (where it appears in the models as e^2), and applied as a correction to the triple products as a factor of $1/e^3$. However, I should have fitted both the visibility and the triple product data at the same time.

If I assume the radial velocity is negative, I derive the accretion rate of:

$$\dot{M} = (6.6 \pm 0.2) \cdot 10^{-9}\, M_\odot\, \mathrm{yr}^{-1}\,, \tag{3.32}$$

which is surprisingly similar to result obtained by Bouvier et al. (2020a).

3.3 `Pyshellspec` radiative-transfer models of the outer disk

From the MCMC modeling by a δ-ring performed at in Section 3.1, I have a general idea of the extent of the outer disk. Stated more carefully, a δ-ring of radius $R = (48 \pm 0.2)$ au is the

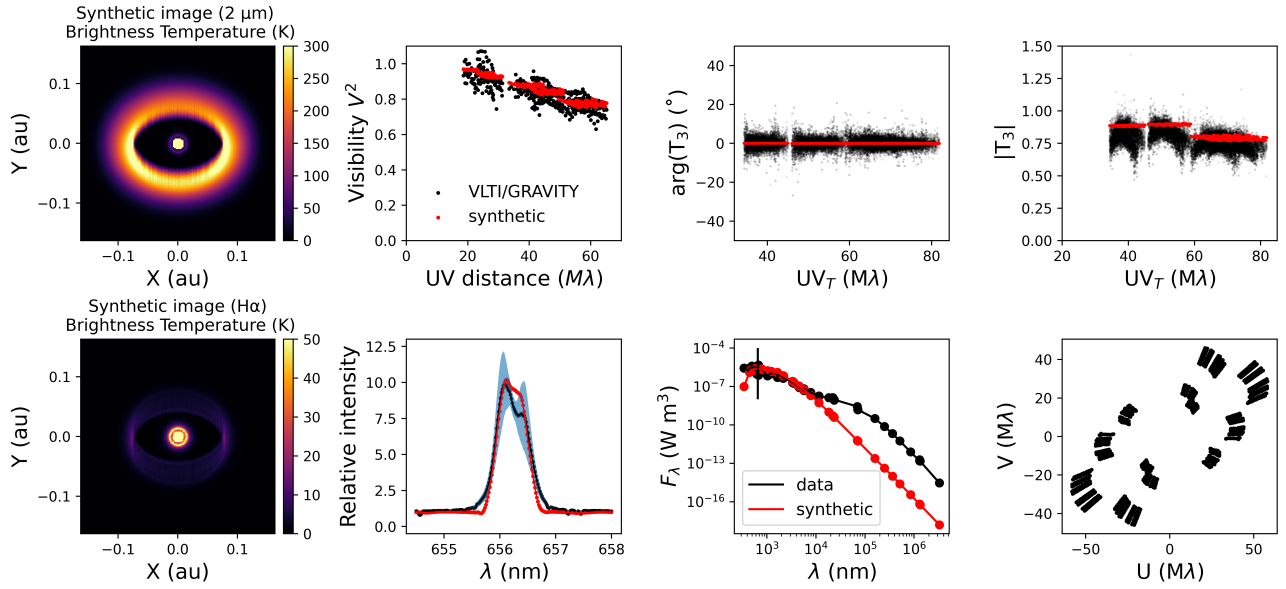

(a) Positive shell radial velocity

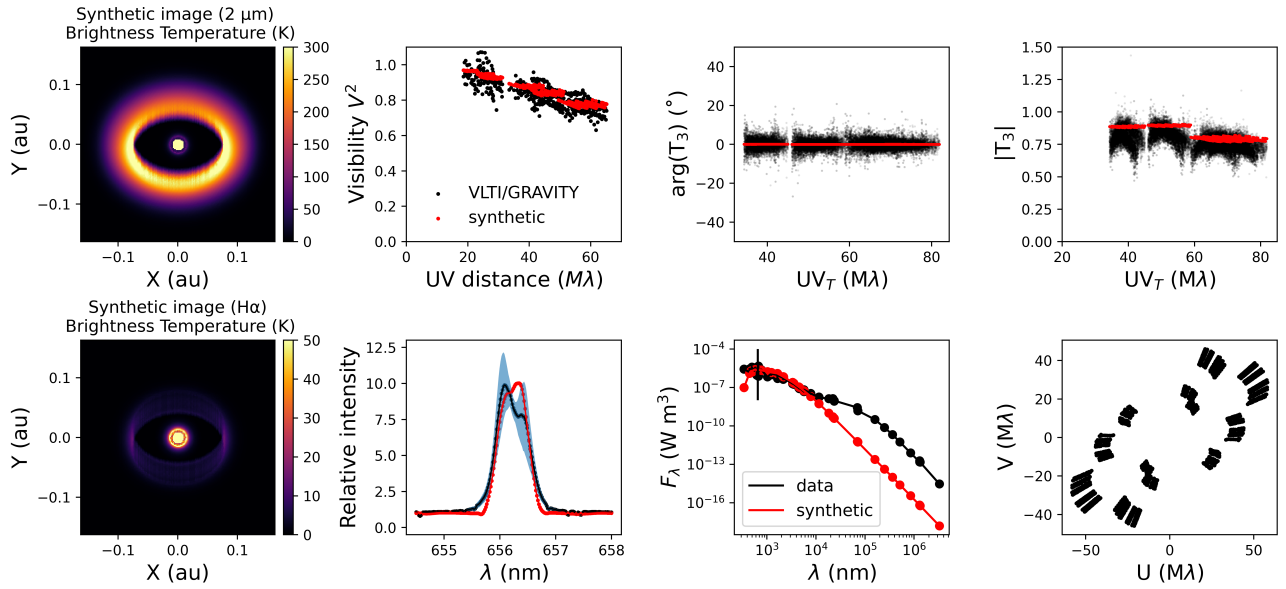

(b) Negative shell radial velocity

Figure 3.11: The best-fit models of the inner accretion region and the inner rim. The two synthetic images (top left, bottom left) are calculated for the K band (2 microns), which is what is observed with the VLTI/GRAVITY. The bottom synthetic image is calculated near the Hα line in the surrounding continuum. The squared visibilities, closure phases and triple products are shown, together with the UV coverage of the Fourier plane. The spherical geometry of the shell was chosen to fit the "mean" calm spectral line. In the SED, a contribution of the outer disk is clearly missing. The top panel is a model with positive radial velocities in the shell, and negative radial velocities were assumed for the model shown on the bottom panel. The position angle of 147° is used for the calculation of the synthetic visibilities.

Table 3.5: Best-fit parameters of the shell and disk model. The stellar parameters are also included. This model of the inner region was also used for the global model. In Table 3.7 you can find estimates of uncertainties of these parameters.

Parameter	Object	best-fit model	Unit
$R_\star$	STAR	2	$R_\odot$
$T_\star$	STAR	4750	K
$M_\star$	STAR	1.4	$M_\odot$
r_{insh}	SHELL	3	$R_\odot$
r_{outsh}	SHELL	9	$R_\odot$
v_{sh}	SHELL	± 330	K
ϱ_{sh}	SHELL	$2.8 \cdot 10^{-13}$	$\mathrm{g\,cm^{-3}}$
T_{sh}	SHELL	10000	$\mathrm{km\,s^{-1}}$
e_{velsh}	SHELL	1.3	1
r_{innb1}	SHELL	16.5	$R_\odot$
r_{outnb1}	NEBULA	35	$R_\odot$
ϱ_{nb1}	NEBULA	$1 \cdot 10^{-8}$	$\mathrm{g\,cm^{-3}}$
T_{nb1}	NEBULA	2500	K
e_{dennb1}	NEBULA	-0.5	1
e_{tmpnb1}	NEBULA	-0.7	1
a_{nb1}	NEBULA	1.5	1

best-fit of all possible δ-rings, and seems to approximate the observed visibilities qualitatively well, as seen in Figure 3.5. The ALMA pipeline, however, claims a 1.2% relative uncertainty on the visibilites, and the deviation of the δ-ring model from the data is about 11%. This means that the structure must be more complex.

As described in Section 2.4, a completely uninformative model can be constructed using a large but finite number of point sources (δ-distributions). Theoretically, the Fourier transform of a function holds the complete description of the function, as $f = \mathcal{F}^{-1}\{\mathcal{F}\{f\}\}$, except for a set of measure zero for all $f \in L^1(\mathbb{R}^N)$, which is a reasonable function space to describe finite sources. However, in practice, we are never in this situation, as we do not have access to the whole Fourier transform of the source, but only to a sample of it.

Disturbingly, this sample is of measure zero and there are infinitely many sources that differ only in the *unsampled* portions of the Fourier space. Notably, the $u = v = 0$ component is missing, which is the component encoding the total flux of the source, as:

$$\mu(0,0) = \int_{\mathbb{R}^2} I(l,m) e^{2\pi i(0l+0m)} \mathrm{d}l\,\mathrm{d}m = \int_{\mathbb{R}^2} I(l,m) \mathrm{d}l\,\mathrm{d}m\,, \tag{3.33}$$

which is the reason the Total Power Array is often employed for extended sources (otherwise the flux calibration should suffice).

Notwithstanding, the CLEAN algorithm for the creation of synthetic images in its various forms is used for essentially all ALMA observations — and ALMA is the most densely sampled of all radio arrays. These images of DoAr 44 are shown in Figure 2.6. Notably, on panels G and H the unusual ring-within-a-ring morphology is apparent. The best-fit $\delta-$ring is located on a slightly larger radius than the bright ring in the CLEAN images, as more flux is coming from outside of this radius than within in it.

3.3.1 A monotonic density profiles

It is possible to imagine that the cavity and ring morphology is a result of some observational effect, e.g., some opacity transition given by a favorable coincidence of temperature, particle size and also wavelength.

I have tried modeling a variety of monotonic density profiles, as this would be an elegant explanation for the morphology, without the need to introduce additional entities to the model — by this I mean that a *real* cavity requires additional conditions to exist, e.g., a pile-up of dust, a pressure trap, or an exoplanet "sheparding" the ring.

A monotonic density profile (like the MMSN (Hayashi, 1981) or others) should be a natural, *a priori* assumption: the cloud collapse preceding the existence of the disk occurs from the inside out, as the matter accretes onto the star.

Two extreme situations are shown in Figure 3.12. While trying to account for the SED in the 1–2 µm band, where the contribution of the star and accretion region is beginning to diminish, the SED in the 7–10 µm region is overestimated, and is underestimated in the mm and sub-mm domain. Likewise, if the far-IR and sub-mm flux is well estimated, then the monotonic model has an SED deficit (with respect to the data) in the 1–2 µm range. **A monotonic profile is thus in contradiction with the observations**.

Moreover, the synthetic images at 225 and 345 GHz (Band 6 and 7) do not show the ring-like morphology. Consequently, the synthetic visibilities are a monotonic function of $\sqrt{u^2 + v^2}$ and do not show the maxima and minima present in the data, regardless of particle size. A drawback of our tools is the fact that a single particle size or size distribution has to be chosen for the entire model, so e.g., a dependence of particle size on the distance from the central star cannot be modeled. Such studies have been performed, utilizing spatially resolved spectral index maps, e.g., Arce-Tord et al. (2023).

We can conclude that the disk does not have a monotonic dust density profile with a radially independent particle size distribution.

3.3.2 A large cavity

As we cannot proceed any further with the monotonic profiles, we were forced to introduce a cavity, mirroring the structure seen in the CLEAN ALMA images. A scan over a variety of parameters (particle size, density, inner radius, outer radius) evaluating the $\chi^2_{\mathrm{V2}} + \chi^2_{\mathrm{SED}}$ contribution was performed, see Figures 3.13, 3.14 and 3.17. The constraint on the total area of the disk is given primarily from the CLEANed ALMA images, where the inner and outer boundaries are visible (up to the background RMS level, the dust extends up to ≈ 80 au, see Figure 2.6). At the moment, `Shellspec` does not offer a more complex density profile. The ring-within-a-ring morphology was for the first time seen in 2021, and only for DoAr 44, WSB 82 and SR24S (Cieza et al., 2021), so it is quite a niche requirement. This however means that a certain compromise has to be taken to fit the interferometry, as most of the emission is coming from a narrow annulus, but a portion of the emission comes from a wide annulus. The best-fit parameters for the outer disk are shown in Table 3.6. The parameter ϱ_{dstnb} describes the dust density in the protoplanetary disk. In my simulations, this parameter was fixed to the gas density ϱ_{nb} via a constant metallicity,

$$\varrho_{\mathrm{dstnb}} = Z\,\varrho_{\mathrm{nb}}\,, \tag{3.34}$$

which was chosen as $Z = 0.0123$ which is the solar metallicity.

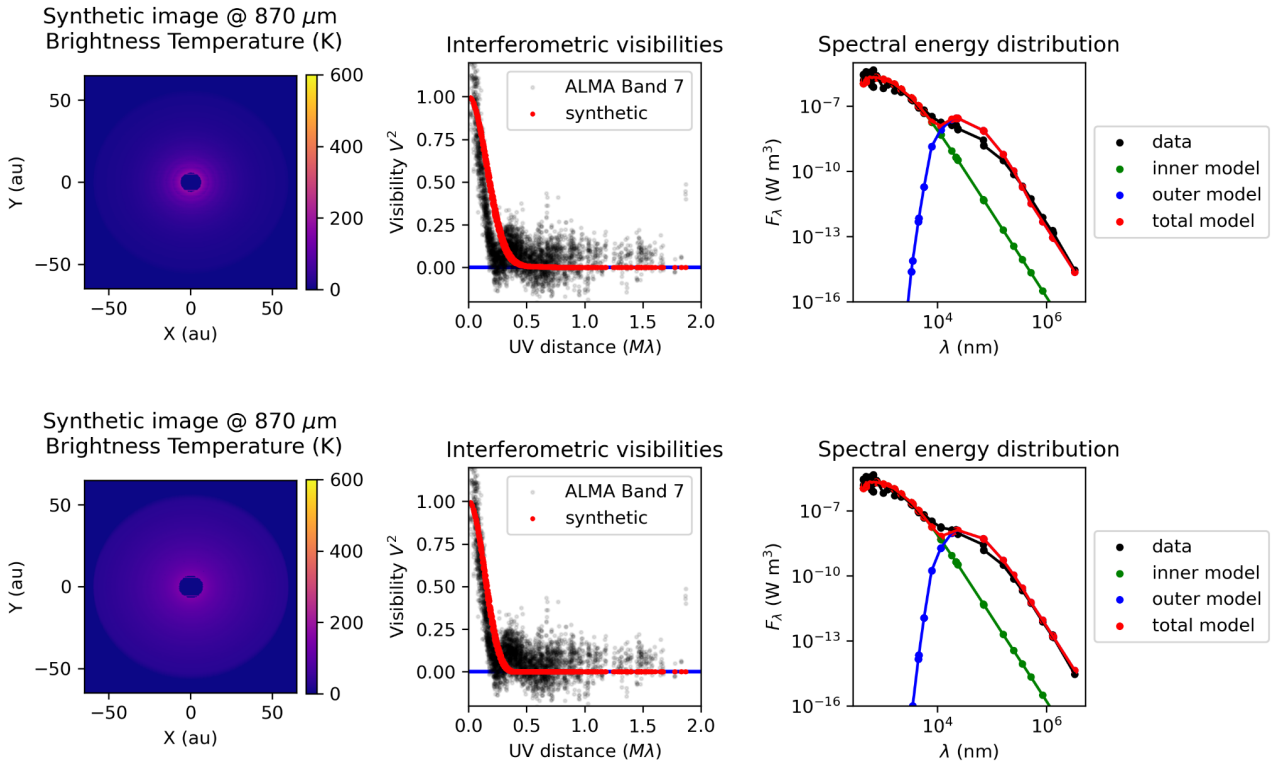

Figure 3.12: The best-fit models of DoAr 44 with monotonic density profiles. The top model tries to account for the mid-IR photometric measurements, while the bottom model tries to fit the far-IR, sub-mm and mm measurements. Both models assume a uniform particle size across the whole disk, as our tool does not allow a closer specification of a grain size distribution vs distance. Both models are clearly in a contradiction with the ALMA visibilities or the SED.

From the SED, the best-fit models are achieved by reaching densities so high that the outer disk to becomes optically thick — see Figures 3.13 and 3.17. For dust containing only large particles (100 µm), we did not obtain any good fits. The issues with this result are discussed in Chapter 4.

Table 3.6: The best-fit model of the outer disk, for small dust particles ($a < 1\,\mu\text{m}$). The size distribution of the dust was uniform, and did not affect the best-fit values significantly until it reached 100 µm.

Parameter	Object	best-fit value	σ	Unit
r_{innb}	NEBULA	36	1	au
r_{outnb}	NEBULA	56	1	au
T_{nb}	NEBULA	60	3	K
ϱ_{dstnb}	NEBULA	$> 1 \cdot 10^{-14}$	$> 3 \cdot 10^{-15}$	g cm^{-3}
e_{densnb}	NEBULA	-0.5	0.1	1
e_{tempnb}	NEBULA	-0.5	0.1	1

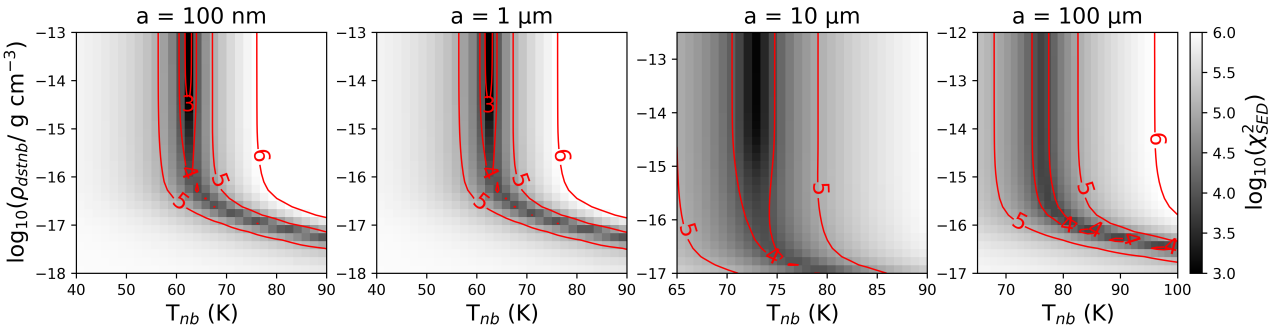

Figure 3.13: The χ^2_{SED} contribution of the outer disk, for a variety of different particle sizes, from 100 nm to 100 µm. The curved low-density high-temperature sections correspond to optically thin solutions, and the vertical (isothermal) dark areas correspond to optically thick solutions.

3.4 The global model and constrains on the inner disk

In the sections above, I have constructed and described models of structures, of which we have spatially resolved interferometric observations, constraining their angular extent. However, including all the modeled structures (the star, the shell, the innermost disk, and the outer disk) into a single radiative-transfer simulation is challenging, for several reasons.

Firstly, the inner accretion region simulations revealed that for the synthetic spectral line profiles to converge, it is necessary to use cells of at most $0.5 \cdot 0.5 \cdot 0.5\,R^3_\odot$. If the whole disk was sampled with this cell size, the grid would have about 30 000 cells in each direction ($3 \cdot 10^{13}$ cells in total). This is simply too much.

In principle, a logarithmic grid could be used, but this presents a whole new set of challenges. These are related to the geometry of projection onto an inclined aperture plane, which would also have to be unequally spaced. Due to the inclined geometry, a single ray in the simulation would intersect differently sized cells. Later, to produce synthetic interferometric observables, discrete Fourier transforms with unequal cell sizes, which are computationally expensive, would

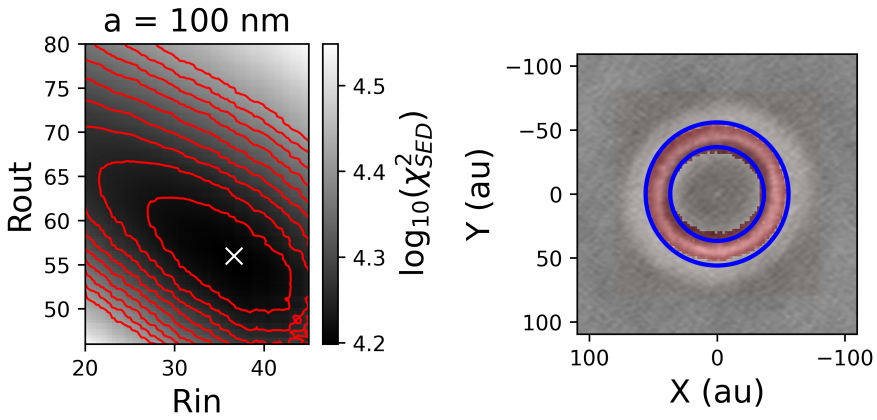

Figure 3.14: The χ^2_{V2} contribution of the outer disk, for the density $\varrho_{\mathrm{densnb}} = 3 \cdot 10^{-14}\,\mathrm{g/cm^3}$, and the temperature of $T_{\mathrm{nb}} = 62.3\,\mathrm{K}$.

have to be performed tens of thousands of times, to calculate the χ^2 contribution. To converge the parameters of the model would be extremely challenging.

Secondly, DoAr 44 has a warped geometry, with the inner region being more inclined than the outer region. At the moment, we have no way to achieve this complex geometry with `Shellspec`.

To overcome these challenges, the following approach was taken while constructing the global model. Observables which could be uniquely attributed to a single component of the model were converged separately.

In particular, the Hα contribution was calculated only from the star, shell and innermost disk, but not from the outer disk. This is well justified, as the temperatures in the outer disk are strictly below 100 K, a temperature much too low to excite the Hα transition. Absorption of Hα from the outer disk was not considered, as it is not geometrically in the path of light from the star towards the observed.

On the other hand, in several simulations, the central star (rescaled to sub-cell sizes, as shown in Figure 3.20) was included, to gauge the contribution of scattering of stellar sub-mm radiation from the disk – these can be seen in Figure 3.28.

Four global models have been constructed. Firstly, a model with a monotonic density profile, constructed in Section 3.3.1, is presented in the third column of Table 3.7 as a reference.

The inner region was described by the shell and disk model. That is because a rotating disk cannot explain the emission line profile (see Figures 3.22, 3.23). Jet models of the inner regions seemed like a good way to explain the spectral line emission, see Figures 3.25 and 3.25. However, after including an innermost disk, necessary to explain the VLTI/GRAVITY visibilities, these jet models started to converge to very large opening angles. To reduce the dimensionality of the space, I have decided to use a shell model as a source of the Hα emission.

Then, three different models with a large cavity are presented. To account for the mid-IR deficit, an inner disk has been included, modeled by a `DISK` object in `Pyshellspec`. These models (A, B, C) have identical parameters of the innermost region and the outer disk, but differ only in the parameters of the `DISK` object, which is a thin rotationally symmetric wedge (space complement to two opposite cones) with an opening angle α_{dc}. The temperature in the `DISK` is described by a power-law with the exponent e_{tmpdc}:

$$T(R) = T_{\mathrm{dc}} \left(\frac{R}{R_{\mathrm{indc}}} \right)^{e_{\mathrm{tmpdc}}} , \tag{3.35}$$

where $T_{\rm dc}$ is the temperature at the inner edge of the disk, which has a radius $R_{\rm indc}$. The density in the disk is also described by a power-law:

$$\varrho(R) = \varrho_{\rm dc} \left(\frac{R}{R_{\rm indc}} \right)^{e_{\rm densdc}} , \tag{3.36}$$

where I assumed $e_{\rm densdc} = -1.5$ to be fixed. Model **A** describes a very extended inner disk, spanning from 0.5 au to 5 au. It has the steepest temperature power-law exponent of the three models. Models **B** extends from 3 au to 5 au and model **C** extends from 5.2 au to 7 au. These parameters produce virtually identical contributions to the SED.

The parameters of the global model are presented in Table 3.7, and the density and temperature profile of Model A is shown in Figure 3.19. Integrated total surface densities of the innermost, inner and outer disks are shown in Figure 3.18

The three different models of the inner disk, where the most interesting events of planet formation are occurring, are currently impossible to distinguish, and more observations are needed. For this reason, I have submitted an ALMA proposal (see details in Appendix A) and I am also suggesting observations with VLTI/MATISSE (Chapter 4).

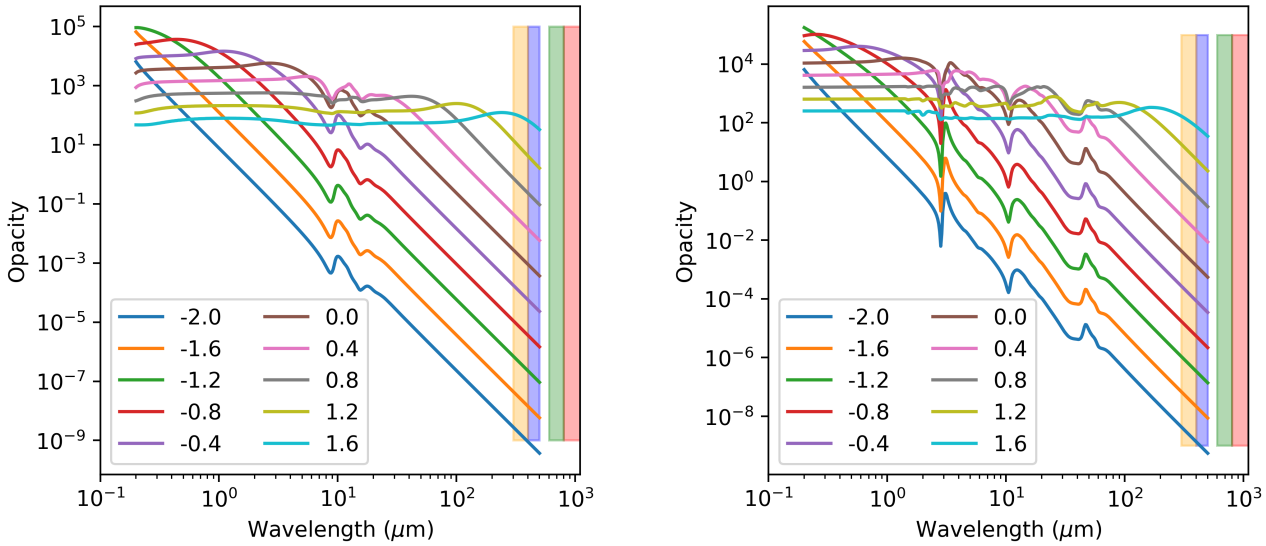

Figure 3.15: **Scattering** opacity of forsterite grains and water ice grains of given size, in cm^2/g. The different curves denote different particle sizes, denoted by $\log_{10}(a/\mu\mathrm{m})$. The shaded areas on the right sides of each graph denote ALMA Bands 7, 8, 9 and 10. The flat part of the curve for short wavelengths corresponds to the Mie scattering regime, and the steep diagonal part of the curve corresponds to the Rayleigh scattering regime. The feature around 10 µm on the **left** plot (forsterite) is caused by the vibration of Si–O bonds in a crystalline lattice. Similarly, the sharp features on the **right** graph are caused by vibrations of the water ice lattice. Data from the Budaj et al. (2015) dust tables.

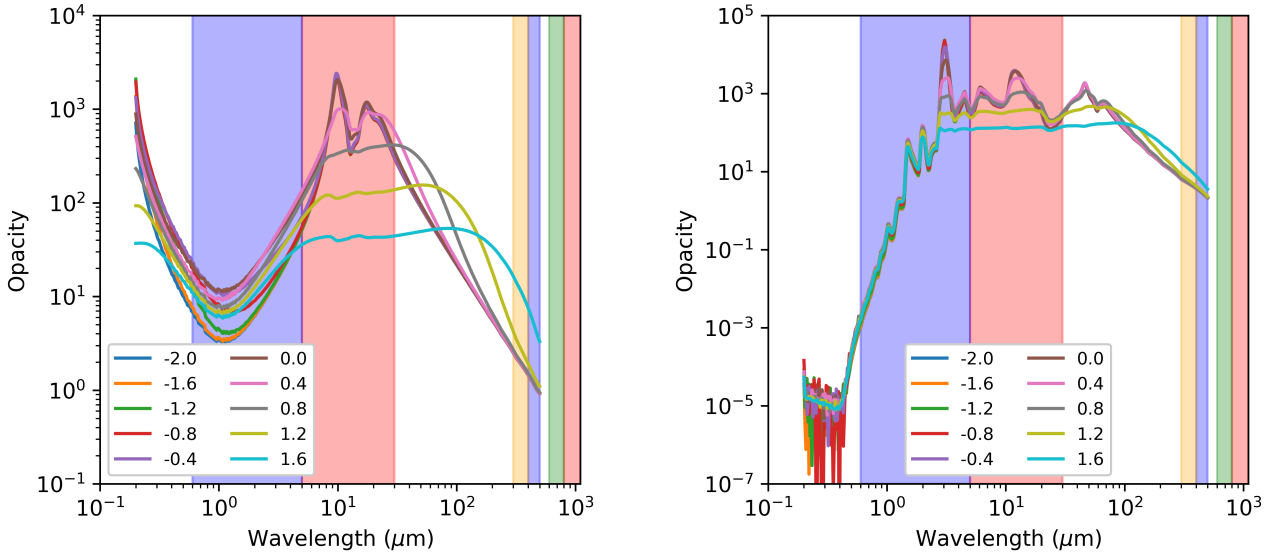

Figure 3.16: **Absorption** opacity of forsterite grains (**left**) and water ice grains (**right**) of given size, in cm^2/g. Shaded areas on the right sides of each graph again denote ALMA Bands 7, 8, 9 and 10. The wider blue and red bands correspond to the wavelength range of JWST/NIRSpec and JWST/MIRI instruments, respectively. The red area also coincides with the range of Spitzer/IRS. Data from the Budaj et al. (2015) dust tables.

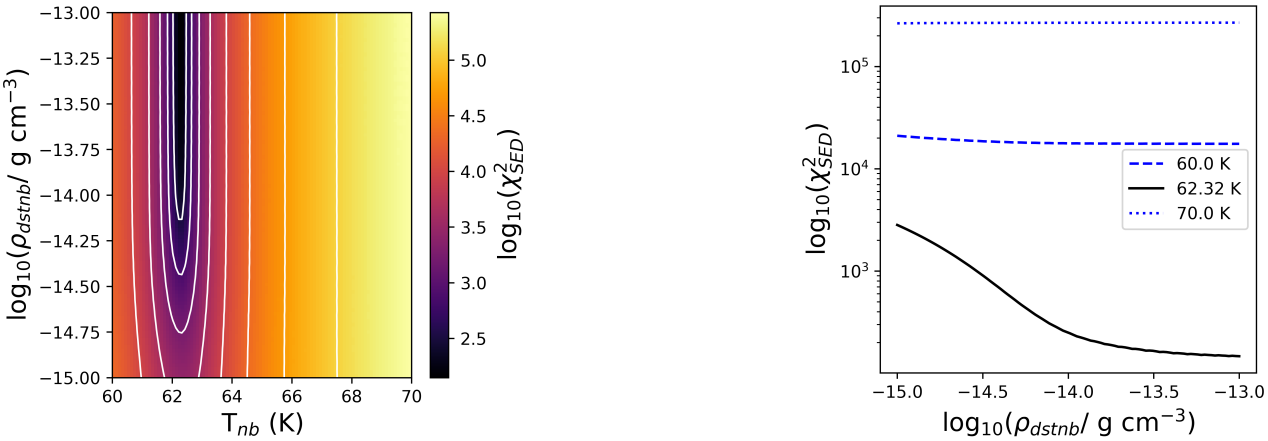

Figure 3.17: The $\chi^2_{\rm SED}$ contribution of the outer disk, modelled with dust of size $a = 10\,\mathrm{nm}$ as an extremely small value. The SED was cropped to $\lambda > 70\,\mu\mathrm{m}$, to minimize the contribution of the a priori unconstrained inner disk (1–10 au). The geometry is constrained by ALMA interferometry, with $R_{\rm innb} = 37\,\mathrm{au}$ and $R_{\rm outnb} = 56\,\mathrm{au}$. The density profile was chosen as $e_{\rm densnb} = -0.5$, which is quite shallow (the MMSN (Hayashi, 1981) exponent is -1.5). This is to give more weight to the inner rim, to accommodate for the ring-within-a-ring geometry. The temperature is well constrained at $T = 62.3\,\mathrm{K}$ for **fixed** values of the inner and outer radius. Different inner and outer radii (in a reasonable range compatible with the ALMA measurements) result in similar temperatures in the 50–70 K range.

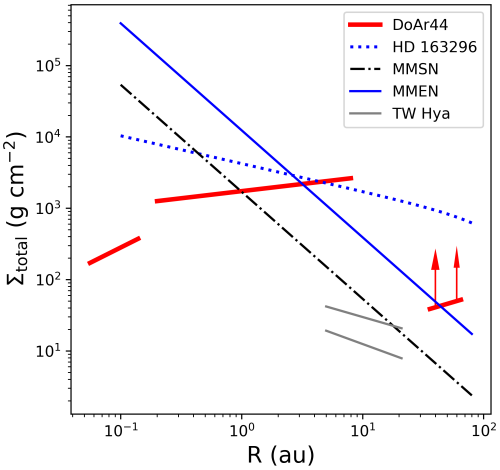

Figure 3.18: The integrated surface total (gas + dust) density of our model (red) compared to a series of other surface densities. In the outer disk, a lower bound on the density is presented. Williams and McPartland (2016) derived the surface density of the disk HD163296 from ALMA measurements using the Lynden-Bell and Pringle (1974) prescription. MMSN is the traditional description by Hayashi (1981), $\Sigma = 1700\,\mathrm{g/cm^2}\left(\frac{r}{1\,\mathrm{au}}\right)^{-1.5}$. MMEN denotes one of the Minimum Mass Extrasolar nebulae (Chiang and Laughlin, 2013), derived from exoplanetary statistics. The TW Hya surface densities were derived by Zhang et al. (2017) from ALMA Band 7 CO-line measurements.

Table 3.7: Best-fit global models of DoAr 44. * The parameters $v_{\rm sh}$ and $e_{\rm velsh}$ are inevitably correlated. ** The estimated errors for the density $\varrho_{\rm nb2}$ in the monotonic profile model is of the order of $2 \cdot 10^{-8}\,{\rm g\,cm^{-3}}$, whereas for the cavity models (A, B, C) I provide only a lower limit of the density.

Parameter	Object	best monotonic	Model A	Model B	Model C	σ	Unit
$r_\star$	STAR	2	2	2	2	0.2	$R_\odot$
$T_\star$	STAR	4750	4750	4750	4750	150	K
$M_\star$	STAR	1.4	1.4	1.4	1.4	0.2	$M_\odot$
$r_{\rm insh}$	SHELL	3	3	3	3	0.1	$R_\odot$
$r_{\rm outsh}$	SHELL	10	10	10	10	1	$R_\odot$
$v_{\rm sh}$ *	SHELL	330	330	330	330	5	K
$\varrho_{\rm sh}$	SHELL	$2.8 \cdot 10^{-13}$	$2.8 \cdot 10^{-13}$	$2.8 \cdot 10^{-13}$	$2.8 \cdot 10^{-13}$	$5 \cdot 10^{-14}$	${\rm g\,cm^{-3}}$
$T_{\rm sh}$	SHELL	10000	10000	10000	10000	1000	K
$e_{\rm velsh}$ *	SHELL	1.5	1.5	1.5	1.5	0.1	1
$R_{\rm innb1}$	NEBULA	12	16.5	16.5	16.5	3	$R_\odot$
$R_{\rm outnb1}$	NEBULA	35	35	35	35	5	$R_\odot$
$\varrho_{\rm nb1}$	NEBULA	$1.0 \cdot 10^{-8}$	$1.0 \cdot 10^{-8}$	$1.0 \cdot 10^{-8}$	$1.0 \cdot 10^{-8}$	$3 \cdot 10^{-9}$	${\rm g\,cm^{-3}}$
$T_{\rm nb1}$	NEBULA	3000	2500	2500	2500	500	K
$e_{\rm dennb1}$	NEBULA	-0.5	-0.5	-0.5	-0.5	0.1	1
$e_{\rm tmpnb1}$	NEBULA	-0.7	-0.7	-0.7	-0.7	0.1	1
$R_{\rm indc}$	DISK	–	108	645	1125	100	$R_\odot$
$R_{\rm outdc}$	DISK	–	1075	1075	1500	100	$R_\odot$
$\varrho_{\rm dc}$	DISK	–	$1 \cdot 10^{-10}$	$1 \cdot 10^{-10}$	$1 \cdot 10^{-10}$	$3 \cdot 10^{-11}$	${\rm g\,cm^{-3}}$
$T_{\rm dc}$	DISK	–	550	260	260	20	K
$e_{\rm tmpdc}$	DISK	–	-0.53	-0.3	-0.3	0.1	${\rm g\,cm^{-3}}$
$\alpha_{\rm dc}$	DISK	–	15	15	15	3	$^\circ$
$R_{\rm innb2}$	NEBULA	108	9000	9000	9000	200	$R_\odot$
$R_{\rm outnb2}$	NEBULA	12900	12900	12900	12900	200	$R_\odot$
$\varrho_{\rm nb2}$	NEBULA	$2.4 \cdot 10^{-7}$	$> 8 \cdot 10^{-13}$	$> 8 \cdot 10^{-13}$	$> 8 \cdot 10^{-13}$	**	${\rm g\,cm^{-3}}$
$T_{\rm nb2}$	NEBULA	600	60	60	60	10	K
$e_{\rm dennb2}$	NEBULA	-1.5	-0.5	-0.5	-0.5	0.1	1
$e_{\rm tmpnb2}$	NEBULA	-0.5	-0.5	-0.5	-0.5	0.1	1

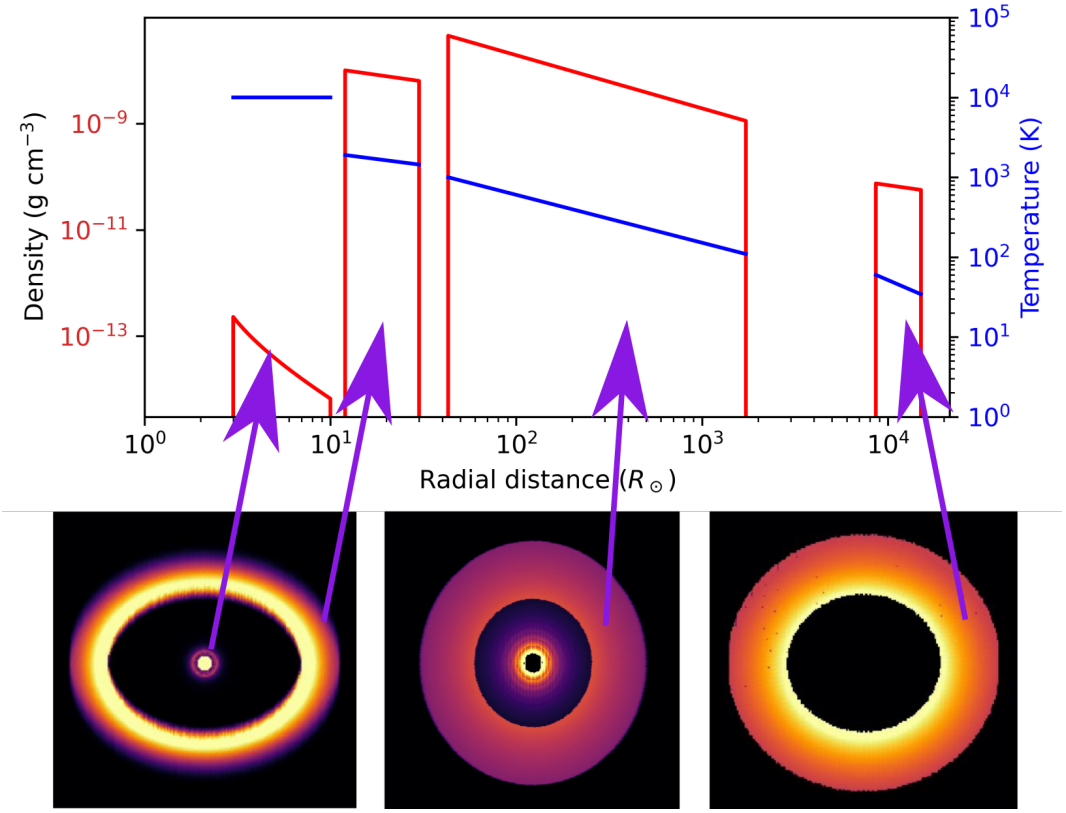

Figure 3.19: **Top**: The temperature and total density profiles in the final global multi-scale model. The center part is described by a star, surrounded by a spherical shell of **optically thin** hot gas, which is responsible for the observed visible spectral lines. Next, an **optically thick** innermost disk follows, of which mostly the inner rim is visible, contributing to the near-IR visibilities. Next, a large, essentially empty gap follows. At still larger radii, an inner disk is present, but not many constrains are placed on its exact extent. Here, Model A from Table 3.7 is shown. At last, a dusty outer disk is included in the model, which is directly observed with ALMA. **Bottom**: synthetic images from the `Pyshellspec` radiative-transfer simulations. The left panel shows the star, an optically thin shell, surrounded by an innermost disk. The shell is not very prominent, as this image was calculated in the 2 micron continuum. The center panel shows the inner disk at 350 micron (ALMA Band 10), with a prominent opacity transition due to the condensation of water ice. The right panel shows the outer disk in the 870 micron continuum (ALMA Band 7).

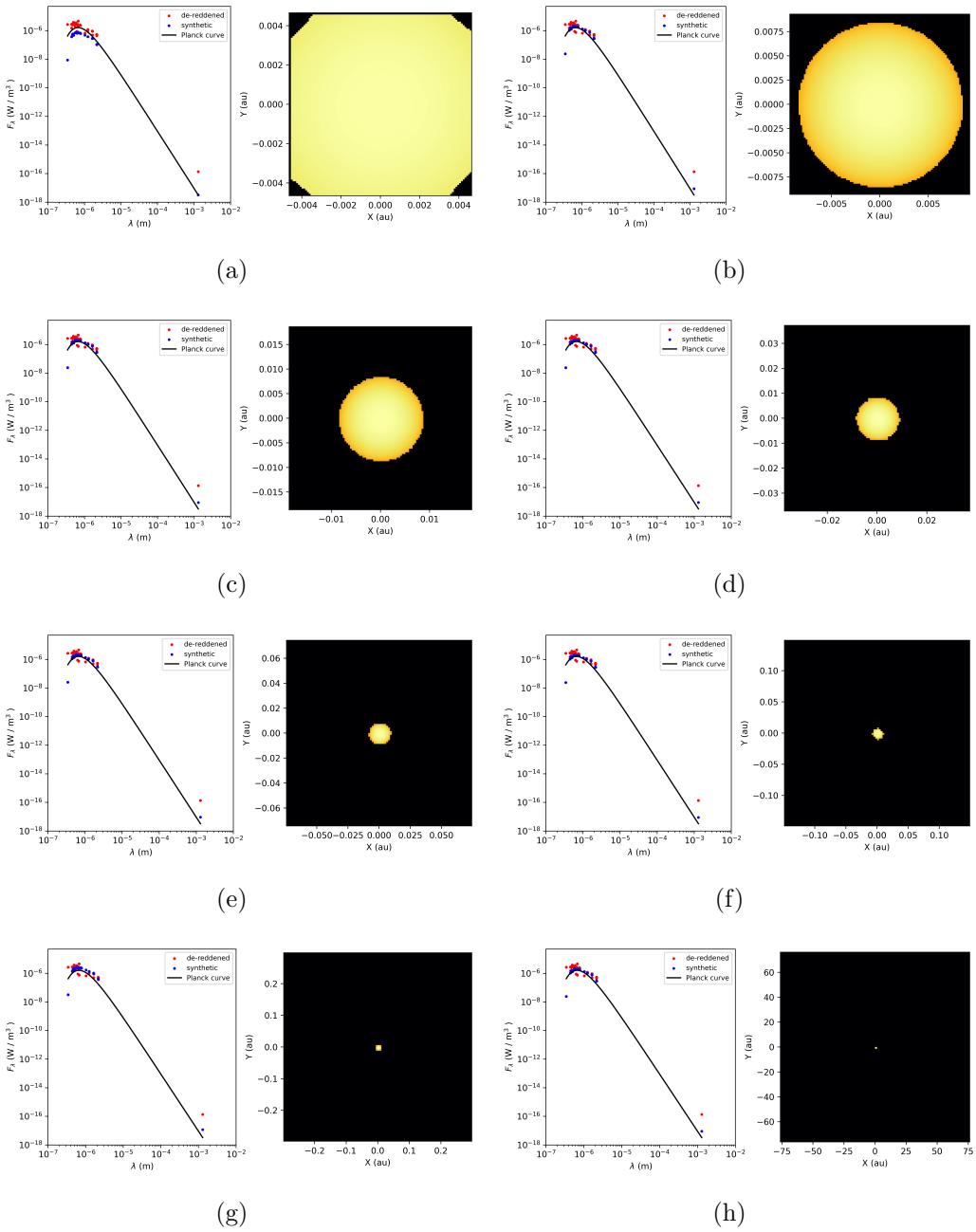

Figure 3.20: Testing synthetic images and SEDs of the central star. It was necessary to access the effect of scattering of the stellar light in the outer disk. Notice, that with the exception of (a), where a part of the stellar emission is missing, the global SEDs look virtually identical, even for the radiative transfer simulations using only several cells. I modified the `Shellspec` code to fractionally scale the contribution of the star, even if its size is orders of magnitude smaller than one pixel. The details, like the wavelength-dependent limb darkening, are sacrificed in the process. The photospheric emission is negligible in comparison to the outer disk in the mm and sub-mm wavelength. For the magnetospheric accretion region calculations, the star was kept as a small but resolved source.

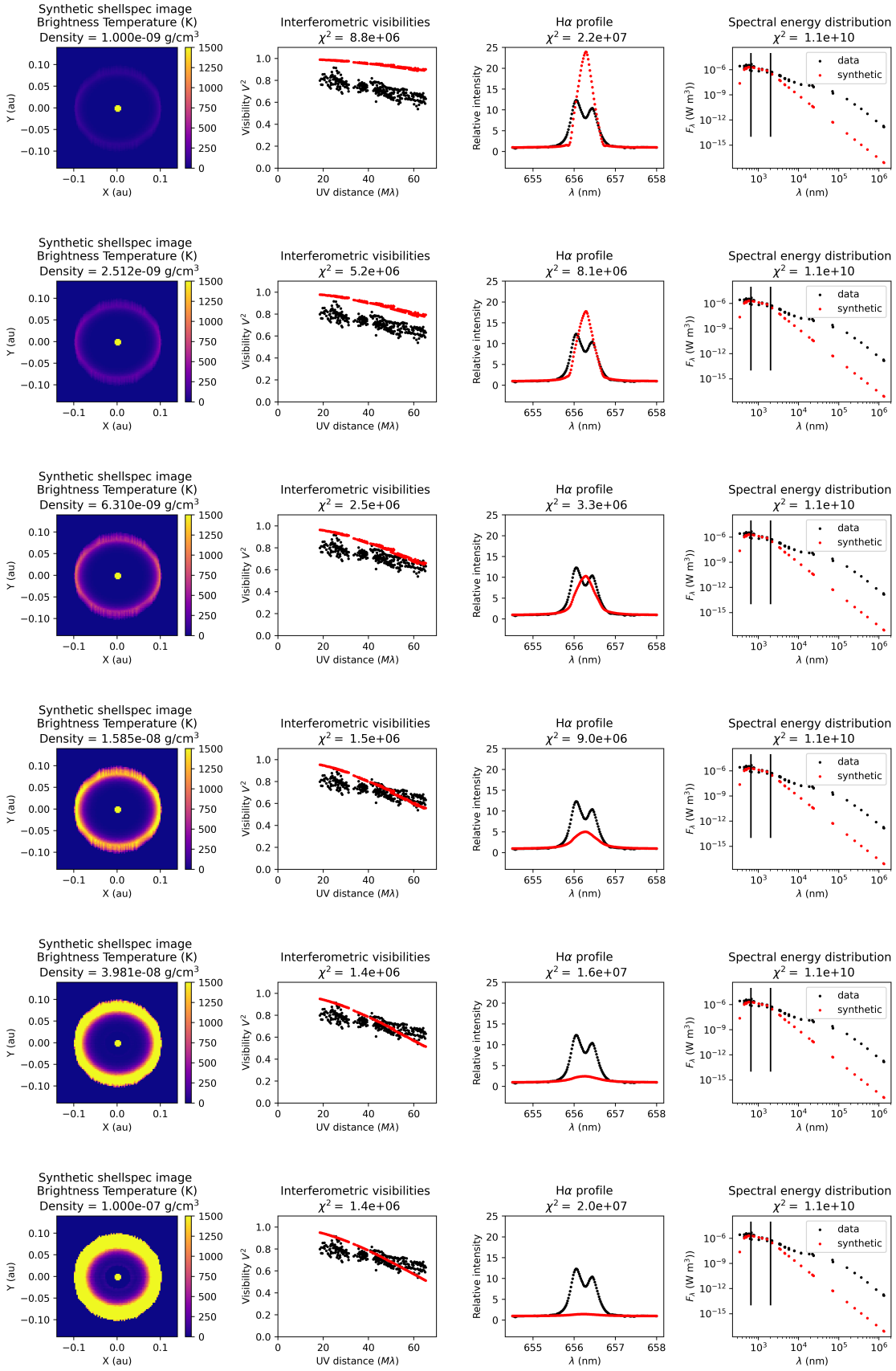

Figure 3.21: Testing a transition of densities, for the innermost disk with an inclination of $i = 23\,\mathrm{deg}$ derived from ALMA measurements compared to observables (interferometry, Hα profile, SED). As the density of the innermost disk increases, so does the continuum optical depth. Low optical depths allow us for an emission from a large volume of the disk. In the optically thick regime, one can only see the line emission from a thin atmosphere above the untransparent disk.

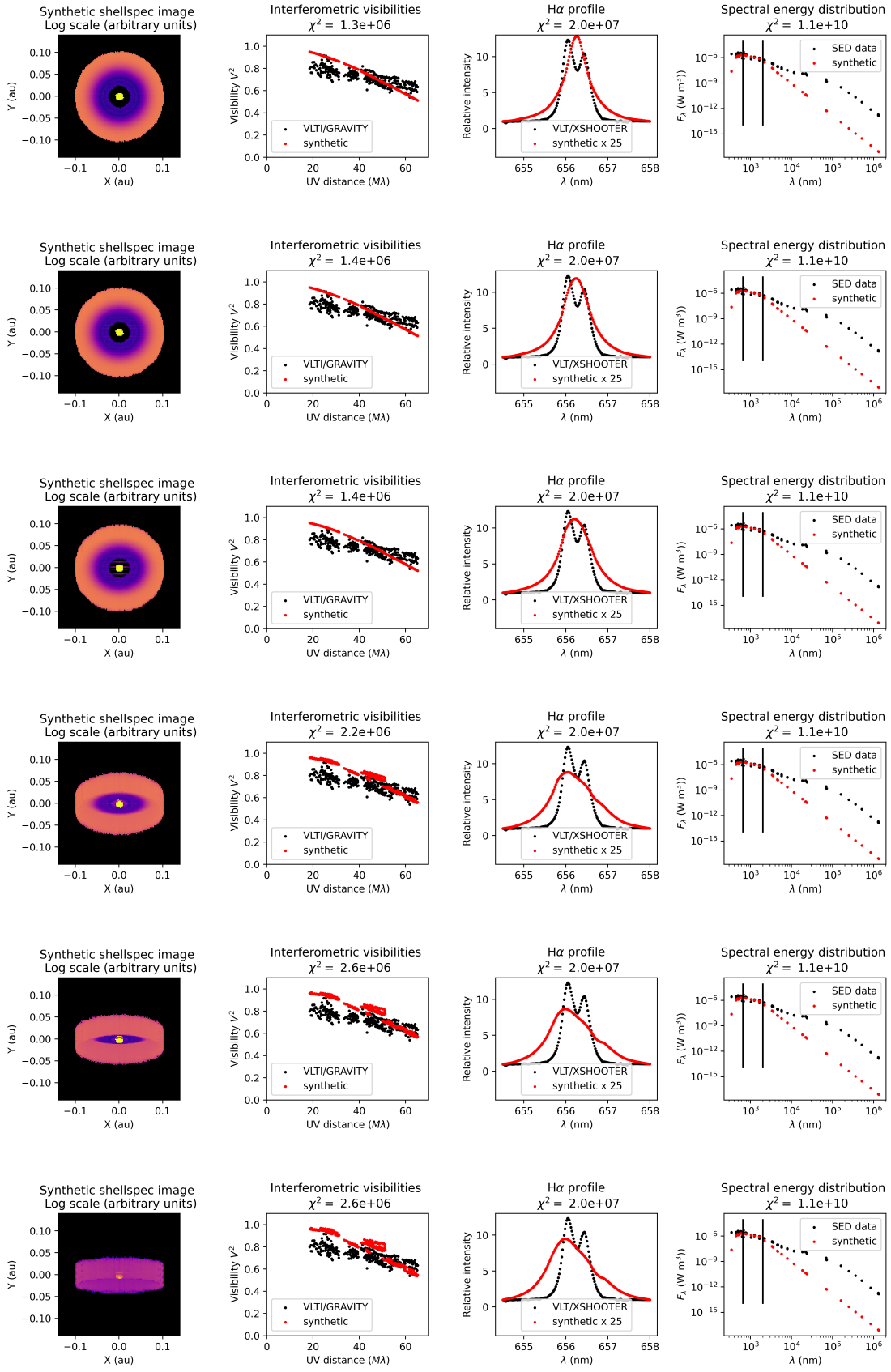

Figure 3.22: Testing of different inclinations of an optically thick innermost disk. From top to bottom, $i = (10°, 20°, 30°, 60°, 70°, 80°)$. Notice that an optically thick disk never produces enough Hα flux (the synthetic profiles are **scaled by a factor of 25**). The parameters in this simulation were: $R_{\mathrm{innb}} = 2\,R_\odot$, $r_{\mathrm{out}} = 22\,R_\odot$, $T(r_{\mathrm{nb}}) = 2000\,\mathrm{K}$, $\varrho_{\mathrm{nb}} = 1 \cdot 10^{-7}\mathrm{g/cm}^3$, $e_{\mathrm{densnb}} = -1$, $e_{\mathrm{tmpnb}} = 0.5$. Thus, the Hα line cannot originate from an optically thick disk.

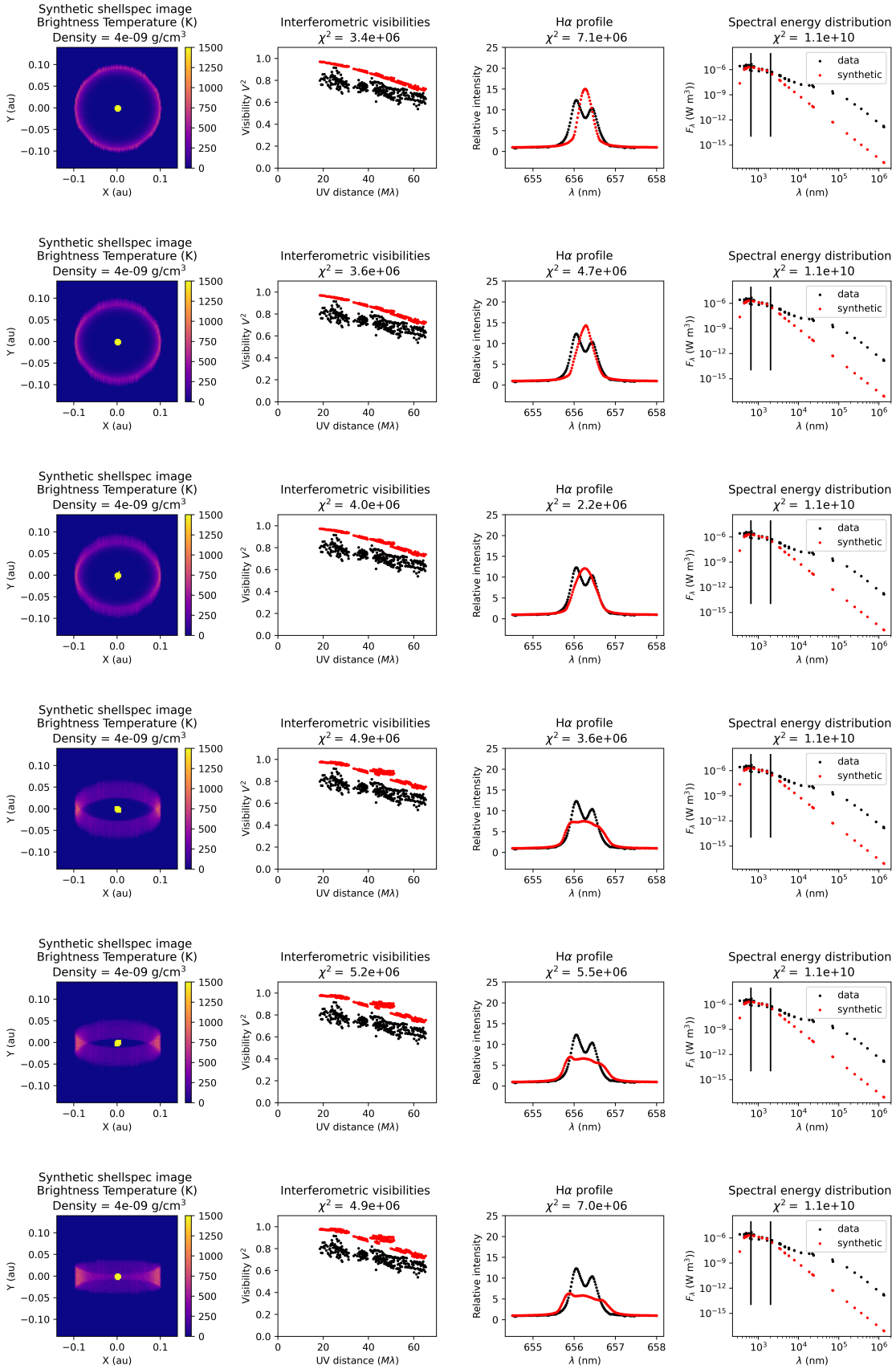

Figure 3.23: The same as Figure 3.22, except in the optically thin regime. Tested for different inclinations, $i = (10°, 20°, 30°, 60°, 70°, 80°)$. **Even at highest inclinations, the double-peaked Hα profile is not reproduced**. $R_{\mathrm{innb}} = 2\,R_\odot$, $R_{\mathrm{outnb}} = 22\,R_\odot$, $T_{\mathrm{innb}} = 2000\,\mathrm{K}$, $\varrho_{\mathrm{innb}} = 4 \cdot 10^{-9}\mathrm{g/cm}^3$, $e_{\mathrm{densnb}} = -1$, $e_{\mathrm{tmpnb}} = 0.5$.

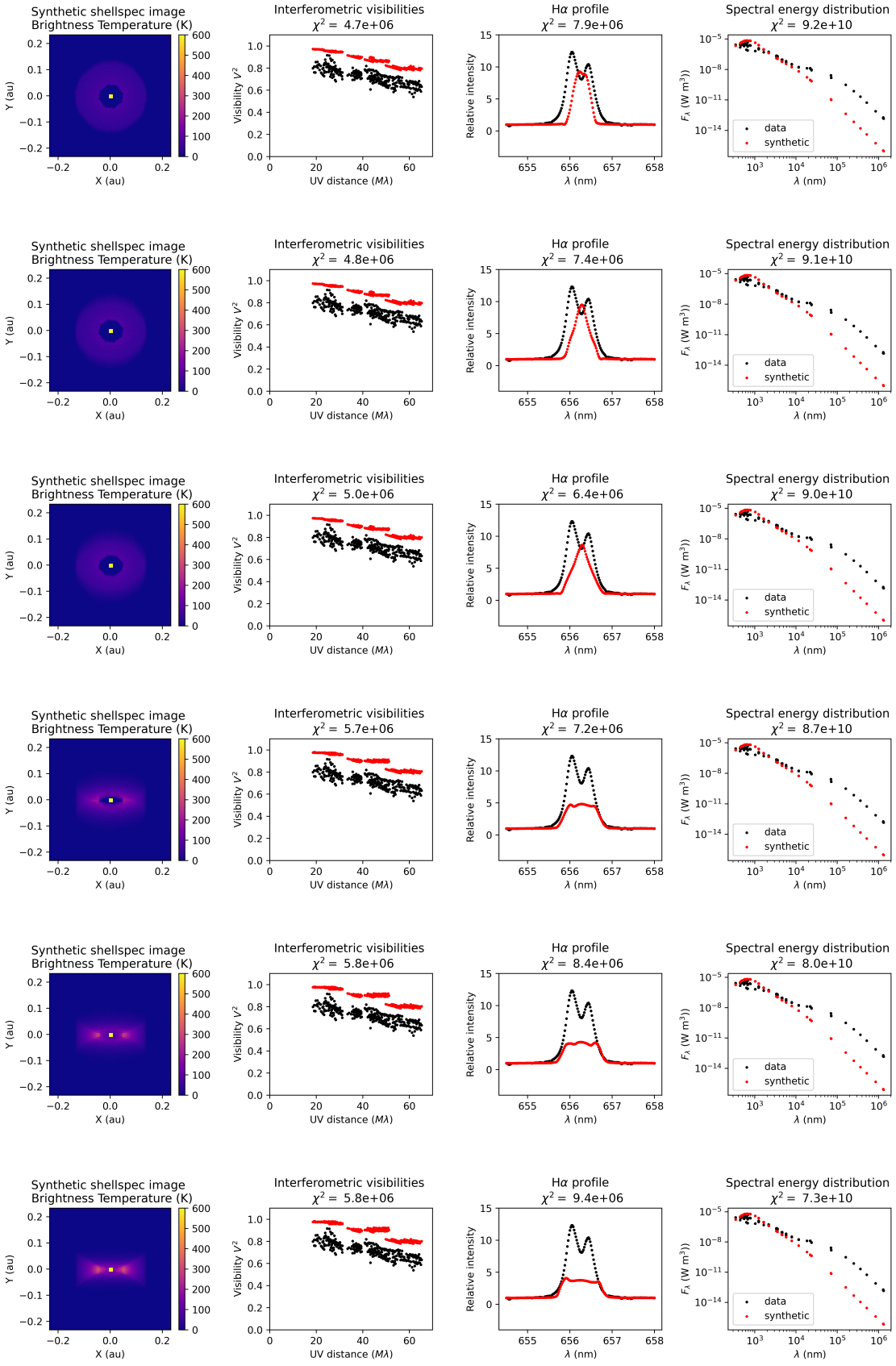

Figure 3.24: Testing of different inclinations of an optically thin innermost disk model at $i = (10°, 20°, 30°, 60°, 70°, 80°)$. The same as Figure 3.23, but with a different (hotter and less dense) temperature and density profile: $R_{\rm innb} = 10\,R_\odot\,, R_{\rm outnb} = 30\,R_\odot\,, T_{\rm nb} = 4800\,{\rm K}\,, \varrho_{\rm nb} = 5 \cdot 10^{-10}{\rm g/cm^3}\,, e_{\rm densnb} = 0\,, e_{\rm tempnb} = 0.$

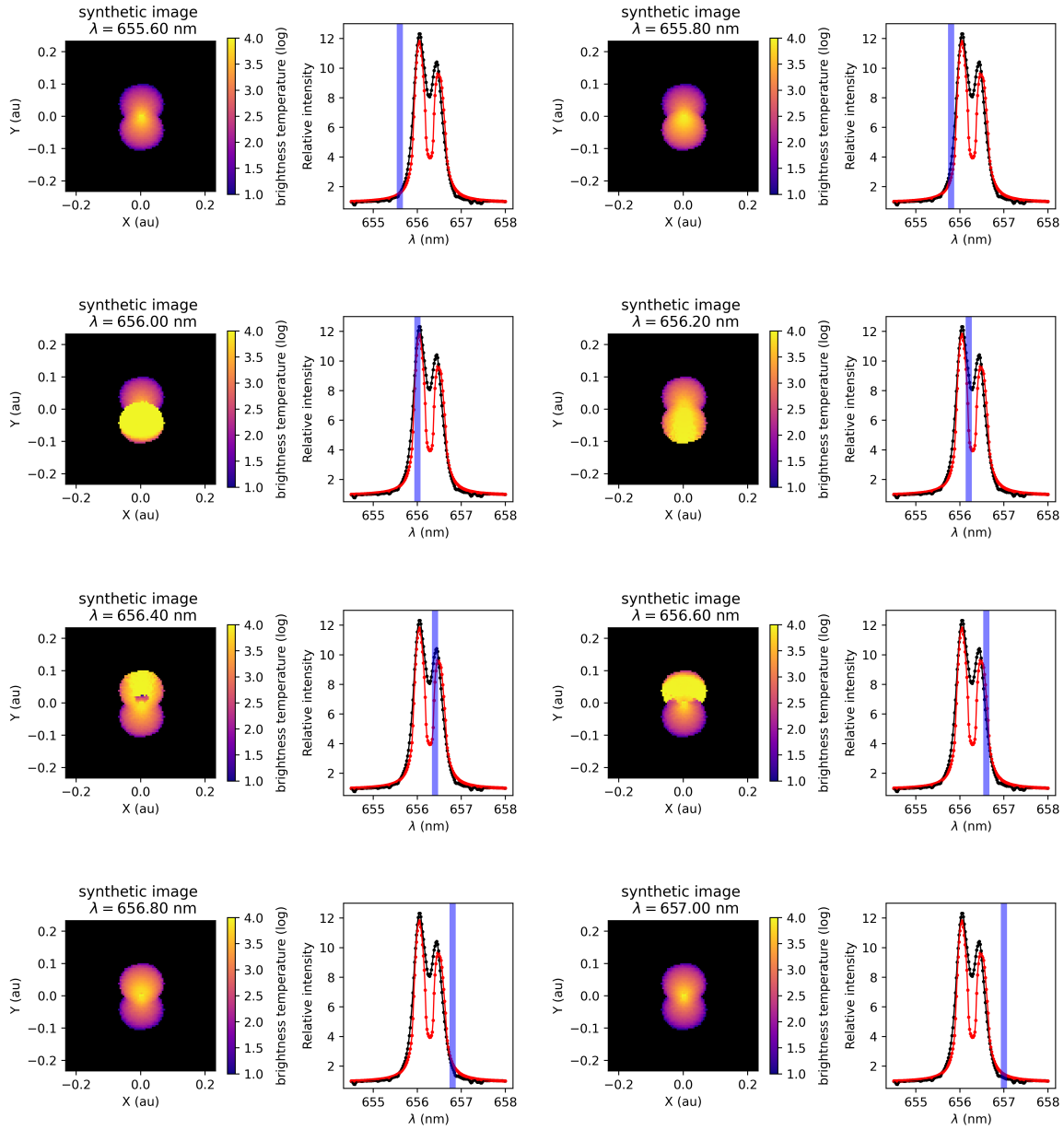

Figure 3.25: Testing spectral line calculations for the jet model of the inner region, with a **positive radial velocity**. The figure shows synthetic images at different wavelengths, from which the spectral line profile is calculated. This model uses the following parameters of the jet: $\alpha_{\rm jt} = 35°$, $R_{\rm injt} = 2\,R_\odot$, $R_{\rm outjt} = 25\,R_\odot$, $v_{\rm jt} = 134\,{\rm km\,s^{-1}}$, $T_{\rm jt} = 7000\,{\rm K}$, $\varrho_{\rm jt} = 1.3 \cdot 10^{-9}{\rm g/cm^3}$.

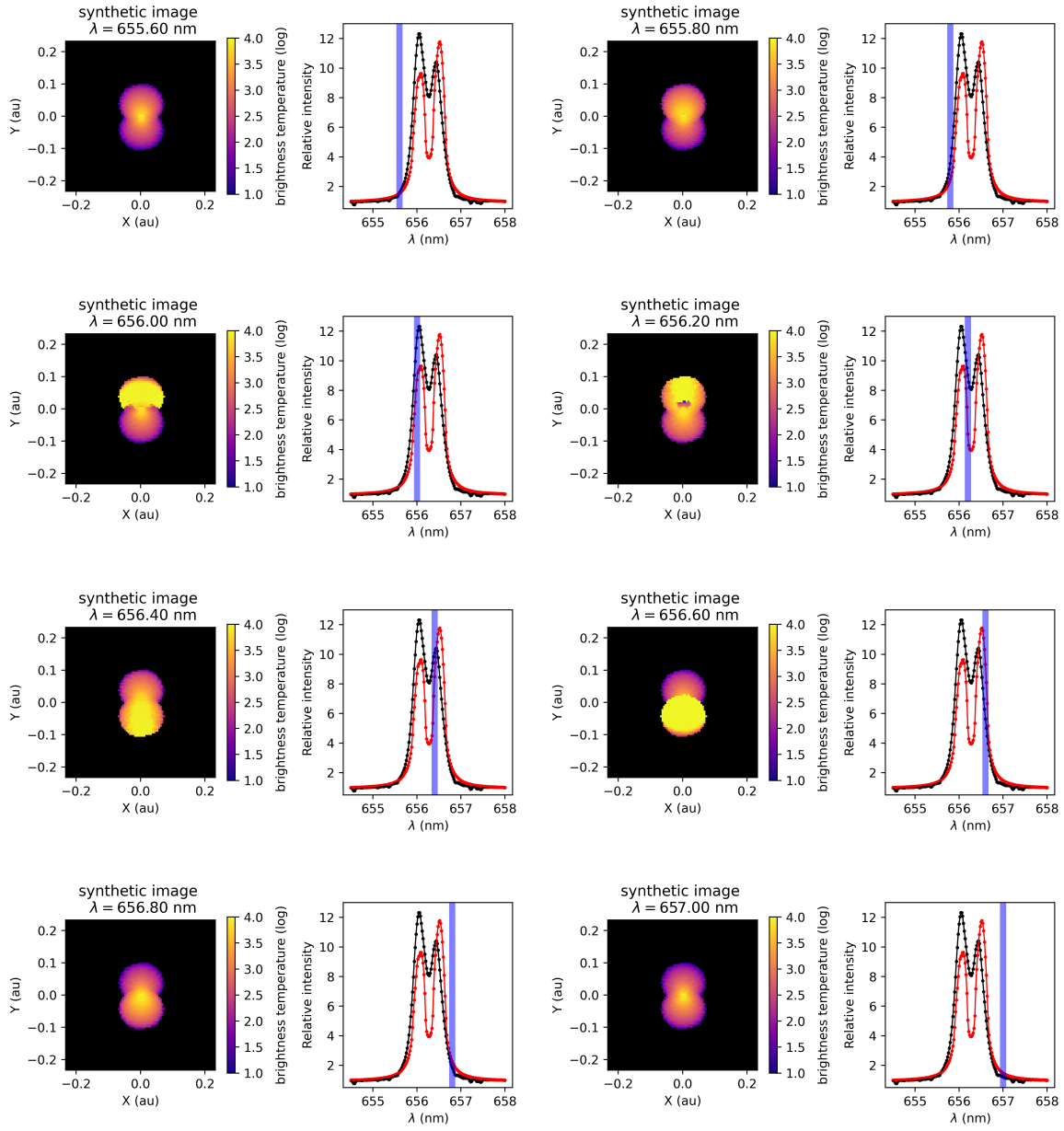

Figure 3.26: The same as Figure 3.25, generated using the same parameters, except with **negative radial velocities** in the jet. This model thus corresponds to an inflow of matter from the polar region. If only Hα measurements were available, the **outflow** model shown in Figure 3.25 would be preferred. However, VLTI/GRAVITY interferometric observations prohibit models without a large optically thick structure (not shown).

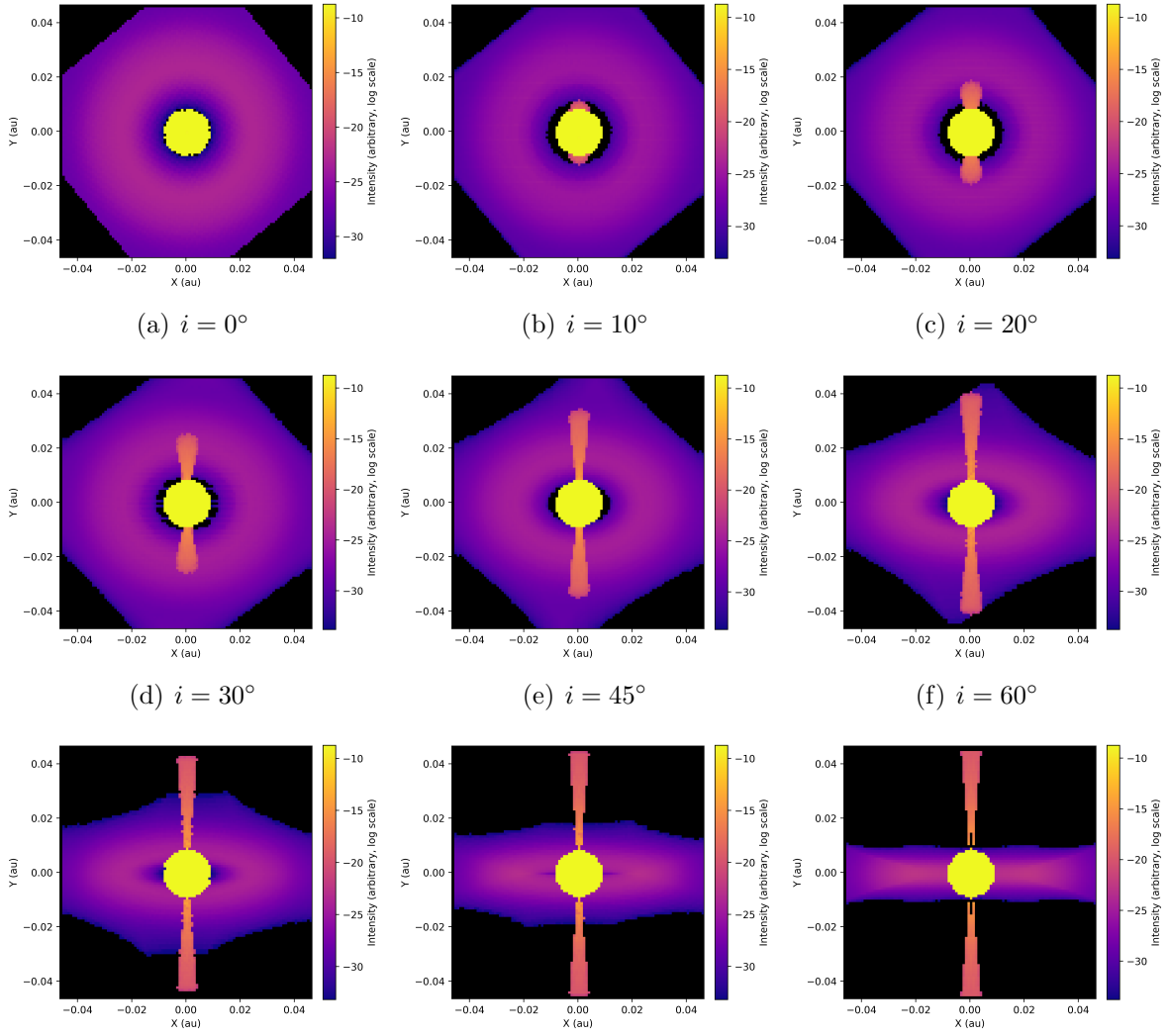

(a) $i = 0°$ (b) $i = 10°$ (c) $i = 20°$

(d) $i = 30°$ (e) $i = 45°$ (f) $i = 60°$

(g) $i = 70°$ (h) $i = 80°$ (i) $i = 90°$

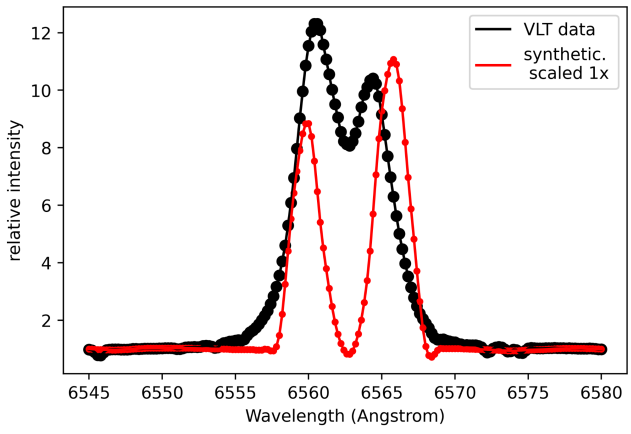

(j)

Figure 3.27: Testing different inclinations $(0°, 10°, 20°, 30°, 45°, 60°, 70°, 80°, 90°)$ of a combined disk and jet model of DoAr 44. This narrow jet geometry does not seem to replicate well the observed spectral line profiles at any inclination, e.g., at $i = 40°$, as shown in subfigure (j).

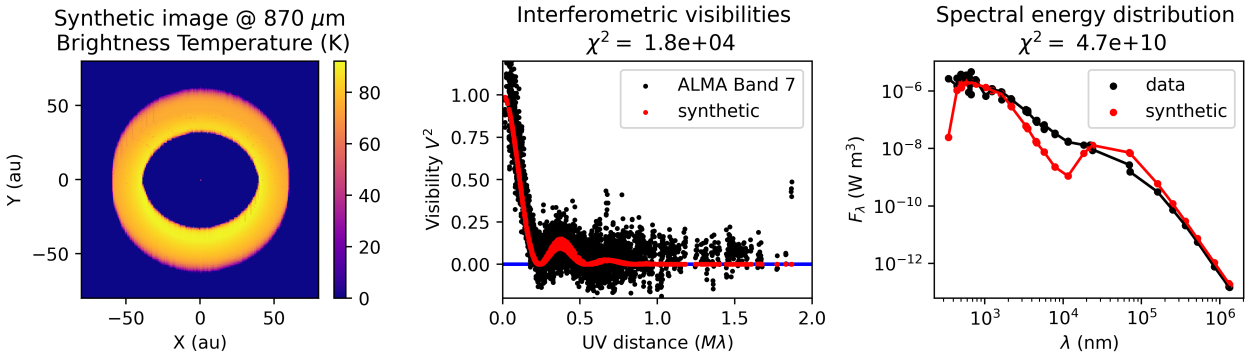

(a) $a = 1\,\mu\text{m}$

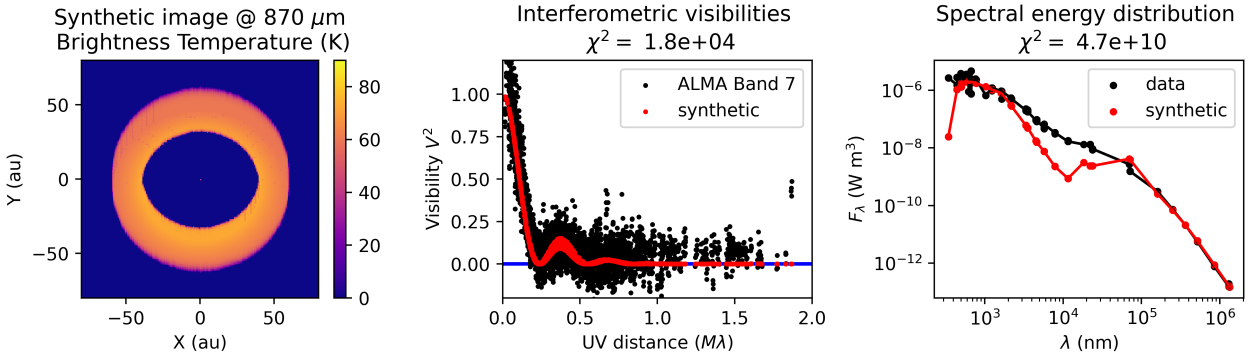

(b) $a = 10\,\mu\text{m}$

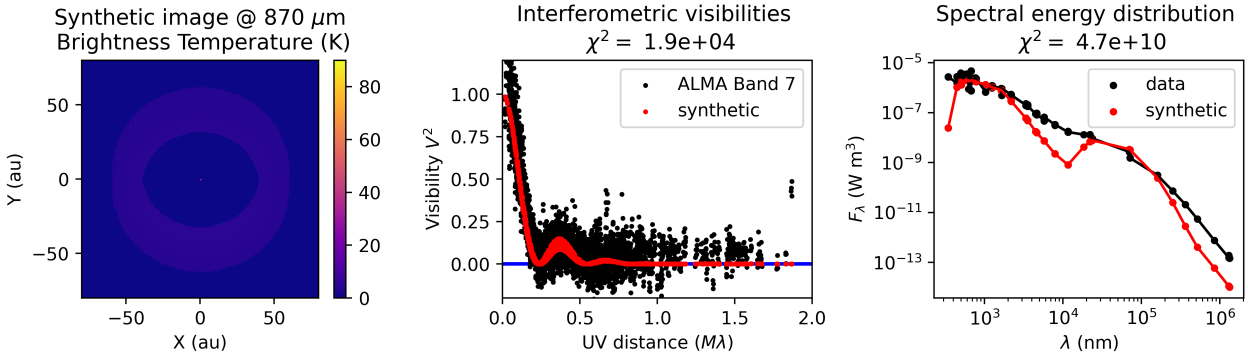

(c) $a = 100\,\mu\text{m}$

Figure 3.28: Testing the effects of particle size on the synthetic images. Increasing the particle size decreases the specific opacity for a given dust density, as the same amount of material has a much smaller effective cross-section. These simulations used water ice as the only dust species, with a density of $\varrho_{\text{dust}} = 1 \cdot 10^{-14}\,\text{g}\,\text{cm}^{-3}$. For the largest particle size of $a = 100\,\mu\text{m}$, we see a large deficit in the sub-mm and mm wavelengths. Notice that another large SED deficit is caused by the missing inner disk in the mid-IR wavelengths.

Chapter 4

Discussion

4.1 The magnetospheric accretion region

4.1.1 [Q1] Is matter being accreted onto the central star, or are we observing stellar winds?

As the matter in the central magnetospheric cavity, where the spectral line emission originates, is optically thin, this question is hard to answer. The VLT/X-shooter profile, where the blue-shifted wing is stronger than the red-shifted wing, indicates that we are observing an outflow. The VLT/UVES profiles are almost symmetric, and solutions with an infalling symmetrical shell look almost identical to the solutions with an expanding envelope.

During the last days of writing this work, I have also found several spectral line measurements from VLT/ESPRESSO. These profiles are almost a mirror image of the VLT/X-shooter measurements, thus suggesting polar accretion inflows.

The following solution presents itself: a steady-state, almost symmetrical inflow of gas from the inner disk is fed onto the central star. During some disturbances (e.g., of magnetic origin) this inflow is concentrated in a funnel-like geometry that could possibly be oriented parallel to the inner disk. As these structures rotate with respect to the observer, they can get partially shadowed by the inner optically thick wall, resulting in one wing of the spectral line being stronger than the other.

Other explanations also come to mind, such as the possibility of disk winds: these are commonly found in many astrophysical disks (Murray and Chiang, 1997), and are almost tangent to the disk's surface. Nevertheless, these winds seem to be generally slower than the Keplerian velocity at small radii, and produce single-peaked lines.

4.1.2 [Q2] What is the geometry of the accretion region?

The detailed geometry of the inner accretion region is variable on the scale of days, and is most likely connected to magnetic funnel flows, described in works like Bessolaz et al. (2008); Takasao et al. (2018); Bouvier et al. (2020a).

Nevertheless, we can describe some general features of this region. In my model, the central star must be surrounded by an envelope of optically thin gas, which lies within the co-rotation radius of the young star ($\approx 15\,R_\odot$). Beyond this radius, a hot innermost disk is present. This disk is likely fueling the accretion by channeling material to the inner shell.

The innermost disk seems to be misaligned by about $(20 \pm 5)^\circ$ with respect to the outer

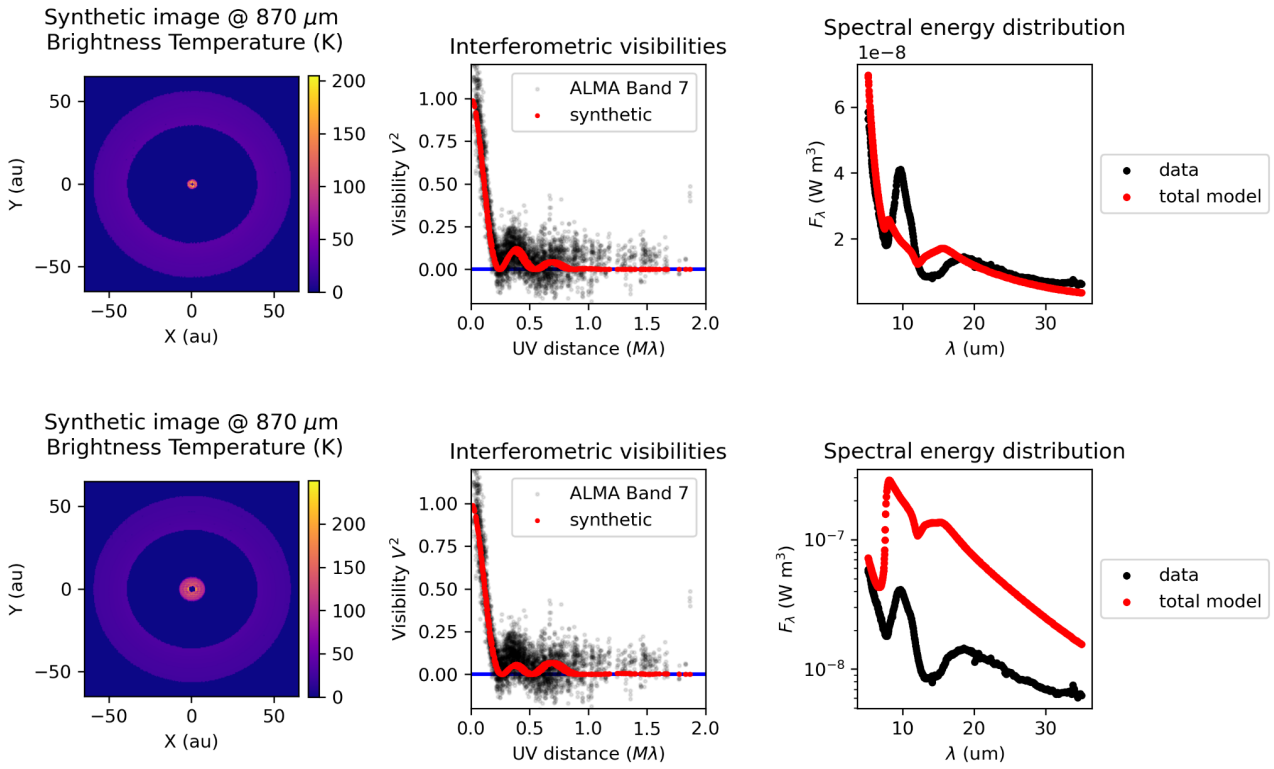

Figure 4.1: Two models of the inner and outer disk in a single radiative-transfer simulation. The dust is a mixture of water-ice, forsterite and enstatite with ratios roughly corresponding to the photospheric elemental composition (90% water, 5% forsterite, 5% enstatite). Both models have a "modest" inner disk temperature $\sim 200 - 500\,\mathrm{K}$. The first one (**top**) has a small inner disk and the second model (**bottom**) has a more extended inner disk. The first model is in good agreement with the global SED (not shown) and ALMA measurements, but the vibrational mode spectral feature at 10 µm remains negligible. The second situation makes this feature very prominent, but overestimates the global SED (not shown), and the absolute mid-IR Spitzer spectra, and would be resolvable by the ALMA observations. This seems to be due to the fact that the silicate features arise from the hottest inner parts of the disk.

disk. Ginski et al. (2021) suggested an elegant explanation for such a misalignment in the disk SU Aur. There, VLT/SPHERE observation revealed tendrils of material connecting the outer and inner regions, likely carrying material inwards. These tendrils are dramatically asymmetric and introduce angular momentum to the inner region.

4.2 Outer disk

4.2.1 [Q3] Is it necessary to describe the large observed cavity between the inner disk and the outer ring as a drop in surface density?

We can conclusively say that with a constant dust particle size in the entire disk, it is not possible to create the ring morphology inferred from the ALMA visibilities. However, with a variable particle size, it is of course possible to create rings without the necessity to change the integrated surface density.

For optically **thin** thermal emission, it holds that:

$$I_\nu = B_\nu(T)(1 - e^{-\tau}) \,,$$

where B_ν is the Planck function at temperature T and τ is the optical thickness in the vertical direction. The optical depth can be expressed as:

$$\tau = \kappa_\nu^{\text{abs}} \Sigma \,, \tag{4.1}$$

where κ_ν^{abs} is the absorption opacity and Σ the surface density. The absorption opacity (Figure 3.16) is a complicated function, but can be approximated by a power law of frequency on a narrow frequency range:

$$\kappa_\nu \sim \nu^\beta \,.$$

This quantity can be accessed using the spectral index, defined as:

$$\alpha = \frac{\partial \log F_\nu}{\partial \nu} \,. \tag{4.2}$$

This spectral index can be evaluated at every point of the disk, or in an azimuthally averaged radial profile. In practice, this quantity is derived from a discrete number of measurements, often pairwise. For DoAr 44, a recent[1] study (Arce-Tord et al., 2023) performed this spectral index analysis between the ALMA Bands 6 and 7, calculating:

$$\alpha = \frac{\log_{10}(I_{350\text{GHz}}) - \log_{10}(I_{244\text{GHz}})}{\log_{10}(350\text{GHz}) - \log_{10}(244\text{GHz})} \,. \tag{4.3}$$

As the blackbody emission is operating in the Rayleigh–Jeans regime, we can express:

$$I_\nu = \frac{2 k_B T \nu^2}{c^2}(1 - e^{-\tau}) \,,$$

which for small optical depths becomes:

$$I_\nu = \frac{2 k_B T \nu^2}{c^2}(1 - e^{-\tau}) \approx \frac{2 k_B T \nu^2}{c^2}(1 - 1 + \tau) = \frac{2 k_B T \nu^2}{c^2} \kappa_\nu^{\text{abs}} \Sigma \sim \nu^{2+\beta} \,.$$

[1] Published during the writing of this thesis.

We can measure the quantity $\alpha = \beta + 2$, and thus derive the value of β. The Figure 3.16 only shows the opacity of particles up to 100 µm. The trend for even larger particles continues, so that the opacity is almost independent of frequency on smaller frequencies, i.e., a slope of $\beta \approx 0$. Arce-Tord et al. (2023) found the value of $\beta \approx 1.3$ in the inner cavity, and $\beta \approx 0$ in the most prominent part of the ring at $R = 48$ au. The large values of β can be interpreted as very small particles, only slightly larger than in the interstellar medium, where $\beta \approx 1.7$ (Draine, 2006). The value of $\beta = 0$ could either mean large particles (cm–sizes) or optically thick emission.

I presume the former option is more probable, as the observed brightness temperature in both bands is much lower, than the thermodynamic temperature needed in our models, indicating that the emission really is optically thin. However, it is important to note that the models in this work did not include these cm–sized pebbles, as I used the Budaj et al. (2015) dust tables, and the opacities I have used differ from those proposed by Beckwith et al. (1990) which were for example used for the dust mass estimates by The ODISEA (Cieza et al., 2021).

4.2.2 [Q4] Does the observed ring coincide with a condensation line of a volatile, or must it be caused by an exoplanet?

My models suggest the temperature at the inner edge of the outer disk is about $T_{\rm nb} = 60$ K and that the emission in the sub-mm region is optically thick. This temperature could be as low as $T_{\rm nb} = 50$ K if the emitting area of the disk is assumed to be larger.

Assuming the best monotonic profile (see parameters in Table 3.7), and calculating the temperature at $R = 49$ au, which is the ring maximum, one obtains:

$$T = T_{\rm nb(monotonic)} \left(\frac{R}{R_{\rm innb}} \right)^{e_{\rm tempnb}} = 600\,{\rm K} \sqrt{\frac{108\,R_\odot}{49\,{\rm au}}} = 61\,{\rm K}\,.$$

This is in good agreement with the cavity models.

Moreover, mid-plane temperatures around 50 au in other protoplanetary disks, such as HL Tauri, can also reach around 50–70 K (Zhang et al., 2015).

The scientific literature about solar system comets, which originate from these cold outer regions, is a good guide with respect to the expected chemical composition. The major **volatiles** found in comets are H_2O, CO, CO_2, CH_4 and NH_3, with water ice being typically most abundant. The comet's composition is often given with respect to the water ice content. CO can contribute up to 30 % of the mass of the water ice, CO_2 up to 10 %, and the other chemicals usually contribute less than 1 % (Greenberg, 1998). Different ratios were obtained for example by Rosetta orbiting 67P/Churyumov-Gerasimenko, where CO_2 formed 7.5 % and CO 3 % (Rubin et al., 2023). These ratios might be lower than what we expect in the outer disk, as 67P/Churyumov-Gerasimenko is a periodic comet, which effectively looses highly volatile ices during every perihelion passage.

Water ice does *not* seem like a good candidate for the condensation line at this distance. Given the temperature profile from my models, the water ice line occurs somewhere between 4–6 au, similar to the ≈ 3 au water ice line distance in our early solar system.

The condensation of **carbon monoxide** is *not* responsible for the for the condensation line at this distance, as we can see the CO gas emission extending far away beyond the dust structures, into even colder regions — see Figure 4.2.

Possibly, **carbon dioxide** *could* be transitioning from the gaseous to the solid state at the peak emission radius in DoAr 44, based only on the modeled temperature and pressure profiles. However, we must proceed with caution: solid CO_2 is associated with mid-IR bands, which

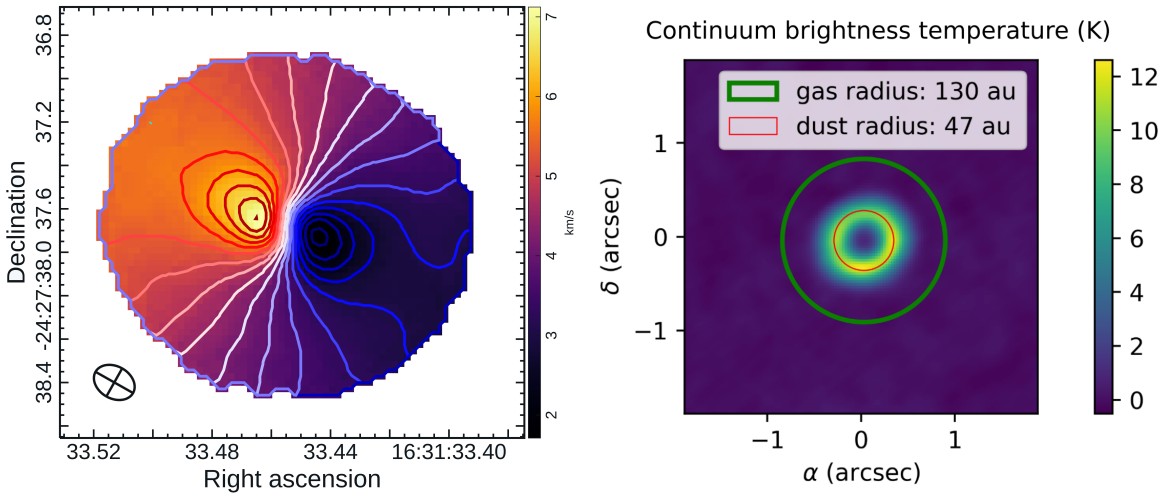

Figure 4.2: The gas is much more extended than the dust in DoAr 44. **Left**: A radial velocity map from CO $v = 0, J = 3 - 2$ line emission, showing the extent of the gas. **Right**: Comparison of the extent of the CO gas (130 au) in comparison to the maximum emission from the dust (47–49 au). This observation suggests that the continuum emission is in fact optically thin, as the CO must be in gaseous form for us to see the rotational transitions. CO condenses at about 25 K (at Kuiper belt pressures). Therefore, the dust temperature must be significantly higher than the observed brightness temperatures, and thus the emission should be optically thin. The figure was taken from the SFG report Souza de Joode (2022).

would be in the range observed by the Spitzer/IRS instrument. These CO_2 bands around 15 µm are often observed around YSOs (Cook et al., 2011). Due to the complicated nature of the silicate spectral features overlapping with the possibly present solid CO_2 feature, I have decided to refrain from further interpretations.

The possibility of other volatiles condensing, forming the ring in DoAr 44, seems improbable due to the total dust mass in the outer disk. There is probably more than 80 M_{Earth} of dust in the outer disk, which means it cannot be composed of some rare chemical.

The work of Zhang et al. (2015) modeled the disk HL Tauri based on ALMA observations in two different bands. They found that the **dips** in intensity in HL Tauri could correspond to condensation lines of water ice, ammonia and carbon monoxide. They agree that material accumulates at these condensation lines, but argue that this accumulation leads to rapid growth of pebbles to decimeter sizes. These pebbles then disappear from the ALMA images, as their total emitting area is much smaller than that of the dust. The timescale of this process is of the order of thousands of years.

The planet formation mass budget Integrating the surface density of the outer disk along the radial coordinate we obtain the total planet formation mass budget:

$$M_{\text{gas}} = \int_{R_{\text{innb}}}^{R_{\text{outnb}}} 2\pi r \Sigma_{\text{gas}}(r) \mathrm{d}r \,. \tag{4.4}$$

Depending on the chosen model of the outer disk, mainly depending on the chosen particle size, we obtain mass estimates in the range of:

$$M_{\text{gas}} \in (25, 100) M_{\text{Jupiter}} = (8000, 32000)\, M_{\text{Earth}} \,,$$

and assuming a metallicity of 1 %, we obtain:

$$\boxed{M_{\text{dust}} \in (80, 320)\, M_{\text{Earth}}} \,.$$

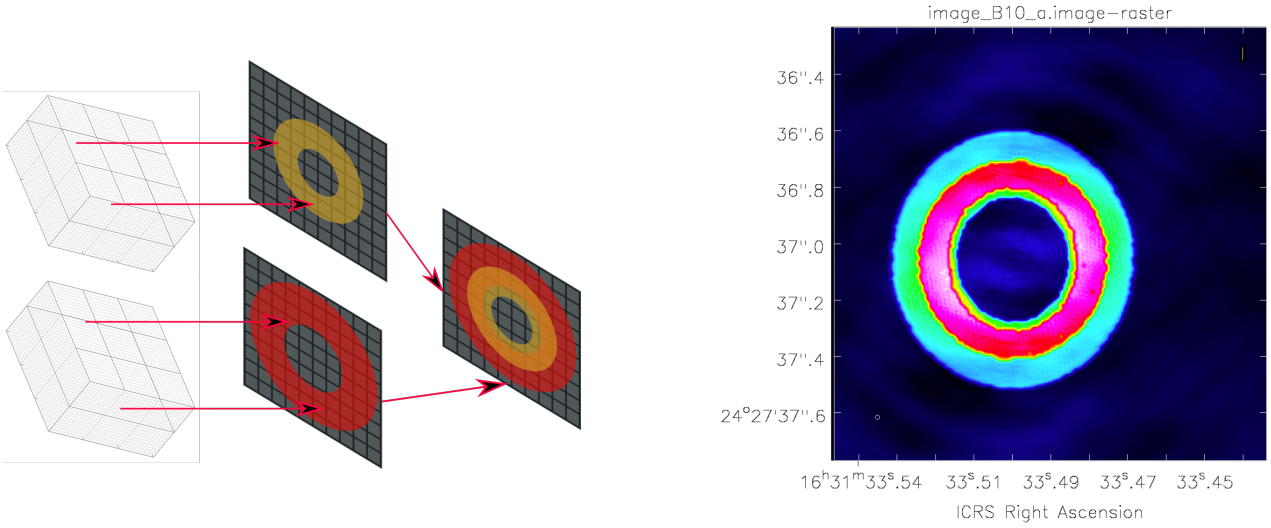

Figure 4.3: A non-radiative-transfer simulation can be justified if the medium is optically thin, which seems to be the case for the mm continuum emission in the outer disk. The double ring (ring-within-a-ring) profile was thus obtained by simply superposing two simulations. This optically thin assumptions seems be reasonable, as an optically thick disk at 48 au and $\lambda = 1.3\,\mathrm{mm}$ would have to have a surface density 20 times larger than the Minimum Mass Solar Nebula (MMSN). Such a local density increase can be achieved, however, at a condensation front. The right image was obtained using the `casa` task `simobserve`, which produced the complex visibilities as sampled by the configuration used in the 2018.1.00028.S Band 6 observations. Then, it was restored using the `casa` task `tclean`, using about $2 \cdot 10^4$ point sources convolved with the synthesized beam.

Such a figure is similar to what is commonly presumed for our own solar system ($\approx 130\,M_{\mathrm{Earth}}$), and to the result of $M_{\mathrm{dust}} \simeq 90\,M_{\mathrm{Earth}}$ obtained by Leiendecker et al. (2022). This leads us to think that the ring structure at 48 au, seen in the ALMA data, might very well be a good analog of the Kuiper belt in our own solar system, which currently extends from about 30 au to about 55 au.

4.3 Other questions

Possibility of VLTI spectro-interferometry The measurements performed in June 2019 by VLTI/GRAVITY, spanning the range 1.99 µm to 2.45 µm captured the spectral range corresponding to the Hydrogen Brγ line. However, it is only barely noticeable in only some of the `OIfits` files, only at a few baselines. Additionally, there are missing data points in the proximity of this line proximity, and it is not certain whether it is a real signal. It does however appear to be consistent over the various epochs. Nevertheless, I have decided not to include it in this analysis.

Such attempts have been made by Bouvier et al. (2020b): the visibilities in the Brγ line were slightly above the continuum visibilities, indicating that the line emission originates from a region more compact than the continuum emission, indicating there might be a contribution from the optically thin matter near the star.

Modeling the silicate dust feature The Spitzer/IRS spectrograph acquired spectra of DoAr 44 in the 3–5µm range, capturing a prominent feature at 10 µm. This feature is associated with the vibration of the Si-O bonds in a crystalline lattice of silicates. Even though silicate dust

emission is included in our model, I did not yet succeed in reproducing the spectrum. Note that modelling such features is exceptionally challenging, as it requires very precise vertical density profiles, particle sizes and particle size distributions, temperature profiles and also the correct mineralogical composition.

Presence of the silicate feature Simply looking at the Spitzer spectrum, it is not clear whether we are looking at:

1. a real feature in the protoplanetary disk,
2. an absorption feature from the foreground Interstellar Medium (ISM),
3. an emission feature from the foreground ISM.

In principle, all three options are viable: the dust in the ISM efficiently absorbs stellar light and re-emits it as thermal radiation. However, there are conflicting opinions on this issue:

1. The gas and dust temperature in the interstellar medium in these star formating regions is only about 20 K (Lindberg et al., 2017; Ksoll et al., 2024), which is insufficient to excite the SiO bond vibrations on its own.
2. Since the Infrared Space Observatory (ISO) spectra have been available, it has been thought there is an almost complete absence of crystalline silicates in the ISM (Kemper et al., 2004), and that they have to form around the young star. This has been the accepted view for many years.
3. However, recently there have been analyses claiming that the situation is more complicated, that crystalline silicate dust forms about 10% – 20% of the ISM, and that they are ubiquitous in the ISM (Do-Duy et al., 2020). In such a case, modeling the protoplanetary disk based on these spectra would be very challenging, as the 10 micron spectral feature could be produced in the foreground material.

In light of this "confusion", I have decided not to further interpret this Spitzer spectrum.

4.4 Further theoretical work

As with all projects, the possibilities for further study are endless. Here are a few of my suggestions for the future development of `Pyshellspec` for protoplanetary disk applications:

1. One has to think about the extrapolations used for the large dust particles. In evolved disks, most of the dust mass is in pebbles, spanning from millimeters to decimeters. There are two issues: firstly, I am not modeling the opacity of these pebbles at the moment. This might not be a problem, as their total contribution to the emitting (and scattering) area is probably much smaller compared to the micron and ISM sized dust. Secondly, we are extrapolating the opacity relations of the small dust we are using to the sub-mm wavelengths. In the case of scattering, this is not an issue, as the Rayleigh scattering is well understood. This might be an easy fix, e.g., using the tables from RADMC-3D (Dullemond et al., 2012), and should be checked against the power-laws from Beckwith et al. (1990).

2. At the moment, it is difficult to fit the inclination of the disk via χ^2 minimization. This is due to the fact that the tool was originally developed and designed for double star modeling, where the observables and derived quantities are slightly different from our case (periods of rotation, the q–ratio, ...).

3. The case of DoAr 44 is complicated by the fact that the density profile does not appear to be like the traditional power-laws of Hayashi (1981) or Lynden-Bell and Pringle (1974). Nevertheless, I believe that a (slightly) closer match of the density profile would not produce order-of-magnitude changes to the outer disk mass budget.

4. At the moment, `Pyshellspec` does not support χ^2 calculations of the difference between synthetic images and, for example, observed images from adaptive-optics instruments like VLT/SPHERE. I can imagine the following work-around: we could take a discrete Fourier transform of the image and selecting a reasonable sub-sample of it. Thus, one could "pretend" the data was taken by an interferometer, and we could use the tools we already have. I believe there is nothing fundamentally wrong with this approach, even though it might sound convoluted.

5. Some visibility scaling parameters could be introduced into `Pyshellspec` itself. I had to scale the ALMA visibilities with the help of analytical models. In this particular case, I believe it worked very well.

6. At the moment, our tool cannot effectively model the shadowing of the outer disk caused by the inner disk, as we cannot model the relative inclinations. Adding this capability might be challenging.

4.5 Further observations

As a part of this work, I would like to present **my ALMA proposal for a Band 10 observation** of the inner disk of DoAr 44. It details and justifies all the technical requirements, such as the angular resolution, maximum recoverable scale, antenna configuration, sensitivity, integration time, calibrator selection, the required weather conditions, the central frequency and bandwidth and correlator settings. This proposal was submitted to ALMA on the 25th of April 2024, and is presented in Appendix A.

The James Webb Space Telescope Other ideas for observations naturally come to mind. The James Webb Space Telescope (JWST) narrowly avoided our target, as it would have presumably saturated the NIRCam instrument – see Figure 4.4. JWST/MIRI spectra would most likely resemble the Spitzer/IRS spectra, as these instruments cover the same spectral range. The hot water vapor lines, reported by Salyk et al. (2015) could be resolved with higher spectral resolution. However, the forsterite/enstatite features would face the same difficulty as I have faced with the Spitzer spectra. Several HST images of DoAr 44 also exist, but are all over-saturated.

VLTI/MATISSE Potentially, a very useful set of observations could be obtained using also VLTI/MATISSE in the N band. This would cover the same spectral range as Spitzer or JWST/MIRI, but would provide a spatially resolved picture. The IRAS and Spitzer measurements indicate that in the 8–10 micron range, the measurements reach 0.9–1.4 Jy flux densities.

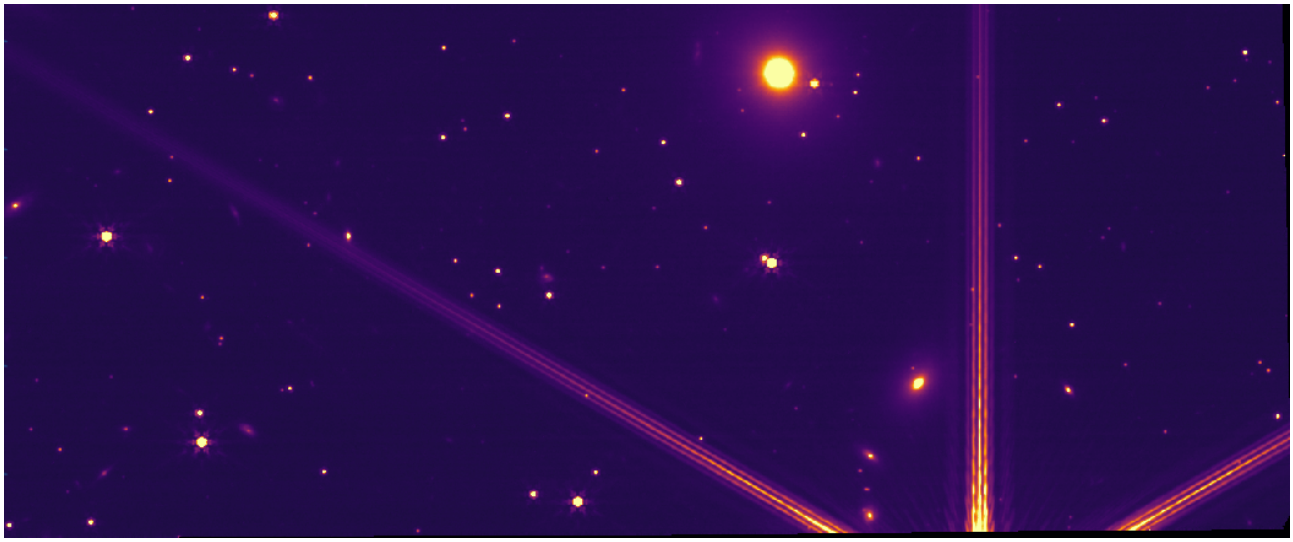

Figure 4.4: The James Webb Space Telescope NIRCam image of the field next to DoAr 44 from the 7th of March 2023. The large diffraction spikes covering the entire frame originate from DoAr 44, which is 3 arcseconds below the bottom of the frame. Taken from the ESO archive: (Delmotte et al., 2006) .

This would result in about 0.1 precision on the visibility measurements with VLTI/MATISSE in the N band using the UTs, reaching about 13 mas resolutions, and there is no chance of being able to use the ATs. This is about the same angular resolution requested by the ALMA measurement. There might, however, be some additional considerations that could complicate matters.

Specifically, the flux density limits in the N1, N2, and N3 sub-bands are 0.9, 1.5, and 2 Jy, to achieve 0.1 precision on the visibility measurements using the UTs. However, going below this limit appears to mean that the precision of the visibilities will be limited, but the interference fringes will still be detectable – these measurements, together with the limits, are shown in Figure 4.7. Different instrument setups are also available, such as the `GRA4MAT` mode, where the fringes are tracked by the VLTI/GRAVITY while MATISSE records them. This in fact **would be possible**, as our target is very bright in the K band. The magnitude limits for this mode are 0.1 and 0.5 Jy for $R \sim 20$ and $R \sim 220$ spectral resolutions, respectively, so DoAr 44 is comfortably within these limits.

I have used the same inner disk models from the ALMA proposal to calculate simulated interferometric visibilities in the N1 and N2 sub-bands. These measurements would constrain the possible inner disk geometries (see middle panels of Figures 4.5 and 4.6), even with an errorbar of 10%.

I have consulted these estimates with an ESO support scientist for VLTI/MATISSE, who **believed it to be possible** to observe the inner disk of DoAr 44 in the N1 and N2 sub-bands. Such observations would be in perfect synergy with the potential ALMA Band 10 observations. The VLTI/MATISSE observations would definitively conclude, whether the forsterite bands originate from DoAr 44 or from the foreground medium. If it were the former, it would allow for the direct interpretation of the Spitzer/IRS spectra, and potentially justify James Webb Space Telescope spectroscopic observations.

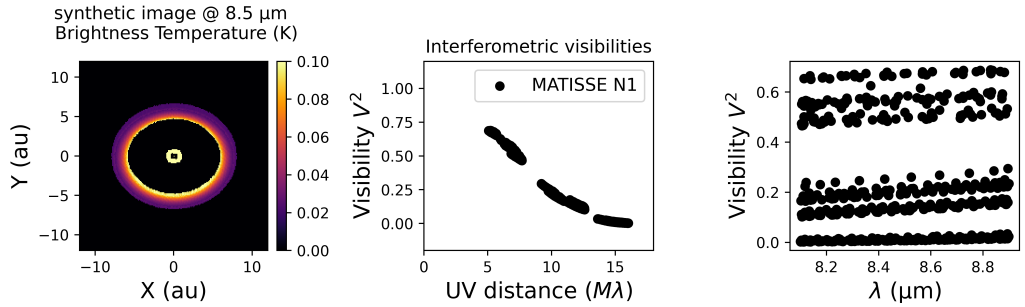

(a)

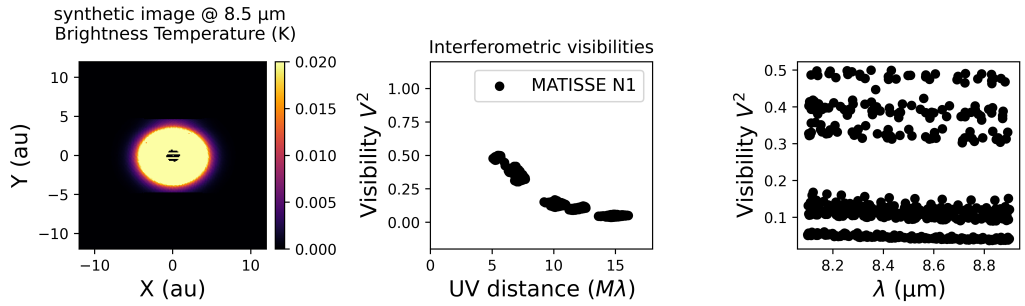

(b)

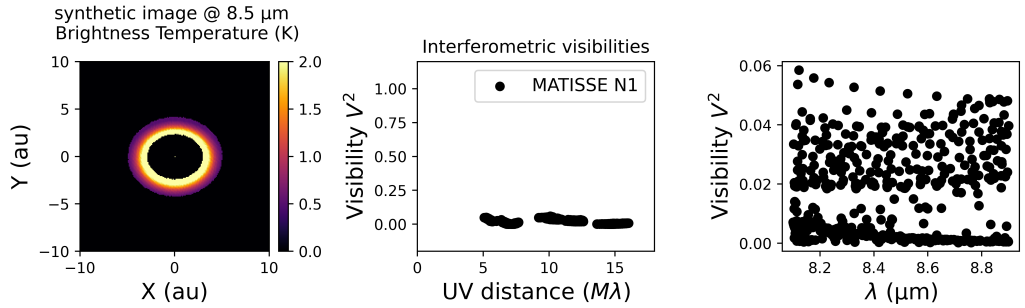

(c)

Figure 4.5: Simulated VLTI/MATISSE interferometry of DoAr 44, in the N band, in the N1 sub-band (8.1–8.9 micron). The differences shown between the presented models are certainly within the reach of the instrument.

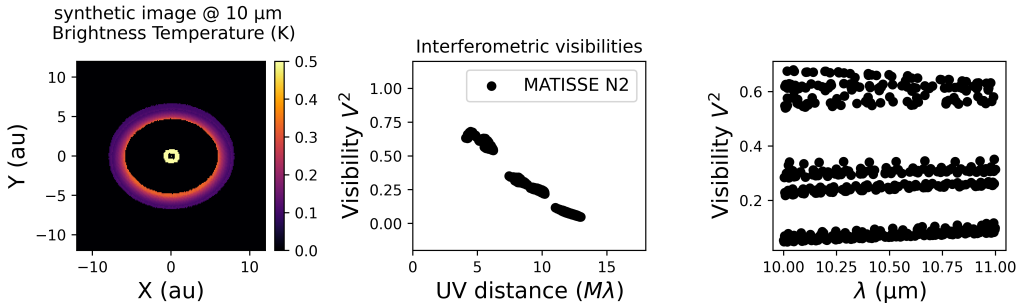

(a)

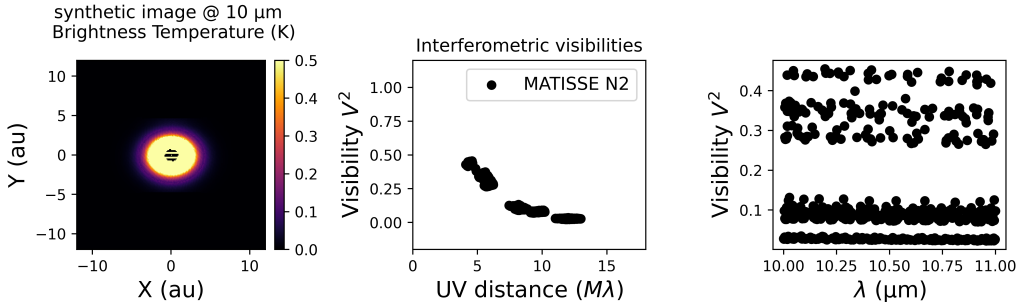

(b)

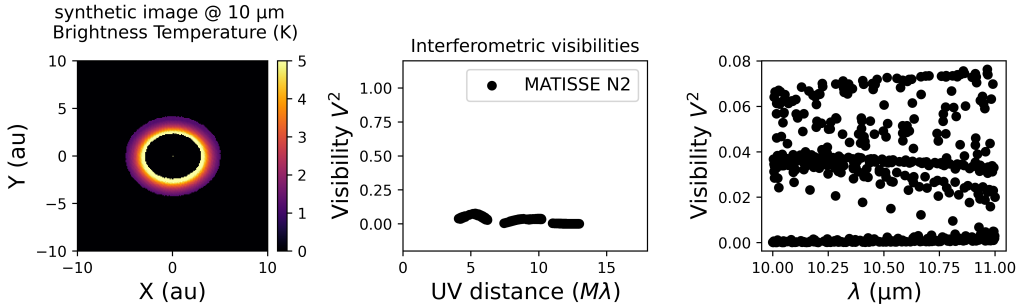

(c)

Figure 4.6: Simulated VLTI/MATISSE interferometry of DoAr 44, in the N band, in the N2 sub-band (10–11 micron). These observations would allow us to study silicates in the terrestrial planet forming region of DoAr 44.

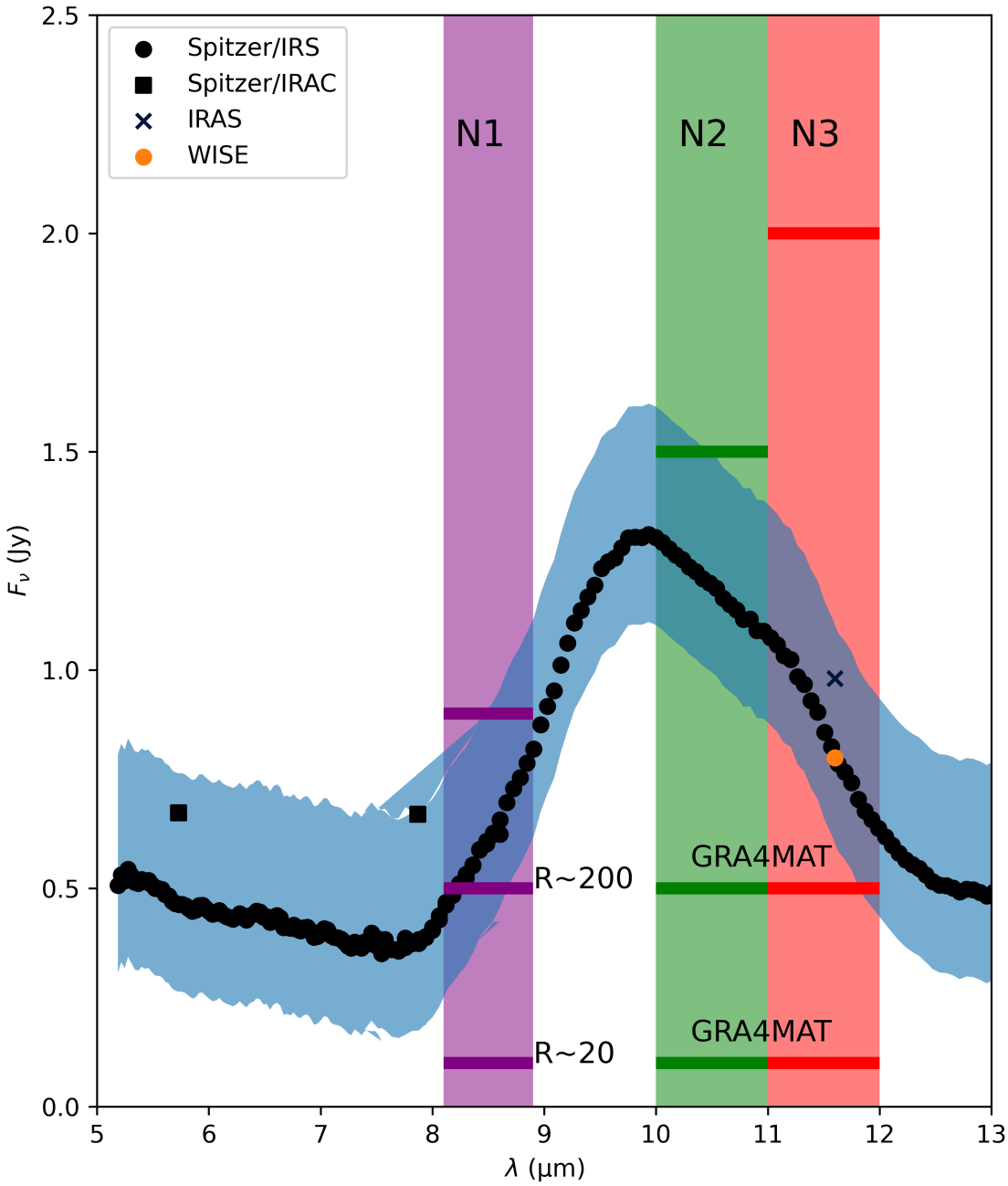

Figure 4.7: The Spitzer/IRS spectrum of DoAr 44, showing the prominent silicate dust feature, together with several photometric measurements from Spitzer/IRAC, the IRAS and Wide-field Infrared Survey Explorer (WISE). The VLTI/MATISSE N1, N2 and N3 sub-bands are shown (labeled rectangles), together with the minimum flux densities for a 0.1 visibility precision (0.9, 1.5 and 2 Jy respectively). It appears that it would be possible to observe resolve the condensation lines of forsterite and enstatite, giving us **spatially resolved mineralogical information.** This would be extremely useful in relation to the models of formation of our own solar system.

Chapter 5

Conclusions

In this work, I present the first global radiative-transfer model of the protoplanetary disk DoAr 44, based on VLT/UVES and VLT/X-shooter spectra, VLTI/GRAVITY squared visibilities, triple product amplitudes and closure phases, ALMA interferometry, and a variety of spectral energy distribution measurements, spanning from the near ultraviolet to millimeter wavelengths. From this model, I have concluded the following:

1. The geometry of the inner accretion region can be described using a shell of gas, heated to about 10 000 K, surrounding the young star. This gas is moving at speeds up to $330\,\mathrm{km\,s^{-1}}$. This shell is surrounded by an innermost disk ($16\,R_\odot$ to $35\,R_\odot$), which is responsible for the VLTI/GRAVITY K-band visibilities.

2. The accretion rate is already low, $\dot{M} = (6.6 \pm 0.2) \cdot 10^{-9}\,M_\odot\,\mathrm{yr}^{-1}$, but not negligible.

3. The dust emission in the outer disk extends from about (36 ± 1) au to about (60 ± 4) au. A large part of the emission is localized in a thin ring centered at (48 ± 1) au. The temperature in this region is about 60 K. The observations are not compatible with a monotonic density profile, and a large central cavity must be present. This cavity was most likely cleared by forming protoplanets.

4. The ring at (48 ± 1) au does **not** correspond to the condensation line of water ice or carbon monoxide. The only possible condensation line that could cause such a ring is carbon dioxide.

5. The mass of gas and dust currently present in the outer disk is more than $25\,M_{\mathrm{Jupiter}}$.

6. An inner disk, unresolved by ALMA, extending from 1 au to at most 10 au, **must be present**.

Thanks to newly offered capabilities (high frequencies, long baselines), the inner disk could be observed with ALMA for the first time next year (2025). A proposal for this observation has been submitted.

Acknowledgements

This paper makes use of the following ALMA data sets: ADS/JAO.ALMA#2019.1.00532.S, ADS/JAO.ALMA#2018.1.00028.S. ALMA is a partnership of ESO (representing its member states), NSF (USA) and NINS (Japan), together with NRC (Canada), NSTC and ASIAA (Taiwan), and KASI (Republic of Korea), in cooperation with the Republic of Chile. The Joint ALMA Observatory is operated by ESO, AUI/NRAO and NAOJ.

Based on observations collected at the European Organisation for Astronomical Research in the Southern Hemisphere under ESO programme(s) 69.C-0481, 093.C-0658, 085.C-0764.

This work has made use of data from the European Space Agency (ESA) mission *Gaia* (https://www.cosmos.esa.int/gaia), processed by the *Gaia* Data Processing and Analysis Consortium (DPAC, https://www.cosmos.esa.int/web/gaia/dpac/consortium). Funding for the DPAC has been provided by national institutions, in particular the institutions participating in the *Gaia* Multilateral Agreement.

The Submillimeter Array is a joint project between the Smithsonian Astrophysical Observatory and the Academia Sinica Institute of Astronomy and Astrophysics and is funded by the Smithsonian Institution and the Academia Sinica.

Appendix A

ALMA proposal for observations of the inner disk

Abstract The conditions in protoplanetary disks surrounding young stellar objects affect the formation of planetesimals, as well as the dynamics of protoplanets, with the exact positions of condensation lines being crucial. However, spatially resolved observations of dust in the terrestrial planet forming region are scarce, leaving the models of formation poorly constrained. With the new observing capabilities, it will be possible for ALMA to probe 1-au-scale structures of Ophiuchus disks.

In order to understand DoAr44, a water-rich pre-transitional disk, we have constructed its global radiative transfer model, based on VLT spectra, VLTI interferometry and previous ALMA measurements (at >5 au resolution).

A dusty inner disk (1-10 au), whose presence is known from the SED, remains unresolved in the lower frequency observations though. We thus propose a long baseline Band 10 observation (C9 and C6) to measure the inner disk density and temperature profiles. This will allow us to determine the radii of condensation fronts, notably of water ice, and possible density inversions, which are crucial for the convergent migration of protoplanets - the likely mechanism explaining our own solar system.

RMS and Sensitivity justification This is a continuum observation focusing on dust structures, and using the 15 GHz bandwidth allows for the highest sensitivity. The RMS value of 0.5 mJy is based on our science requirement. Mapping the surface temperature with 10 K precision will allow us to decide between different condensation fronts, without the necessity of a spectral line observation. The peak flux density is derived from our radiative transfer models of the water-ice condensation line.

As we are primarily interested in the radial profile, the SNR at the weakest source (the water-ice line) will be better than 12, as we can de-project the ring and average in the azimuthal direction. After this averaging, the SNR will be 100, and the precision of the radial coordinate will be better than sub-au.

Justify chosen angular resolution The requested angular resolution is directly related to the expected structure of the source: the morphology expected in the inner region can be compared to the 1 au structures seen in the ALMA observation of the much closer disk HL Tauri. Current measurements of DoAr44 can only provide an insight on the integrated flux from the inner disk and a half-flux radius of about 3 au. To localize this emission, we must

observe at least at 1 au resolution, corresponding to 9 mas. This forces us to use the extended C-9 configuration.

If however a weaker more distant ring is present, extending up to the 8-10 au region, it will be necessary to constrain its diameter. This forced us to request time also in the C-6 configuration, to extend the largest recoverable scale to 140 mas.

Justify chosen correlator setttings We are using the recommended dual polarization single continuum mode in Band 10, using the full 1875 MHz spectral windows, with 90-degree Walsh switching, to obtain the full combined 15 GHz bandwidth.

1 Scientific justification

Protoplanetary disks are reservoirs of gas and dust surrounding young stellar objects, and the birthplace of planets. Understanding their evolution is necessary to understand the formation of exoplanetary systems and our own solar system. Various disk morphologies have been modeled based on their broad band spectral energy distribution [1], and later directly imaged either via mm-observations or adaptive optics imagers [2, 3]. Presumably, the youngest of these disks have a monotonously decreasing density profile, with a large inner cavity opening later, most probably due to the influence of forming ice-giants, creating so-called transitional disks [4], before completely dispersing a few millions of years later [5]. Matter is still flowing through this cavity, as evidenced by the large accretion rates [4].

An intermediary phase has been identified [6], called the pre-transitional phase, where the young star is surrounded by a dusty inner disk, encircled by a large, optically thin cavity, followed by an extended dust ring exhibiting mm-emission.

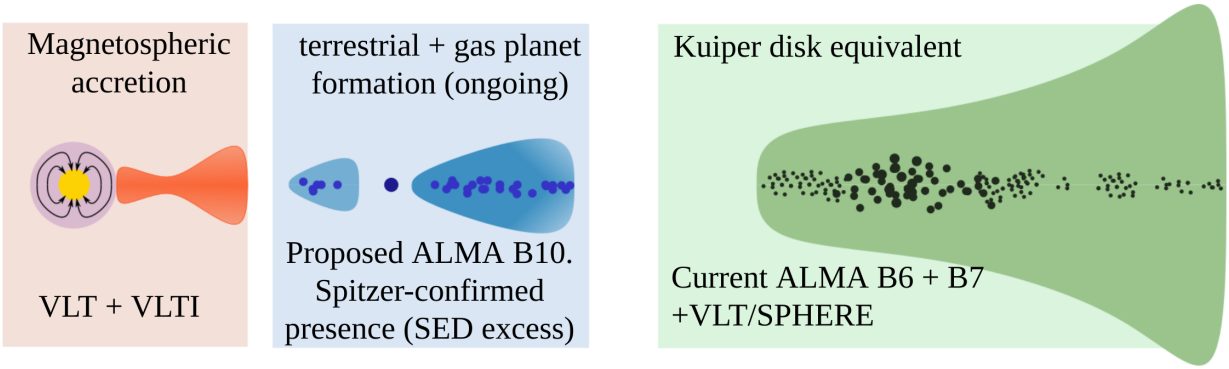

Figure 1: *A Schematic diagram of the DoAr44 system. The inner-most accretion region has been studied extensively, where our radiative transfer models are constrained by visible and NIR spectra. The outer "Kuiper belt" region has been probed by ALMA and VLT/SPHERE. It is separated from the inner disk by a vast gap, most likely cleared by ice giants.*

The object **DoAr44** (Haro 1–16), located in the Ophiuchus star formation region, is one of the pre-transitional disks with the **highest water vapour content** in the inner disk [7], two orders of magnitude more than the structurally very similar disk PDS 70 [8], where planet formation is confirmed by direct imaging by the Hubble Space Telescope (HST) [9], ALMA [10] and VLT/SPHERE [11]. DoAr44 has been investigated both via VLTI/GRAVITY [12], revealing a disk like structure in the 0.2–1.5 au region, VLT/SPHERE [13], showing the disk beyond 15 au, and ALMA Bands 3, 4, 6, 7 and 8 at resolutions up to ≈ 25 mas in Band 6 and 7 [16, 25], in both continuum and spectral lines, investigating the region from 5–80 au, revealing a thin dust ring with a brim around 47 au – see Fig.1.

To understand this unique object, we have constructed a 3D LTE radiative transfer model in `pyshellspec` [14, 15], describing both the star and an inner most magnetospheric accretion region (explaining the observed VLT/X-shooter and UVES Hα line profiles and the GRAVITY visibilities) and the outer region around 50 au, constrained by the ALMA observations. To match the observed broad-band SED and Spitzer/IRS spectra, spanning the range 5 – 30 µm (Fig. 2), it is necessary to introduce dust emission to the terrestrial planet forming region, extending from about 1 au to at most 10 au. The presence of an inner disk was already noted in the ODISEA long baseline observations in Band 6 at 5 au resolution [16], where it remained unresolved. However, based on our radiative transfer model, the region where the bulk of the sub-mm flux is emitted cannot be too compact, as this would be in conflict with infrared fluxes from Herschel/PACS, IRAS, AKARI, Spitzer/MIPS,

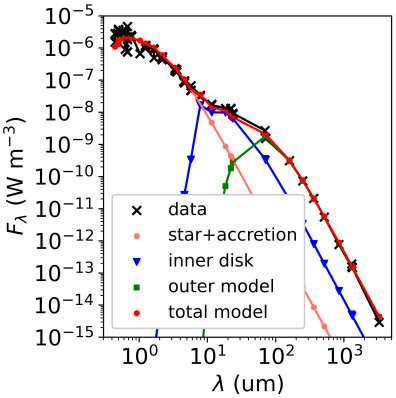

Figure 2: *A large contribution to the SED (right, in blue) from the inner disk (1 – 10 au) is known from various IR missions, but it has never been resolved. There exist many different temperature and density profiles of the inner disk consistent with the SED measurements, which may or may not include density inversion and dust traps, or gaps caused by planet formation. This region was the most relevant for the evolution of our own solar system, as Jupiter might have formed at the water ice-line, as proposed by the Grand Tack Model. [24]*

Spitzer/IRAC and fluxes from the W2 and W3 WISE surveys.

We thus propose a spatially resolved continuum observation of the terrestrial and giant planet forming region of this water-rich disk, to image the condensation lines of minerals condensing in the temperature range 110–700 K. These minerals include ammonia hydrate ($\sim$ 130 K), water (150–170 K), magnetite ($\sim$ 370 K) one of the main minerals observed in returned samples from Ryugu [17,18]. Furthermore, features at 9.4 µm and 11.3 µm from Spitzer/IRS spectra correspond to crystalline dust of the most common silicates, forsterite and enstatite, similar to the bulk of the silicates in the solar system terrestrial planets. Other minerals that condense in this region include graphite (C) and troilite (FeS) — a mineral rare on Earth's surface but common in meteorites.

In addition to these mineralogical question, these observations would allow us to test one of the predictions of the theory of **convergent migration** of protoplanets [19] – see Fig. 3. Radiation-hydrodynamical models have shown that in order to recreate the architecture of the inner solar system, with a small separation of Venus and Earth, and small sizes of Mercury and Mars, it is necessary to have an *inverted* density profile in the inner disk. Currently, it is one of the leading/competing theories for planet formation [20, 21] that for example explains the **origins of water in the terrestrial planet region** as a by-product of the formation of the ice-giants beyond the water snow-line [22]. The analogy of observed disks with our early solar system is challenging, as most observed exoplanetary systems have very different architectures. However, this is most likely due to strong observational biases, and only more reason to study the handful of observable pre-transitional disks. Our science questions include:

SQ1: What are the radii of the condensation lines of common minerals? Where is the water ice line located?
SQ2: Is there a density or temperature profile inversion in the inner 1–10 au disk?
SQ3: What are the highest/lowest temperatures attained in the formation region around 1 – 2 au?

These questions cannot be answered from disk-integrated-flux observations, as there is a degeneracy between the area of the contributing dust ring and its temperature. Based on our radiative transfer models and our chemical calculations of the condensation lines, we have delineated the following science requirements.

SR1: Observing the 1–10 au region with $\sim$1 au resolution, recovering angular radii up to 10 au.
SR2: Obtaining temperature profile with at most 10 K uncertainty.
SR3: If a ring of water ice is present at the ice-line and is optically thick, being able to detect it.

Observing at a worse resolution (2 – 3 au) would **not** be sufficient, as this would hide the water ice-line within one or two synthesized beams.

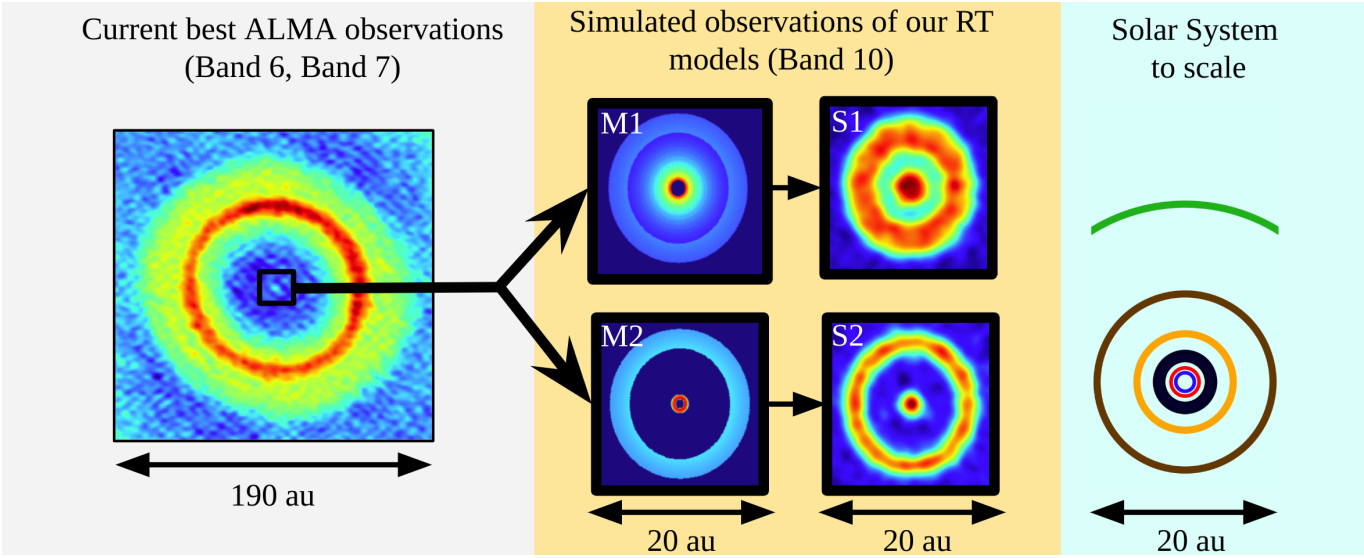

Figure 3: *Two possible models of the inner disk region of DoAr44 deliminating the two most extreme scenarios allowed by the SED. The left panel shows current best observations by [16]. The middle panels shows our RT models (M1, M2) and simulated observations (S1, S2) with the requested configurations.* ***M1*** *has a* **monotonous density profile**, *with the ring being caused by the added opacity of water ice.* ***M2*** *shows a hot region corresponding to the condensation line of silicates, and the water snow-line, with a* **density inversion** *in between them. The pressure drops due to the condensation, and this pressure minimum can accumulate dust, causing the density inversion.*

2 Description of observations

We request to observe the pre-transitional disk DoAr44 in Band 10. To answer our science questions, we require a single pointing in the C-9 and C-6 configurations. Such a configuration has been suggested by the ALMA Observing Tool, based on the following observational requirements, which were straight-forwardly derived from the science requirements:

OR1: The source shall be observed with an angular resolution of 9 milli-arcseconds.
OR2: The sensitivity shall be at least 0.5 mJy per synthesised beam.
OR3: The weakest detectable source component shall have at most 6 mJy per synthesised beam.

The OT estimates 42 minutes of on-source time in both configurations, resulting in a **total of 3.8 h with all overheads,** split between the two configurations, which is within the expected available times for Band 10.

Why DoAr44 Due to short dissipation timescales, DoAr44 might be **one of the only pre-transitional disks we will be able to image at the 1 au scale**, providing an important constraint for planet formation theories, including the convergent migration. It is also a **unique laboratory to directly observe condensation fronts** of minerals that form the bulk of our own interplanetary surroundings. It also has a **large observational dataset**, allowing the proposed Band 10 observations to determine the condensation front temperatures **without unnecessary assumptions** on the inner and outer disk, as their temperature profiles are tightly constrained. From Spitzer [1], it is known that DoAr44 contains **vast amounts of water vapour**, making it the perfect target to investigate the water ice-line, **the most important condensation line** for our own solar system. Due to its location in Ophiuchus, DoAr44 has great observability from the ALMA site, allowing for **flexible scheduling** and observations at high altitudes, minimizing atmospheric effects. This is specially important, as this is a Band 10 observation, requiring PWV less than 0.65 mm.

Why ALMA High-frequency observations on long baselines, as offered for the first time by ALMA in Cycle 11, will allow us for the first time to peer into the most interesting region of planet formation. To probe the dust distribution, it is necessary to perform a mm or sub-mm observation. Other arrays simply do not reach the required angular resolution — the SMA's smallest beam is 250 mas, 25 times larger than requested by this proposal. NOEMA also does not approach these angular scales, and southern Ophiuchus cannot be easily observed from the Plateau de Bure. JWST and ELT/METIS observations would be useful, but would reach the mid-plane dust, due to the optical thickness [23].

Why Band 10 To achieve the 1 au resolution needed to distinguish the condensation fronts, it is necessary to observe with ALMA at Band 10. This also means that the data from the ongoing Band 10 survey in Ophiuchus (2023.1.00131.S) will not be nearly sufficient, as it will be performed with 30 au resolution. For the first time, the new capabilities of ALMA in Cycle 11 allow us to peer into the inner regions of Ophiuchus disks, allowing us to constrain their temperature and density profiles. We plan to perform a continuum observation, taking advantage of the full 15 GHz DSB bandwidth offered in Band 10. The weather constrains (< 0.65 mm PWV) are essentially the same in Band 9, and with a Band 10 observation we can achieve larger angular resolution.

Why C-9 and C-6 Condensation at a given pressure occurs at a well defined temperature, and thus opacity increases rapidly in a small radial range. To differentiate between the condensation lines of various chemical species, we are forced to propose for the C-9 configuration. However, based on our radiative transfer models and our chemical calculations of the condensation sequence, the radii of these condensation lines might extend up to ~ 10 au, which is above the largest recoverable scale of C-9 in Band 10. For this reason, it is necessary to supplement the observations using the C-6 configuration in Band 10. As we are interested in the radial distributions of temperature and surface density, any possible temporal variability between the two observations will not impact the results.

Analysis plan Our group has already constructed various radiative transfer models in `pyshellspec` [14], a universal radiative transfer tool used for modelling interferometric visibilities (from ALMA, VLTI, CHARA, NPOI, ...), spectral line profiles and broad-band SEDs, lightcurves and other observables. Among many other features, our models take into account the precise mineral composition, evaporation temperatures and grain size distribution, making them capable to answer the key questions above given the Band 10 observations.

3 References

[1] Dullemond, C. P. et al. 2007, in Protostars and Planets V (University of Arizona Press), 555 [2], Andrews, S. M. et al. 2018, ApJ, 869, L41 [3], Avenhaus, H. et al. 2018, ApJ, 863, 44 [4], van der Marel, N. et al. 2023, Eur. Phys. J. Plus, 138, 225 [5] Li, M.& Xiao, L. 2016, ApJ, 820, 36 [6] Espaillat, C. et al. 2010, ApJ, 717, 441 [7] Salyk, C. et al. 2015, ApJL, 810(2), L24 [8] Perotti, G. et al. 2023, Nature, 620, 516–520 [9] Zhou, Y. et al. 2021, AJ, 161, 244 [10] Benisty, M. et al. 2021, ApJL, 916(1), L2 [11] Keppler, M. et al. 2018, A&A, 617, A44 [12] Bouvier, J. et al. 2020, A&A, 636, A108 [13] Arce-Tord, C. et al. 2023, MNRAS, 526(2), 2077-2085 [14] Brož, M. et al. 2021, A&A, 645, A51 [15] Mourard, D. et al. 2018, A&A, 618, A112 [16] Cieza, L. A. et al. 2021, MNRAS, 501, 2934-2953 [17] McCain, K. A. et al. 2023, Nat. Astron., 7(3), 309-317 [18] Dobrică, E. et al. 2023, GCA, 346, 65-75 [19] Brož, M. et al. 2021, Nat. Astron., 5, 898-902 [20] Izidoro, A. et al. 2017, MNRAS, 470(2), 1750-1770 [21] Johansen, A. et al. 2021, Sci. Adv., 7(8), eabc0444 [22] Raymond, S. N. et al. 2017, Icarus, 297, 134-148 [23] Oberg, N. et al. 2023, A&A, 670, A74 [24] Walsh, K. et al. 2011, Nature, 475, 206–209 [25] Arce-Tord, C. et al. 2023, MNRAS, 526, 2077

Bibliography

P. Andre, D. Ward-Thompson, and M. Barsony. Submillimeter Continuum Observations of rho Ophiuchi A: The Candidate Protostar VLA 1623 and Prestellar Clumps. *ApJ* , 406:122, Mar. 1993. doi: 10.1086/172425.

S. M. Andrews and J. P. Williams. A submillimeter view of circumstellar dust disks in ρ ophiuchi. *The Astrophysical Journal*, 671(2):1800, 2007.

S. M. Andrews, D. J. Wilner, A. M. Hughes, C. Qi, and C. P. Dullemond. Protoplanetary Disk Structures in Ophiuchus. II. Extension to Fainter Sources. *ApJ* , 723(2):1241–1254, Nov. 2010. doi: 10.1088/0004-637X/723/2/1241.

S. M. Andrews, D. J. Wilner, C. Espaillat, A. M. Hughes, C. P. Dullemond, M. K. McClure, C. Qi, and J. M. Brown. Resolved Images of Large Cavities in Protoplanetary Transition Disks. *ApJ* , 732(1):42, May 2011. doi: 10.1088/0004-637X/732/1/42.

S. M. Andrews, J. Huang, L. M. Pérez, A. Isella, C. P. Dullemond, N. T. Kurtovic, V. V. Guzmán, J. M. Carpenter, D. J. Wilner, S. Zhang, et al. The disk substructures at high angular resolution project (dsharp). i. motivation, sample, calibration, and overview. *The Astrophysical Journal Letters*, 869(2):L41, 2018.

C. Arce-Tord, S. Casassus, W. R. Dent, S. Pérez, M. Cárcamo, P. Weber, N. Engler, L. A. Cieza, A. Hales, A. Zurlo, et al. Radio-continuum decrements associated to shadowing from the central warp in transition disc doar 44. *Monthly Notices of the Royal Astronomical Society*, 526(2):2077–2085, 2023.

P. J. Armitage. *Astrophysics of planet formation*. Cambridge University Press, 2020.

H. Avenhaus, S. P. Quanz, A. Garufi, S. Perez, S. Casassus, C. Pinte, G. H. M. Bertrang, C. Caceres, M. Benisty, and C. Dominik. Disks around T Tauri Stars with SPHERE (DARTTS-S). I. SPHERE/IRDIS Polarimetric Imaging of Eight Prominent T Tauri Disks. *ApJ* , 863(1): 44, Aug. 2018. doi: 10.3847/1538-4357/aab846.

M. Barsony. Class 0 Protostars. In D. P. Clemens and R. Barvainis, editors, *Clouds, Cores, and Low Mass Stars*, volume 65 of *Astronomical Society of the Pacific Conference Series*, page 197, Jan. 1994.

B. Bean, S. Bhatnagar, S. Castro, J. D. Meyer, B. Emonts, E. Garcia, R. Garwood, K. Golap, J. G. Villalba, P. Harris, et al. Casa, the common astronomy software applications for radio astronomy. *Publications of the Astronomical Society of the Pacific*, 134(1041):114501, 2022.

S. V. W. Beckwith, A. I. Sargent, R. S. Chini, and R. Guesten. A Survey for Circumstellar Disks around Young Stellar Objects. *AJ* , 99:924, Mar. 1990. doi: 10.1086/115385.

M. Bessell, G. Bloxham, B. Schmidt, S. Keller, P. Tisserand, and P. Francis. SkyMapper Filter Set: Design and Fabrication of Large-Scale Optical Filters. *PASP* , 123(905):789, July 2011. doi: 10.1086/660849.

N. Bessolaz, C. Zanni, J. Ferreira, R. Keppens, and J. Bouvier. Accretion funnels onto weakly magnetized young stars. *Astronomy & Astrophysics*, 478(1):155–162, 2008.

N. Billot, P. Agnèse, J.-L. Auguères, A. Béguin, A. Bouère, O. Boulade, C. Cara, C. Cloué, E. Doumayrou, L. Duband, et al. The herschel/pacs 2560 bolometers imaging camera. In *Space Telescopes and Instrumentation I: Optical, Infrared, and Millimeter*, volume 6265, pages 81–92. SPIE, 2006.

J. Bolton and G. Stanley. Variable source of radio frequency radiation in the constellation of cygnus. *Nature*, 161(4087):312–313, 1948.

J. Bouvier, S. Alencar, T. Harries, C. Johns-Krull, and M. Romanova. Magnetospheric accretion in classical t tauri stars. *arXiv preprint astro-ph/0603498*, 2006.

J. Bouvier, E. Alecian, S. H. P. Alencar, A. Sousa, J.-F. Donati, K. Perraut, A. Bayo, L. M. Rebull, C. Dougados, G. Duvert, et al. Investigating the magnetospheric accretion process in the young pre-transitional disk system doar 44 (v2062 oph)-a multiwavelength interferometric, spectropolarimetric, and photometric observing campaign. *Astronomy & Astrophysics*, 643:A99, 2020a.

J. Bouvier, K. Perraut, J.-B. Le Bouquin, G. Duvert, C. Dougados, W. Brandner, M. Benisty, J.-P. Berger, and E. Alécian. Probing the magnetospheric accretion region of the young pre-transitional disk system doar 44 using vlti/gravity. *Astronomy & Astrophysics*, 636:A108, 2020b.

J. M. Brown, G. A. Blake, C. Qi, C. P. Dullemond, D. J. Wilner, and J. P. Williams. Evidence for Dust Clearing Through Resolved Submillimeter Imaging. *ApJ* , 704(1):496–502, Oct. 2009. doi: 10.1088/0004-637X/704/1/496.

M. Brož, D. Mourard, Budaj, J., Harmanec, P., Schmitt, H., Tallon-Bosc, I., Bonneau, D., Bozi´c, H., Gies, D., and Slechta, M. Optically thin circumstellar medium in the a system. *A&A*, 645:A51, 2021. doi: 10.1051/0004-6361/202039035. URL https://doi.org/10.1051/0004-6361/202039035.

J. Budaj and M. T. Richards. A description of the shellspec code. *Contributions of the Astronomical Observatory Skalnate Pleso*, 34(3):167–196, Oct. 2004.

J. Budaj, M. Kocifaj, R. Salmeron, and I. Hubený. Tables of phase functions, opacities, albedos, equilibrium temperatures, and radiative accelerations of dust grains in exoplanets. *Monthly Notices of the Royal Astronomical Society*, 454(1):2–27, 2015.

S. Casassus, H. Avenhaus, S. Pérez, V. Navarro, M. Cárcamo, S. Marino, L. Cieza, S. P. Quanz, F. Alarcón, A. Zurlo, et al. An inner warp in the doar 44 t tauri transition disc. *Monthly Notices of the Royal Astronomical Society*, 477(4):5104–5114, 2018.

D. Chalmers, F. Daruich, B. Hoff, and C. Jara. 66 antennas, up to 16km baselines, 5000m elevation, 28 km from support: the coming challenge of ALMA Observatory antenna group

operations and maintenance. In A. B. Peck, R. L. Seaman, and F. Comeron, editors, *Observatory Operations: Strategies, Processes, and Systems IV*, volume 8448, page 844817. International Society for Optics and Photonics, SPIE, 2012. doi: 10.1117/12.927048. URL https://doi.org/10.1117/12.927048.

E. Chiang and G. Laughlin. The minimum-mass extrasolar nebula: in situ formation of close-in super-Earths. *Monthly Notices of the Royal Astronomical Society*, 431(4):3444–3455, 04 2013. ISSN 0035-8711. doi: 10.1093/mnras/stt424. URL https://doi.org/10.1093/mnras/stt424.

L. A. Cieza, D. Ruíz-Rodríguez, A. Hales, S. Casassus, S. Pérez, C. Gonzalez-Ruilova, H. Cánovas, J. P. Williams, A. Zurlo, M. Ansdell, H. Avenhaus, A. Bayo, G. H. M. Bertrang, V. Christiaens, W. Dent, G. Ferrero, R. Gamen, J. Olofsson, S. Orcajo, K. Peña Ramírez, D. Principe, M. R. Schreiber, and G. van der Plas. The Ophiuchus DIsc Survey Employing ALMA (ODISEA) - I: project description and continuum images at 28 au resolution. *MNRAS* , 482(1):698–714, Jan. 2019. doi: 10.1093/mnras/sty2653.

L. A. Cieza, C. González-Ruilova, A. S. Hales, P. Pinilla, D. Ruíz-Rodríguez, A. Zurlo, S. Casassus, S. Pérez, H. Cánovas, C. Arce-Tord, et al. The ophiuchus disc survey employing alma (odisea)–iii. the evolution of substructures in massive discs at 3–5 au resolution. *Monthly Notices of the Royal Astronomical Society*, 501(2):2934–2953, 2021.

A. Comrie, K.-S. Wang, S.-C. Hsu, A. Moraghan, P. Harris, Q. Pang, A. Pińska, C.-C. Chiang, R. Simmonds, T.-H. Chang, et al. Carta: Cube analysis and rendering tool for astronomy. *Astrophysics Source Code Library*, pages ascl–2103, 2021.

A. Cook, D. Whittet, S. Shenoy, P. Gerakines, D. White, and J. Chiar. The thermal evolution of ices in the environments of newly formed stars: The co2 diagnostic. *The Astrophysical Journal*, 730(2):124, 2011.

R. Cutri, M. Skrutskie, S. Van Dyk, C. Beichman, J. Carpenter, T. Chester, L. Cambresy, T. Evans, J. Fowler, J. Gizis, et al. Vizier online data catalog: 2mass all-sky catalog of point sources (cutri+ 2003). *VizieR online data catalog*, pages II–246, 2003.

P. De Laverny, A. Recio-Blanco, C. Worley, and B. Plez. The ambre project: A new synthetic grid of high-resolution fgkm stellar spectra. *Astronomy & Astrophysics*, 544:A126, 2012.

N. Delmotte, M. Dolensky, P. Padovani, J. Retzlaff, C. Rité, P. Rosati, R. Slijkhuis, A. Wicenec, P. Fernique, and A. Micol. Eso science archive interfaces. In *Astronomical Data Analysis Software and Systems XV*, volume 351, page 690, 2006.

T. Do-Duy, C. M. Wright, T. Fujiyoshi, A. Glasse, R. Siebenmorgen, R. Smith, B. Stecklum, and M. Sterzik. Crystalline silicate absorption at 11.1 um: ubiquitous and abundant in embedded YSOs and the interstellar medium. *Monthly Notices of the Royal Astronomical Society*, 493(3):4463–4517, 02 2020. ISSN 0035-8711. doi: 10.1093/mnras/staa396. URL https://doi.org/10.1093/mnras/staa396.

S. E. Dodson-Robinson and C. Salyk. Transitional disks as signposts of young, multiplanet systems. *The Astrophysical Journal*, 738(2):131, aug 2011. doi: 10.1088/0004-637X/738/2/131. URL https://dx.doi.org/10.1088/0004-637X/738/2/131.

M. V. Dolidze and M. A. Arakelyan. The T-Association Near ρ Ophiuchi. *Soviet Ast.* , 3:434, June 1959.

B. T. Draine. On the Submillimeter Opacity of Protoplanetary Disks. *ApJ* , 636(2):1114–1120, Jan. 2006. doi: 10.1086/498130.

C. Dullemond, A. Juhasz, A. Pohl, F. Sereshti, R. Shetty, T. Peters, B. Commercon, and M. Flock. Radmc-3d: A multi-purpose radiative transfer tool. *Astrophysics Source Code Library*, pages ascl–1202, 2012.

C. Espaillat, N. Calvet, P. D'Alessio, J. Hernández, C. Qi, L. Hartmann, E. Furlan, and D. M. Watson. On the Diversity of the Taurus Transitional Disks: UX Tauri A and LkCa 15. *ApJ* , 670(2):L135–L138, Dec. 2007. doi: 10.1086/524360.

C. Espaillat, P. D'Alessio, J. Hernández, E. Nagel, K. Luhman, D. Watson, N. Calvet, J. Muzerolle, and M. McClure. Unveiling the structure of pre-transitional disks. *The Astrophysical Journal*, 717(1):441, 2010.

G. Fazio, J. Hora, L. Allen, M. Ashby, P. Barmby, L. Deutsch, J.-S. Huang, S. Kleiner, M. Marengo, S. Megeath, et al. The infrared array camera (irac) for the spitzer space telescope. *The Astrophysical Journal Supplement Series*, 154(1):10, 2004.

D. Foreman-Mackey, D. W. Hogg, D. Lang, and J. Goodman. emcee: the mcmc hammer. *Publications of the Astronomical Society of the Pacific*, 125(925):306, 2013.

W. Freudling, M. Romaniello, D. Bramich, P. Ballester, V. Forchi, C. García-Dabló, S. Moehler, and M. Neeser. Automated data reduction workflows for astronomy-the eso reflex environment. *Astronomy & Astrophysics*, 559:A96, 2013.

Gaia Collaboration. Vizier online data catalog: Gaia dr2 (gaia collaboration, 2018). *VizieR Online Data Catalog*, pages I–345, 2018.

Gaia Collaboration. VizieR Online Data Catalog: Gaia EDR3 (Gaia Collaboration, 2020). *VizieR Online Data Catalog*, art. I/350, Nov. 2020. doi: 10.26093/cds/vizier.1350.

R. Giacconi, G. Branduardi, U. Briel, A. Epstein, D. Fabricant, E. Feigelson, W. Forman, P. Gorenstein, J. Grindlay, H. Gursky, F. R. Harnden, J. P. Henry, C. Jones, E. Kellogg, D. Koch, S. Murray, E. Schreier, F. Seward, H. Tananbaum, K. Topka, L. Van Speybroeck, S. S. Holt, R. H. Becker, E. A. Boldt, P. J. Serlemitsos, G. Clark, C. Canizares, T. Markert, R. Novick, D. Helfand, and K. Long. The Einstein (HEAO 2) X-ray Observatory. *ApJ* , 230: 540–550, June 1979. doi: 10.1086/157110.

D. R. Gies, W. P. McKibben, P. W. Kelton, C. B. Opal, and S. Sawyer. Time-resolved h-alpha spectroscopy of the be star pleione during a lunar occultation. *Astronomical Journal (ISSN 0004-6256), vol. 100, Nov. 1990, p. 1601-1609.*, 100:1601–1609, 1990.

C. Ginski, S. Facchini, J. Huang, M. Benisty, D. Vaendel, L. Stapper, C. Dominik, J. Bae, F. Ménard, G. Muro-Arena, M. R. Hogerheijde, M. McClure, R. G. van Holstein, T. Birnstiel, Y. Boehler, A. Bohn, M. Flock, E. E. Mamajek, C. F. Manara, P. Pinilla, C. Pinte, and Álvaro Ribas. Disk evolution study through imaging of nearby young stars (destinys): Late infall causing disk misalignment and dynamic structures in su aur*. *The Astrophysical Journal*

Letters, 908(2):L25, feb 2021. doi: 10.3847/2041-8213/abdf57. URL https://dx.doi.org/10.3847/2041-8213/abdf57.

GRAVITY Collaboration, R. Abuter, M. Accardo, A. Amorim, N. Anugu, G. Ávila, N. Azouaoui, M. Benisty, J. P. Berger, N. Blind, H. Bonnet, P. Bourget, W. Brandner, R. Brast, A. Buron, L. Burtscher, F. Cassaing, F. Chapron, É. Choquet, Y. Clénet, C. Collin, V. Coudé Du Foresto, W. de Wit, P. T. de Zeeuw, C. Deen, F. Delplancke-Ströbele, R. Dembet, F. Derie, J. Dexter, G. Duvert, M. Ebert, A. Eckart, F. Eisenhauer, M. Esselborn, P. Fédou, G. Finger, P. Garcia, C. E. Garcia Dabo, R. Garcia Lopez, E. Gendron, R. Genzel, S. Gillessen, F. Gonte, P. Gordo, M. Grould, U. Grözinger, S. Guieu, P. Haguenauer, O. Hans, X. Haubois, M. Haug, F. Haussmann, T. Henning, S. Hippler, M. Horrobin, A. Huber, Z. Hubert, N. Hubin, C. A. Hummel, G. Jakob, A. Janssen, L. Jochum, L. Jocou, A. Kaufer, S. Kellner, S. Kendrew, L. Kern, P. Kervella, M. Kiekebusch, R. Klein, Y. Kok, J. Kolb, M. Kulas, S. Lacour, V. Lapeyrère, B. Lazareff, J. B. Le Bouquin, P. Lèna, R. Lenzen, S. Lévêque, M. Lippa, Y. Magnard, L. Mehrgan, M. Mellein, A. Mérand, J. Moreno-Ventas, T. Moulin, E. Müller, F. Müller, U. Neumann, S. Oberti, T. Ott, L. Pallanca, J. Panduro, L. Pasquini, T. Paumard, I. Percheron, K. Perraut, G. Perrin, A. Pflüger, O. Pfuhl, T. Phan Duc, P. M. Plewa, D. Popovic, S. Rabien, A. Ramírez, J. Ramos, C. Rau, M. Riquelme, R. R. Rohloff, G. Rousset, J. Sanchez-Bermudez, S. Scheithauer, M. Schöller, N. Schuhler, J. Spyromilio, C. Straubmeier, E. Sturm, M. Suarez, K. R. W. Tristram, N. Ventura, F. Vincent, I. Waisberg, I. Wank, J. Weber, E. Wieprecht, M. Wiest, E. Wiezorrek, M. Wittkowski, J. Woillez, B. Wolff, S. Yazici, D. Ziegler, and G. Zins. First light for GRAVITY: Phase referencing optical interferometry for the Very Large Telescope Interferometer. *A&A* , 602: A94, June 2017. doi: 10.1051/0004-6361/201730838.

J. M. Greenberg. Making a comet nucleus. *A&A* , 330:375–380, Feb. 1998.

M. J. Griffin, A. Abergel, A. Abreu, P. A. Ade, P. André, J.-L. Augueres, T. Babbedge, Y. Bae, T. Baillie, J.-P. Baluteau, et al. The herschel-spire instrument and its in-flight performance. *Astronomy & Astrophysics*, 518:L3, 2010.

S. Haffert, A. Bohn, J. De Boer, I. Snellen, J. Brinchmann, J. Girard, C. Keller, and R. Bacon. Two accreting protoplanets around the young star pds 70. *Nature Astronomy*, 3(8):749–754, 2019.

G. Haro. Faint spectra showing H_α in emission in the obscuring clouds of Ophiuchus and Scorpius and in a region in Sagittarius. *AJ* , 54:188–189, Sept. 1949. doi: 10.1086/106257.

C. Hayashi. Stellar evolution in early phases of gravitational contraction. *PASJ* , 13:450–452, Jan. 1961.

C. Hayashi. Structure of the Solar Nebula, Growth and Decay of Magnetic Fields and Effects of Magnetic and Turbulent Viscosities on the Nebula. *Progress of Theoretical Physics Supplement*, 70:35–53, 01 1981. ISSN 0375-9687. doi: 10.1143/PTPS.70.35. URL https://doi.org/10.1143/PTPS.70.35.

A. A. Henden, M. Templeton, D. Terrell, T. C. Smith, S. Levine, and D. Welch. VizieR Online Data Catalog: AAVSO Photometric All Sky Survey (APASS) DR9 (Henden+, 2016). art. II/336, Jan. 2016.

G. H. Herbig. The spectra of be-and ae-type stars associated with nebulosity. *The Astrophysical Journal Supplement Series*, 4:337, 1960.

P. C. Hewett, S. J. Warren, S. K. Leggett, and S. T. Hodgkin. The UKIRT Infrared Deep Sky Survey ZY JHK photometric system: passbands and synthetic colours. *MNRAS* , 367(2): 454–468, Apr. 2006. doi: 10.1111/j.1365-2966.2005.09969.x.

J. R. Hind. Note on the Variable Nebula in Taurus. *MNRAS* , 24:65, Jan. 1864.

J. A. Högbom. Aperture Synthesis with a Non-Regular Distribution of Interferometer Baselines. *A&AS* , 15:417, June 1974.

A. M. Hughes, S. M. Andrews, C. Espaillat, D. J. Wilner, N. Calvet, P. D'Alessio, C. Qi, J. P. Williams, and M. R. Hogerheijde. A Spatially Resolved Inner Hole in the Disk Around GM Aurigae. *ApJ* , 698(1):131–142, June 2009. doi: 10.1088/0004-637X/698/1/131.

T.-O. Husser, S. Wende-von Berg, S. Dreizler, D. Homeier, A. Reiners, T. Barman, and P. H. Hauschildt. A new extensive library of phoenix stellar atmospheres and synthetic spectra. *Astronomy & Astrophysics*, 553:A6, 2013.

S. Iguchi, K.-I. Morita, M. Sugimoto, B. V. Vilaró, M. Saito, T. Hasegawa, R. Kawabe, K. Tatematsu, S. Sakamoto, H. Kiuchi, S. K. Okumura, G. Kosugi, J. Inatani, S. Takakuwa, D. Iono, T. Kamazaki, R. Ogasawara, and M. Ishiguro. The Atacama Compact Array (ACA). *PASJ* , 61(1):1–12, Feb. 2009. doi: 10.1093/pasj/61.1.1.

A. Isella, J. M. Carpenter, and A. I. Sargent. Structure and evolution of pre-main-sequence circumstellar disks. *The Astrophysical Journal*, 701(1):260, 2009.

T. Jayasinghe, C. Kochanek, K. Stanek, B. Shappee, T. W. Holoien, T. A. Thompson, J. Prieto, S. Dong, M. Pawlak, J. Shields, et al. The asas-sn catalogue of variable stars i: The serendipitous survey. *Monthly Notices of the Royal Astronomical Society*, 477(3):3145–3163, 2018.

J. H. Jeans. I. the stability of a spherical nebula. *Philosophical Transactions of the Royal Society of London. Series A, Containing Papers of a Mathematical or Physical Character*, 199(312-320):1–53, 1902.

H. L. Johnson and R. I. Mitchell. A Completely Digitized Multi-Color Photometer. *Communications of the Lunar and Planetary Laboratory*, 1:73–82, Jan. 1962.

A. H. Joy. No. 709. T Tauri variable stars. *Contributions from the Mount Wilson Observatory / Carnegie Institution of Washington*, 709:1–28, Jan. 1945.

N. Kaiser, H. Aussel, B. E. Burke, H. Boesgaard, K. Chambers, M. R. Chun, J. N. Heasley, K.-W. Hodapp, B. Hunt, R. Jedicke, et al. Pan-starrs: a large synoptic survey telescope array. In *Survey and Other Telescope Technologies and Discoveries*, volume 4836, pages 154–164. SPIE, 2002.

I. Kant. *Universal natural history and theory of the Heavens*. Newcomb Livraria Press, 2023, 1755.

F. Kemper, W. Vriend, and A. Tielens. The absence of crystalline silicates in the diffuse interstellar medium. *The Astrophysical Journal*, 609(2):826, 2004.

S. J. Kenyon and L. Hartmann. Spectral Energy Distributions of T Tauri Stars: Disk Flaring and Limits on Accretion. *ApJ* , 323:714, Dec. 1987. doi: 10.1086/165866.

M. Keppler, M. Benisty, A. Müller, T. Henning, R. van Boekel, F. Cantalloube, C. Ginski, R. G. van Holstein, A. L. Maire, A. Pohl, M. Samland, H. Avenhaus, J. L. Baudino, A. Boccaletti, J. de Boer, M. Bonnefoy, G. Chauvin, S. Desidera, M. Langlois, C. Lazzoni, G. D. Marleau, C. Mordasini, N. Pawellek, T. Stolker, A. Vigan, A. Zurlo, T. Birnstiel, W. Brandner, M. Feldt, M. Flock, J. Girard, R. Gratton, J. Hagelberg, A. Isella, M. Janson, A. Juhasz, J. Kemmer, Q. Kral, A. M. Lagrange, R. Launhardt, A. Matter, F. Ménard, J. Milli, P. Mollière, J. Olofsson, L. Pérez, P. Pinilla, C. Pinte, S. P. Quanz, T. Schmidt, S. Udry, Z. Wahhaj, J. P. Williams, E. Buenzli, M. Cudel, C. Dominik, R. Galicher, M. Kasper, J. Lannier, D. Mesa, D. Mouillet, S. Peretti, C. Perrot, G. Salter, E. Sissa, F. Wildi, L. Abe, J. Antichi, J. C. Augereau, A. Baruffolo, P. Baudoz, A. Bazzon, J. L. Beuzit, P. Blanchard, S. S. Brems, T. Buey, V. De Caprio, M. Carbillet, M. Carle, E. Cascone, A. Cheetham, R. Claudi, A. Costille, A. Delboulbé, K. Dohlen, D. Fantinel, P. Feautrier, T. Fusco, E. Giro, L. Gluck, C. Gry, N. Hubin, E. Hugot, M. Jaquet, D. Le Mignant, M. Llored, F. Madec, Y. Magnard, P. Martinez, D. Maurel, M. Meyer, O. Möller-Nilsson, T. Moulin, L. Mugnier, A. Origné, A. Pavlov, D. Perret, C. Petit, J. Pragt, P. Puget, P. Rabou, J. Ramos, F. Rigal, S. Rochat, R. Roelfsema, G. Rousset, A. Roux, B. Salasnich, J. F. Sauvage, A. Sevin, C. Soenke, E. Stadler, M. Suarez, M. Turatto, and L. Weber. Discovery of a planetary-mass companion within the gap of the transition disk around PDS 70. *A&A* , 617:A44, Sept. 2018. doi: 10.1051/0004-6361/201832957.

V. F. Ksoll, S. Reissl, R. S. Klessen, I. W. Stephens, R. J. Smith, J. D. Soler, A. Traficante, P. Girichidis, L. Testi, P. Hennebelle, et al. A deep-learning approach to the 3d reconstruction of dust density and temperature in star-forming regions. *Astronomy & Astrophysics*, 683: A246, 2024.

B. V. Kukarkin, P. N. Kholopov, Y. P. Pskovsky, Y. N. Efremov, N. P. Kukarkina, N. E. Kurochkin, and G. I. Medvedeva. The third edition containing information on 20437 variable stars discovered and designated till 1968. *General Catalogue of Variable Stars*, page 0, Jan. 1971.

R. Kurosawa, M. M. Romanova, and T. J. Harries. Multidimensional models of hydrogen and helium emission line profiles for classical t tauri stars: method, tests and examples. *Monthly Notices of the Royal Astronomical Society*, 416(4):2623–2639, 2011.

A. Labeyrie. Interference fringes obtained on Vega with two optical telescopes. *ApJ* , 196: L71–L75, Mar. 1975. doi: 10.1086/181747.

C. J. Lada. Star formation: From ob associations to protostars. *Symposium - International Astronomical Union*, 115:1–18, 1987. doi: 10.1017/S0074180900094766.

C. J. Lada and B. A. Wilking. The nature of the embedded population in the rho ophiuchi dark cloud-mid-infrared observations. *Astrophysical Journal, Part 1 (ISSN 0004-637X), vol. 287, Dec. 15, 1984, p. 610-621.*, 287:610–621, 1984.

A.-M. Lagrange, M. Bonnefoy, G. Chauvin, D. Apai, D. Ehrenreich, A. Boccaletti, D. Gratadour, D. Rouan, D. Mouillet, S. Lacour, and M. Kasper. A giant planet imaged in the disk of the young star β pictoris. *Science*, 329(5987):57–59, 2010. doi: 10.1126/science.1187187. URL https://www.science.org/doi/abs/10.1126/science.1187187.

T. Lanz and I. Hubený. A grid of non-lte line-blanketed model atmospheres of o-type stars. *The Astrophysical Journal Supplement Series*, 146(2):417, 2003.

T. Lanz and I. Hubený. A grid of nlte line-blanketed model atmospheres of early b-type stars. *The Astrophysical Journal Supplement Series*, 169(1):83, 2007.

P.-S. Laplace. *Pierre-Simon Laplace philosophical essay on probabilities: translated from the fifth french edition of 1825 with notes by the translator*, volume 13. Springer Science & Business Media. 2012, 1796.

B. M. Lasker, M. G. Lattanzi, B. J. McLean, B. Bucciarelli, R. Drimmel, J. Garcia, G. Greene, F. Guglielmetti, C. Hanley, G. Hawkins, et al. The second-generation guide star catalog: description and properties. *The Astronomical Journal*, 136(2):735, 2008.

A. Lawrence, S. J. Warren, O. Almaini, A. C. Edge, N. C. Hambly, R. F. Jameson, P. Lucas, M. Casali, A. Adamson, S. Dye, J. P. Emerson, S. Foucaud, P. Hewett, P. Hirst, S. T. Hodgkin, M. J. Irwin, N. Lodieu, R. G. McMahon, C. Simpson, I. Smail, D. Mortlock, and M. Folger. The UKIRT Infrared Deep Sky Survey (UKIDSS). *MNRAS* , 379(4):1599–1617, Aug. 2007. doi: 10.1111/j.1365-2966.2007.12040.x.

B. Lazareff, J. P. Berger, J. Kluska, J. B. Le Bouquin, M. Benisty, F. Malbet, C. Koen, C. Pinte, W. F. Thi, O. Absil, F. Baron, A. Delboulbé, G. Duvert, A. Isella, L. Jocou, A. Juhasz, S. Kraus, R. Lachaume, F. Ménard, R. Millan-Gabet, J. D. Monnier, T. Moulin, K. Perraut, S. Rochat, F. Soulez, M. Tallon, E. Thiébaut, W. Traub, and G. Zins. Structure of Herbig AeBe disks at the milliarcsecond scale . A statistical survey in the H band using PIONIER-VLTI. *A&A* , 599:A85, Mar. 2017. doi: 10.1051/0004-6361/201629305.

J.-B. Le Bouquin, J.-P. Berger, B. Lazareff, G. Zins, P. Haguenauer, L. Jocou, P. Kern, R. Millan-Gabet, W. Traub, O. Absil, et al. Pionier: a 4-telescope visitor instrument at vlti. *Astronomy & Astrophysics*, 535:A67, 2011.

C.-F. Lee, Z.-Y. Li, H. Shang, and N. Hirano. Magnetocentrifugal origin for protostellar jets validated through detection of radial flow at the jet base. *The Astrophysical Journal Letters*, 927(2):L27, mar 2022. doi: 10.3847/2041-8213/ac59c0. URL https://dx.doi.org/10.3847/2041-8213/ac59c0.

H. Leiendecker, H. Jang-Condell, N. J. Turner, and A. D. Myers. Dust rings and cavities in the protoplanetary disks around hd 163296 and doar 44. *The Astrophysical Journal*, 941(2): 172, 2022.

R. Li, Y.-X. Chen, and D. N. Lin. Dust accumulation near the magnetospheric truncation of protoplanetary discs around t tauri stars. *Monthly Notices of the Royal Astronomical Society*, 510(4):5246–5265, 2022.

J. E. Lindberg, S. B. Charnley, J. K. Jørgensen, M. A. Cordiner, and P. Bjerkeli. Externally heated protostellar cores in the ophiuchus star-forming region. *The Astrophysical Journal*, 835(1):3, 2017.

B. Lopez, S. Lagarde, R. Petrov, W. Jaffe, P. Antonelli, F. Allouche, P. Berio, A. Matter, A. Meilland, F. Millour, et al. Matisse, the vlti mid-infrared imaging spectro-interferometer. *Astronomy & Astrophysics*, 659:A192, 2022.

D. Lynden-Bell and J. E. Pringle. The evolution of viscous discs and the origin of the nebular variables. *MNRAS* , 168:603–637, Sept. 1974. doi: 10.1093/mnras/168.3.603.

D. Lynden-Bell and J. E. Pringle. The evolution of viscous discs and the origin of the nebular variables. *Monthly Notices of the Royal Astronomical Society*, 168(3):603–637, 1974.

M. K. McClure, E. Furlan, P. Manoj, K. L. Luhman, D. M. Watson, W. J. Forrest, C. Espaillat, N. Calvet, P. D'Alessio, B. Sargent, J. J. Tobin, and H.-F. Chiang. The Evolutionary State of the Pre-main Sequence Population in Ophiuchus: A Large Infrared Spectrograph Survey. *ApJS* , 188(1):75–122, May 2010. doi: 10.1088/0067-0049/188/1/75.

E. E. Mendoza. Infrared Photometry of T Tauri Stars and Related Objects. *ApJ* , 143:1010, Mar. 1966. doi: 10.1086/148584.

A. A. Michelson. I. on the application of interference methods to astronomical measurements. *The London, Edinburgh, and Dublin Philosophical Magazine and Journal of Science*, 30(182): 1–21, 1890.

A. A. Michelson and F. G. Pease. Measurement of the diameter of alpha-orionis by the interferometer. *Proceedings of the National Academy of Sciences*, 7(5):143–146, 1921.

N. Miret-Roig, P. A. B. Galli, J. Olivares, H. Bouy, J. Alves, and D. Barrado. The star formation history of Upper Scorpius and Ophiuchus. A 7D picture: positions, kinematics, and dynamical traceback ages. *A&A* , 667:A163, Nov. 2022. doi: 10.1051/0004-6361/202244709.

S. Mohanty, J. Greaves, D. Mortlock, I. Pascucci, A. Scholz, M. Thompson, D. Apai, G. Lodato, and D. Looper. Protoplanetary Disk Masses from Stars to Brown Dwarfs. *ApJ* , 773(2):168, Aug. 2013. doi: 10.1088/0004-637X/773/2/168.

T. Montmerle, L. Koch-Miramond, E. Falgarone, and J. E. Grindlay. Einstein observations of the rho ophiuchi dark cloud-an x-ray christmas tree. *Astrophysical Journal, Part 1 (ISSN 0004-637X), vol. 269, June 1, 1983, p. 182-201. Research supported by the Ministere des Relations Exterieures of France.*, 269:182–201, 1983.

D. Mourard, Brož, M., Nemravová, J. A., Harmanec, P., Budaj, J., Baron, F., Monnier, J. D., Schaefer, G. H., Schmitt, H., Tallon-Bosc, I., Armstrong, J. T., Baines, E. K., Bonneau, D., Bozi´c, H., Clausse, J. M., Farrington, C., Gies, D., Jurysek, J., Korcáková, D., McAlister, H., Meilland, A., Nardetto, N., Svoboda, P., Slechta, M., Wolf, M., and Zasche, P. Physical properties of ae a and its opaque accretion disk. *A&A*, 618:A112, 2018. doi: 10.1051/0004-6361/201832952. URL https://doi.org/10.1051/0004-6361/201832952.

N. Murray and J. Chiang. Disk winds and disk emission lines. *The Astrophysical Journal*, 474 (1):91, 1997.

J. Nemravová, P. Harmanec, M. Brož, D. Vokrouhlickỳ, D. Mourard, C. Hummel, C. Cameron, J. M. Matthews, C. Bolton, H. Božić, et al. ξtauri: a unique laboratory to study the dynamic interaction in a compact hierarchical quadruple system. *Astronomy & Astrophysics*, 594:A55, 2016.

G. Neugebauer, H. Habing, R. Van Duinen, H. Aumann, B. Baud, C. Beichman, D. Beintema, N. Boggess, P. Clegg, T. De Jong, et al. The infrared astronomical satellite (iras) mission. *Astrophysical Journal, Part 2-Letters to the Editor (ISSN 0004-637X), vol. 278, March 1, 1984, p. L1-L6. Research supported by the Science and Engineering Research Council and NASA.*, 278:L1–L6, 1984.

D. Nuernberger, W. Brandner, H. W. Yorke, and H. Zinnecker. Millimeter continuum observations of X-ray selected TTauri stars in Ophiuchus. *A&A* , 330:549–558, Feb. 1998.

F. Ochsenbein, P. Bauer, and J. Marcout. The vizier database of astronomical catalogues. *Astronomy and Astrophysics Supplement Series*, 143(1):23–32, 2000.

M. Page, C. Brindle, A. Talavera, M. Still, S. Rosen, V. Yershov, H. Ziaeepour, K. Mason, M. Cropper, A. Breeveld, et al. The xmm—newton serendipitous ultraviolet source survey catalogue. *Monthly Notices of the Royal Astronomical Society*, 426(2):903–926, 2012.

A. Palacios, M. Gebran, E. Josselin, F. Martins, B. Plez, M. Belmas, and A. Lebre. Pollux: a database of synthetic stellar spectra. *Astronomy & Astrophysics*, 516:A13, 2010.

Pinilla, Benisty, M., Birnstiel, T., Ricci, L., Isella, A., Natta, A., Dullemond, C. P., Quiroga-Nuñez, L. H., Henning, T., and Testi, L. Millimetre spectral indices of transition disks and their relation to the cavity radius. *A&A*, 564:A51, 2014. doi: 10.1051/0004-6361/201323322. URL https://doi.org/10.1051/0004-6361/201323322.

K. Pouilly, J. Bouvier, E. Alecian, S. H. P. Alencar, A.-M. Cody, J.-F. Donati, K. Grankin, G. A. Hussain, L. Rebull, and C. P. Folsom. Magnetospheric accretion in the intermediate-mass t tauri star hq tauri. *Astronomy & Astrophysics*, 642:A99, 2020.

J. E. Pringle. Accretion discs in astrophysics. *In: Annual review of astronomy and astrophysics. Volume 19.(A82-11551 02-90) Palo Alto, CA, Annual Reviews, Inc., 1981, p. 137-162.*, 19: 137–162, 1981.

A. Quirrenbach, D. Buscher, D. Mozurkewich, C. Hummel, and J. Armstrong. Maximum-entropy maps of the be shell star zeta tauri from optical long-baseline interferometry. *Astronomy and Astrophysics (ISSN 0004-6361), vol. 283, no. 2, p. L13-L16*, 283:L13–L16, 1994.

B. Reipurth, P. Hartigan, S. Heathcote, J. A. Morse, and J. Bally. Hubble Space Telescope Images of the HH 111 Jet. *AJ* , 114:757–780, Aug. 1997. doi: 10.1086/118509.

L. Ricci, L. Testi, A. Natta, and K. Brooks. Dust grain growth in ρ-ophiuchi protoplanetary disks. *Astronomy & Astrophysics*, 521:A66, 2010a.

L. Ricci, L. Testi, A. Natta, R. Neri, S. Cabrit, and G. J. Herczeg. Dust properties of protoplanetary disks in the taurus-auriga star forming region from millimeter wavelengths. *Astronomy & Astrophysics*, 512:A15, 2010b.

N. A. Ridge, J. D. Francesco, H. Kirk, D. Li, A. A. Goodman, J. F. Alves, H. G. Arce, M. A. Borkin, P. Caselli, J. B. Foster, M. H. Heyer, D. Johnstone, D. A. Kosslyn, M. Lombardi, J. E. Pineda, S. L. Schnee, and M. Tafalla. The complete survey of star-forming regions: Phase i data. *The Astronomical Journal*, 131(6):2921, jun 2006. doi: 10.1086/503704. URL https://dx.doi.org/10.1086/503704.

G. Rieke, E. Young, C. Engelbracht, D. Kelly, F. Low, E. Haller, J. Beeman, K. Gordon, J. Stansberry, K. Misselt, et al. The multiband imaging photometer for spitzer (mips). *The Astrophysical Journal Supplement Series*, 154(1):25, 2004.

M. Rubin, K. Altwegg, J.-J. Berthelier, M. R. Combi, J. De Keyser, S. A. Fuselier, T. I. Gombosi, M. S. Gudipati, N. Hänni, K. A. Kipfer, N. F. W. Ligterink, D. R. Müller, Y. Shou, and S. F. Wampfler. Volatiles in the H2O and CO2 ices of comet 67P/Churyumov–Gerasimenko. *Monthly Notices of the Royal Astronomical Society*, 526(3):4209–4233, 10 2023. ISSN 0035-8711. doi: 10.1093/mnras/stad3005. URL https://doi.org/10.1093/mnras/stad3005.

C. Salyk, J. H. Lacy, M. J. Richter, K. Zhang, G. A. Blake, and K. M. Pontoppidan. Detection of water vapor in the terrestrial planet forming region of a transition disk. *The Astrophysical Journal Letters*, 810(2):L24, 2015.

E. F. Schlafly and D. P. Finkbeiner. Measuring reddening with sloan digital sky survey stellar spectra and recalibrating sfd. *The Astrophysical Journal*, 737(2):103, 2011.

T. Schmidt-Kaler. Automated spectral classification. A survey. *Bulletin d'Information du Centre de Donnees Stellaires*, 23:2, Oct. 1982.

F. Schwab. Relaxing the isoplanatism assumption in self-calibration; applications to low-frequency radio interferometry. *Astronomical Journal (ISSN 0004-6256), vol. 89, July 1984, p. 1076-1081.*, 89:1076–1081, 1984.

J. Serna, J. Hernandez, M. Kounkel, E. Manzo-Martínez, A. Roman-Lopes, C. G. Román-Zúñiga, M. G. Batista, G. Pinzón, N. Calvet, C. Briceño, et al. Stellar rotation of t tauri stars in the orion star-forming complex. *The Astrophysical Journal*, 923(2):177, 2021.

W. Shillue, W. Grammer, C. Jacques, R. Brito, J. Meadows, J. Castro, J. Banda, and Y. Masui. The alma photonic local oscillator system. In *2011 XXXth URSI General Assembly and Scientific Symposium*, pages 1–4. IEEE, 2011.

M. Skrutskie, R. Cutri, R. Stiening, M. Weinberg, S. Schneider, J. Carpenter, C. Beichman, R. Capps, T. Chester, J. Elias, et al. The two micron all sky survey (2mass). *The Astronomical Journal*, 131(2):1163, 2006.

M. Souza de Joode. Modeling of a protoplanetary disk based on alma observations. Technical report, Faculty of Mathematics and Physics, Charles University, 2022. URL https://www.marco-souza-de-joode.cz/undergraduate-projects/radioastronomy-alma.

K. R. Stapelfeldt, A. M. Watson, J. E. Krist, C. J. Burrows, D. Crisp, G. E. Ballester, J. T. Clarke, R. W. Evans, J. S. Gallagher III, R. E. Griffiths, et al. A variable asymmetry in the circumstellar disk of hh 30. *The Astrophysical Journal*, 516(2):L95, 1999.

S. E. Strom, S. Edwards, and M. F. Skrutskie. Evolutionary timescales for circumstellar disks associated with solar-type pre-main sequence stars. In *AIP Conference Proceedings*, volume 207, pages 71–86. American Institute of Physics, 1990.

O. Struve and M. Rudkjøbing. Stellar Spectra with Emission Lines in the Obscuring Clouds of Ophiuchus and Scorpius. *ApJ* , 109:92, Jan. 1949. doi: 10.1086/145107.

S. Takasao, K. Tomida, K. Iwasaki, and T. K. Suzuki. A three-dimensional simulation of a magnetized accretion disk: fast funnel accretion onto a weakly magnetized star. *The Astrophysical Journal*, 857(1):4, 2018.

S. Takita, H. Kataza, Y. Kitamura, D. Ishihara, Y. Ita, S. Oyabu, and M. Ueno. A survey of T Tauri stars with AKARI towards the Taurus-Auriga region. *A&A* , 519:A83, Sept. 2010. doi: 10.1051/0004-6361/200913475.

P. H. van Cittert. Die Wahrscheinliche Schwingungsverteilung in Einer von Einer Lichtquelle Direkt Oder Mittels Einer Linse Beleuchteten Ebene. *Physica*, 1(1):201–210, Jan. 1934. doi: 10.1016/S0031-8914(34)90026-4.

B. Wilking, M. Gagné, and L. Allen. Star formation in the rho ophiuchi molecular cloud. *arXiv preprint arXiv:0811.0005*, 2008.

B. A. Wilking and C. J. Lada. The discovery of new embedded sources in the centrally condensed coreof the rho Ophiuchi dark cloud : the formation of a bound cluster ? *ApJ* , 274:698–716, Nov. 1983. doi: 10.1086/161482.

J. P. Williams and C. McPartland. Measuring protoplanetary disk gas surface density profiles with alma. *The Astrophysical Journal*, 830(1):32, oct 2016. doi: 10.3847/0004-637X/830/1/32. URL https://dx.doi.org/10.3847/0004-637X/830/1/32.

E. L. Wright, P. R. Eisenhardt, A. K. Mainzer, M. E. Ressler, R. M. Cutri, T. Jarrett, J. D. Kirkpatrick, D. Padgett, R. S. McMillan, M. Skrutskie, et al. The wide-field infrared survey explorer (wise): mission description and initial on-orbit performance. *The Astronomical Journal*, 140(6):1868, 2010.

D. G. York, J. Adelman, J. E. Anderson Jr, S. F. Anderson, J. Annis, N. A. Bahcall, J. Bakken, R. Barkhouser, S. Bastian, E. Berman, et al. The sloan digital sky survey: Technical summary. *The Astronomical Journal*, 120(3):1579, 2000.

F. Zernike. The concept of degree of coherence and its application to optical problems. *Physica*, 5(8):785–795, 1938. ISSN 0031-8914. doi: https://doi.org/10.1016/S0031-8914(38)80203-2. URL https://www.sciencedirect.com/science/article/pii/S0031891438802032.

K. Zhang, G. A. Blake, and E. A. Bergin. Evidence of fast pebble growth near condensation fronts in the hl tau protoplanetary disk. *The Astrophysical Journal Letters*, 806(1):L7, 2015.

K. Zhang, E. A. Bergin, G. A. Blake, L. I. Cleeves, and K. R. Schwarz. Mass inventory of the giant-planet formation zone in a solar nebula analogue. *Nature Astronomy*, 1(6):0130, 2017.

A. Zurlo, L. A. Cieza, S. Pérez, V. Christiaens, J. P. Williams, G. Guidi, H. Cánovas, S. Casassus, A. Hales, D. A. Principe, et al. The ophiuchus disc survey employing alma (odisea)–ii. the effect of stellar multiplicity on disc properties. *Monthly Notices of the Royal Astronomical Society*, 496(4):5089–5100, 2020.

List of Figures

List of Tables

List of Acronyms